A NUMERICAL INVESTIGATION OF TRACK-BRIDGE INTERACTION IN RAILWAY BRIDGES

A THESIS SUBMITTED TO
THE GRADUATE SCHOOL OF NATURAL AND APPLIED SCIENCES
OF
MIDDLE EAST TECHNICAL UNIVERSITY

BY

ALPER ÖZTÜRK

IN PARTIAL FULFILLMENT OF THE REQUIREMENTS
FOR
THE DEGREE OF DOCTOR OF PHILOSOPHY
IN
CIVIL ENGINEERING

JANUARY 2024

Approval of the thesis:

A NUMERICAL INVESTIGATION OF TRACK-BRIDGE INTERACTION IN RAILWAY BRIDGES

submitted by **ALPER ÖZTÜRK** in partial fulfillment of the requirements for the degree of **Doctor of Philosophy** i**n Civil Engineering, Middle East Technical University** by,

Prof. Dr. Halil Kalıpçılar
Dean, **Graduate School of Natural and Applied Sciences**

Prof. Dr. Erdem Canbay
Head of the Department, **Civil Engineering**

Prof. Dr. Eray Baran
Supervisor, **Civil Engineering, METU**

Examining Committee Members:

Prof. Dr. Murat Dicleli
Engineering Sciences, METU

Prof. Dr. Eray Baran
Civil Engineering, METU

Prof. Dr. Ayşegül Askan Gündoğan
Civil Engineering, METU

Prof. Dr. Kurtuluş Soyluk
Civil Engineering, Gazi University

Asst. Prof. Dr. Halit Cenan Mertol
Civil Engineering, Atılım University

Date: 16.01.2024

I hereby declare that all information in this document has been obtained and presented in accordance with academic rules and ethical conduct. I also declare that, as required by these rules and conduct, I have fully cited and referenced all material and results that are not original to this work.

Name Last name : Alper Öztürk

Signature :

ABSTRACT

A NUMERICAL INVESTIGATION OF TRACK-BRIDGE INTERACTION IN RAILWAY BRIDGES

Öztürk, Alper
Doctor of Philosophy, Civil Engineering
Supervisor : Prof. Dr. Eray Baran

January 2024, 171 pages

In railway tracks, additional stresses occur in rails due to interaction between the rail and the bridge superstructure, which is a phenomenon known as track-bridge interaction (TBI). The additional rail stresses (ARSs) develop mainly as a result of temperature effect, vertical bending of bridge superstructure, braking/acceleration of trains traveling over the bridge. One of the major parameters affecting the TBI response is the behavior of interface elements simulating the coupling between the bridge superstructure and the rail. In TBI analysis this coupling is defined by the so-called longitudinal resistance-displacement curves (RDCs).

The first part of the study focuses on the longitudinal aspect of TBI through numerical investigation. The numerical modeling approach was verified with available analytical solutions and data obtained from bridge monitoring. The primary interest was to illustrate how sensitive the TBI response is to changes in RDCs. The parametric study was extended to investigate the effect of expansion length and substructure stiffness. Analysis results reveal that for simply supported precast concrete girder bridges, using RDCs developed from ballastless railway track measurements can be an economical alternative to specified provisions. Substructure stiffness was determined to have a crucial effect on the ARSs especially under acceleration/braking loads.

The second part of the study comprehensively investigates longitudinal TBI in railway bridges under seismic ground motion. The investigation focused on two prestressed concrete girder bridges located in a seismically active area of Türkiye. The study focused on the influence of various parameters on TBI, including service earthquake intensity measure, soil property, distance to fault, and deck expansion joint locations. A detailed numerical modeling approach utilized Nonlinear Time History Analysis (NTHA) to capture dynamic responses under recorded seismic ground motions. Results reveal that earthquake magnitude and distance to fault significantly affect ARSs. Expansion joints at pier locations impacted rail stress distribution, reducing maximum tensile stresses and increasing compressive stresses. Furthermore, using fixed boundary conditions at pier bases provides comparable results to soil spring modeling for the investigated bridges. Comparison of analysis results for utilization of unloaded and loaded RDCs highlights the importance of considering train-induced loads in seismic assessments.

Finally, the same numerical approach was further utilized to explore the effect of scaling of the ground motion, distances to epicenter and rupture on TBI response, based on recent earthquakes happened in Kahramanmaraş, Türkiye. Five different ground motion sets were selected based on their intensity including Pazarcık (Mw=7.7) and Elbistan (Mw=7.6) earthquakes. Five stations were utilized for each event to assess how earthquake intensity measures can reveal limitations in TBI response in design. As seismic intensity increases, the analysis highlights the importance of displacements over ARSs in design limitations. Design recommendations were developed based on evaluation of this study.

Keywords: Track-Bridge Interaction, Additional Rail Stress, High-Speed Railway, Continuously Welded Rail, Time-History Analysis

ÖZ

DEMİRYOLU KÖPRÜLERİNDE RAY-KÖPRÜ ETKİLEŞİMİNİN SAYISAL OLARAK İNCELENMESİ

Öztürk, Alper
Doktora, İnşaat Mühendisliği
Tez Yöneticisi: Prof. Dr. Eray Baran

Ocak 2024, 171 sayfa

Demiryolu raylarında, ray ve köprü üst yapısı arasındaki etkileşimden dolayı raylarda ek gerilmeler oluşur. Bu fenomene ray-köprü etkileşimi (RKE) denir. Ek ray gerilmeleri (ERG'ler) esas olarak sıcaklık etkisinden, köprü üst yapısının düşey yönde eğilmesinden, köprü üzerinde hareket eden trenlerin frenlemesinden/ivmelenmesinden kaynaklanmaktadır. RKE tepkisini etkileyen önemli parametrelerden biri, köprü üst yapısı ile ray arasındaki bağlantıyı simüle eden arayüz elemanlarının davranışıdır. RKE analizinde bu bağlantı, uzunlamasına direnç-yer değiştirme eğrileri (DYE'ler) olarak adlandırılan eğrilerle tanımlanır.

Birinci kısım, RKE'nin uzunlamasına yönüne sayısal araştırmalar aracılığı ile odaklanmıştır. Sayısal modelleme yaklaşımı, mevcut analitik çözümler ve köprü izleme verileri ile doğrulanmıştır. Buradaki öncelikli amaç, DYE'lerdeki değişikliklerin RKE'ye ne kadar etkisi olduğunun gösterilmesi olmuştur. Parametrik çalışma, genleşme uzunluğu ve alt yapı rijitliği etkilerini incelemek üzere genişletilmiştir. Analiz sonuçları basit mesnetli prekast kiriş köprüler için, balastsız demiryolu köprülerine özgü olduğu kanıtlanmış DYE'lerin, şartnameler tarafından belirtilen eğrilere ekonomik bir alternatif olabileceğini, ortaya çıkarmıştır. Altyapı rijitliğinin özellikle ivmelenme/frenleme yükleri altında ERG'ler üzerinde kritik bir etkisi olduğu belirlenmiştir.

Çalışmanın ikinci bölümü, Türkiye'nin sismik olarak aktif bir bölgesinde bulunan iki öngerilmeli prekast beton kirişli demiryolu köprüsündeki uzunlamasına RKE detaylı bir şekilde ele almaktadır. Zemin özellikleri, fay kırılma mesafesi, köprü genleşme derzi gibi çeşitli parametrelerin RKE üzerindeki etkisini inceleyen araştırma, Zaman Tanım Alanında Analiz (ZTAA) metodu kullanarak kaydedilen sismik zemin hareketleri altındaki dinamik tepkiyi yakalamak için ayrıntılı bir sayısal modelleme yaklaşımını benimsemiştir. Sonuçlar, deprem büyüklüğü ve fay hattına uzaklığın ERG'leri önemli ölçüde etkilediğini göstermektedir. Köprü genleşme derzlerinin orta ayak konumlarında, ray gerilme dağılımını etkileyerek maksimum çekme gerilmelerini azalttığı ve basınç gerilmelerini artırdığı belirlenmiştir. Ayrıca, taban düğüm noktalarında ankastre sınır koşulları kullanmanın, zemin-yay modellemesine benzer sonuçlar verdiği görülmüştür. Tren yüklü ve yüksüz durumlar için yapılan analizlerin karşılaştırılması, tren kaynaklı yüklerin dikkate alınmasının önemini vurgulamaktadır.

Son olarak, Kahramanmaraş'ta meydana gelen son depremler temelinde deprem büyüklüğünün, fay hattı ve fay kırılma mesafelerinin RKE’ye olan etkisini incelemek için aynı sayısal yaklaşım kullanılmıştır. Pazarcık (Mw=7.7) ve Elbistan (Mw=7.6) depremleri de dahil olmak üzere büyüklüklerine göre beş farklı zemin hareketi seti seçilmiştir. Her deprem için beş istasyon kullanılmış, böylece deprem büyüklük parametrelerinin, RKE tasarımına hangi sınırlamalara dikkat edilmesi gerektiği anlaşılmıştır. Analiz sonuçları, sismik etkilerin artmasıyla, deplasmanların ERG'lere kıyasla daha önemli hale geldiğini ortaya çıkarmıştır. Bu çalışmanın değerlendirmesine dayanarak tasarım önerileri geliştirilmiştir.

Anahtar Kelimeler: Ray-Köprü Etkileşimi, Ray Gerilmesi, Yüksek Hızlı Demiryolu, Sürekli Kaynaklı Ray, Zaman Tanım Alanında Analiz

For Pırıl

ACKNOWLEDGMENTS

I would like to express my deepest gratitude to my supervisor Prof. Dr. Eray Baran for the continuous guidance and constructive criticism he has provided throughout the preparation of the thesis. Without his patience and encouragement, this thesis would not have been completed.

I would also like to thank my thesis monitoring committee members, and the examining committee members one by one for their precious time and comments.

I extend my heartfelt gratitude to Aydan, my mother, Tezcan, my father, and Andaç, my brother, for consistently standing by me and offering unwavering support through every situation.

I am incredibly thankful for my friend Tolga Cantürk. He is always there for me during tough times, cheering me on, and providing the motivation to keep going.

I would like to give special thanks to my wife İpek Çakaloz Öztürk for her endless love, encouragement, and support regardless of the time I stole from her.

Finally, I dedicate this thesis to my beloved daughter, Pırıl, my pineapple and my crabby crab.

TABLE OF CONTENTS

CHAPTERS

APPENDICES

LIST OF TABLES

TABLES

LIST OF FIGURES

FIGURES

CHAPTER 1

INTRODUCTION

1.1 General

High-speed rail (HSR) holds a vital role in a nation's daily activities, impacting the lives of its people, economy, and public transportation infrastructure significantly. According to Union of Railways (UIC), a HSR is defined as a railway system with an operating speed of more than 200 km/h. The first segment of the Shinkansen Train line, named as Japanese Bullet serving between Tokyo and Osaka was completed in 1964 and this is considered as the first HSR with 210 km/h maximum speed (Dai et al. (2016)). In 1981, French Railway Company (SCNF) started operating HSR line between Paris and Lyon with a maximum 260 km/h train speed. HSR lines spread through France, Italy, Germany, Spain and Belgium from 1981 to 1997. As of today, HSR lines are operational in over 21 countries. Remarkably, the global HSR network expanded by more than a third from approximately 44,000 to around 59,000 kilometers between 2017 and 2022, as reported by the UIC (2023).

To meet the growing demand for HSR networks, there has been a significant adoption of continuously welded rails (CWRs) in HSR lines. CWR refers to a type of railway track where long stretches of rail are welded together to form a continuous line, as opposed to the traditional method of connecting shorter (20-25 meters long) sections of rail using fish plate joints. In CWR, the rails are welded end-to-end, creating a continuous and seamless track without the gaps found in jointed rails. Example photos for type of railway tracks are given in Figure 1.1.

CWR offers several advantages over jointed rails, including smoother rides for trains, reduced maintenance needs, reduced risk of track buckling, and improved durability. The absence of joints eliminates the noise as trains pass over them, contributing to a quieter and more comfortable travel experience. Additionally, CWR tends to require less frequent maintenance and inspections compared to jointed tracks, enhancing overall operational efficiency for railways.

CWRs present a challenge as they lack the flexibility to expand or contract under varying thermal and mechanical loads due to their uninterrupted structure. In contrast, structures like bridges along the railway line undergo expansion or contraction during their service life, leading to potential regions of disruption on the railway track. This disparity in expansion and contraction between the track and the bridge creates a coupling mechanism that introduces additional rail stresses (ARSs) and displacements, impacting both the track and the bridge strucure. The thermal gradient between the deck and rail, as well as the vertical and acceleration/braking loads due to passing trains were the main effects causing this mechanism. Factors, such as creep, shrinkage, and seismic actions may also cause TBI in railway lines. Figure 1.2 illustrates the mechanism of force transfer between the track and the bridge caused by thermal effects when the bridge expands due to an increase in temperature and vertical traffic loading. As depicted in the figure, the difference in the temperature creates compressive stresses in the rails. On the other hand, the state of stress in raill due to vertical load traffic loading might be different. In terms of vertical train loading, the location of train has also crucial impact on the resulting ARSs and the most critical location should be considered at design stage. These combined stresses according to the most critical state are superimposed with existing ones on the rail. The existing stresses are mainly due to the temperature fluctuations in rails, residual stresses, and stresses induced by bending from wheel loads. In the long run, uncontrolled stresses resulting from TBI, alongside the already existing effects, can potentially lead to rail buckling when rails are under compression or rail fracture due to tension.

To ensure safety of railway with presence of ARSs across various track types, and displacements especially in ballasted tracks (to ensure ballast stability), international and national codes have regulated the determination of structural parameters and associated actions to be used in TBI. The codes also provide methodologies for modeling TBI, based on the comprehensive experimental and numerical studies conducted between the 1970s to the 1990s.

Recently, an attempt has been made by different researches (Kang et al. (2021), Su et al. (2018)) to update the international regulations for accurate consideration of TBI based on the recent developments. Nevertheless, little emphasis was placed on exploring the utilization of diverse longitudinal resistance displacement curves (RDCs), and investigating the impact of seismic actions on TBI. This thesis involves three distinct primary sections, each dedicated to numerical studies aimed at addressing the existing research gaps within the field. The first part is a numerical investigation of simply supported precast concrete girder railway bridges, where the sensitiviy of RDCs were primarily aimed. The second part investigates TBI response under seismic ground motion centered around two designed prestressed concrete girder bridges in Türkiye based on service-level earthquakes. Finally, the third part provides an insight into how unscaled ground motion characteristics affect TBI, based on recent Pazarcık (Mw=7.7) and Elbistan (Mw=7.6) earthquakes and following aftershocks and its relation with the intensity measures.

1.2 Objectives and Scope

The primary interest of the first part of the study is to illustrate how sensitive the TBI response is to changes in RDCs with respect to separate and sequential analysis approaches given in the international design codes. The motivation behind the study is the insufficient prior exploration and comprehensive investigation into the impact and implications of RDCs. Following the validation of the modeling approach against available analytical solutions and data obtained from bridge monitoring, a parametric study was conducted to fulfill this objective. Subsequently, this study was expanded to explore the impacts of expansion length and substructure stiffness, alongside the type of RDCs.

The considerations governing loadings in TBI analysis, along with associated permissible stresses and displacements, originate from an ERRI (1997) project titled “Improved Knowledge of Forces in CWR Track.” The relevant studies were primarily conducted in Western Europe, particularly centralized in Germany, leading to seismic actions not being factored in as a parameter in TBI analysis. Consequently, the outcomes are mostly valid to railway systems located in regions characterized by lower seismic activity. In order to address the gap in the literature on TBI analysis with the presence of seismic effect, an investigation was conducted as the second part of the study. This exploration was based on two designed precast girder bridges located in a seismically active area. A detailed numerical modeling approach was employed, utilizing Nonlinear Time History Analysis (NTHA) to capture the dynamic response under recorded seismic ground motions. The parameters investigated within this context include earthquake magnitude and distance, the presence of expansion joints at pier locations, and train-induced loads.

The third part of the study is motivated by a desire to gain deeper insights into the specific impact of actual earthquake ground motions on TBI by using one of the previously investigated designed bridges. To achieve this, ground motion records from recent earthquakes in the Kahramanmaraş Region were utilized. This investigation holds a crucial significance as the analyses were conducted without any scaling of the recorded ground motions, aiming to demonstrate the TBI response that would be expected in the case of ground motions with varying intensities produced by the same seismic activity. The outcomes of this investigation led to design recommendations intended for use by bridge designers.

1.3 Thesis Organization

The thesis comprises five chapters. The initial chapter is an Introduction. Chapter 2 addresses TBI response based on thermal loads and the train loading, while Chapters 3 and 4 specifically discuss seismic loads.

In Chapter 2, the numerical analysis is first verified with avaliable analytical solutions and data obtained from bridge monitoring. Using this verified model parametric results are represented by different RDC types, substructure stiffness levels and expansion lengths, as well as seperate and sequential analysis approaches.

Chapter 3 presents the results of NTHA based on 15 sets of ground motion data. A comprehensive examination of TBI behavior under various ground motion parameters, such as service earthquake intensity measures, soil properties, and distance to fault is provided. Additionally, the influence of two distinct methods for pier support modeling (i.e., utilizing fixed boundary conditions at pier bases versus employing soil spring modeling based on recommended values for spread footing) on TBI response is discussed.

In Chapter 4, results from additonal analyses under the ground motion records from the Kahramanmaraş-Elbistan Earthquakes are presented. Examining ARSs and displacement thresholds, this section offers design recommendations for TBI railway bridges located within earthquake-prone regions. Moreover, the variation of the bridge ARSs and displacements with the peak ground velocity (PGV) and, peak ground acceleration (PGA) of the records is also presented.

The findings from the aforementioned studies are consolidated and presented as concluding remarks in Chapter 5.

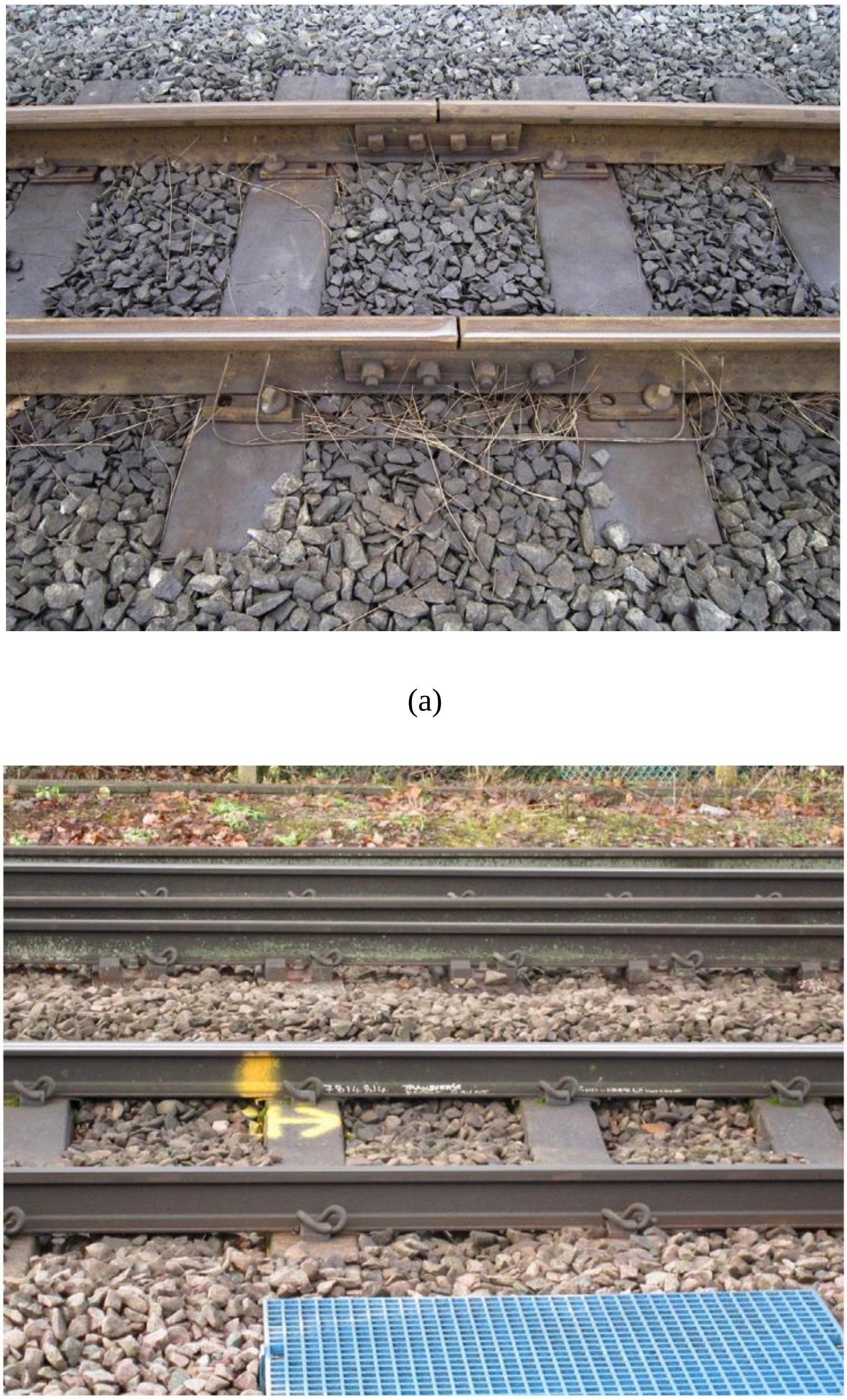

(a)

(b)

Figure 1.1. An example of (a) jointed (b) continuously welded rail

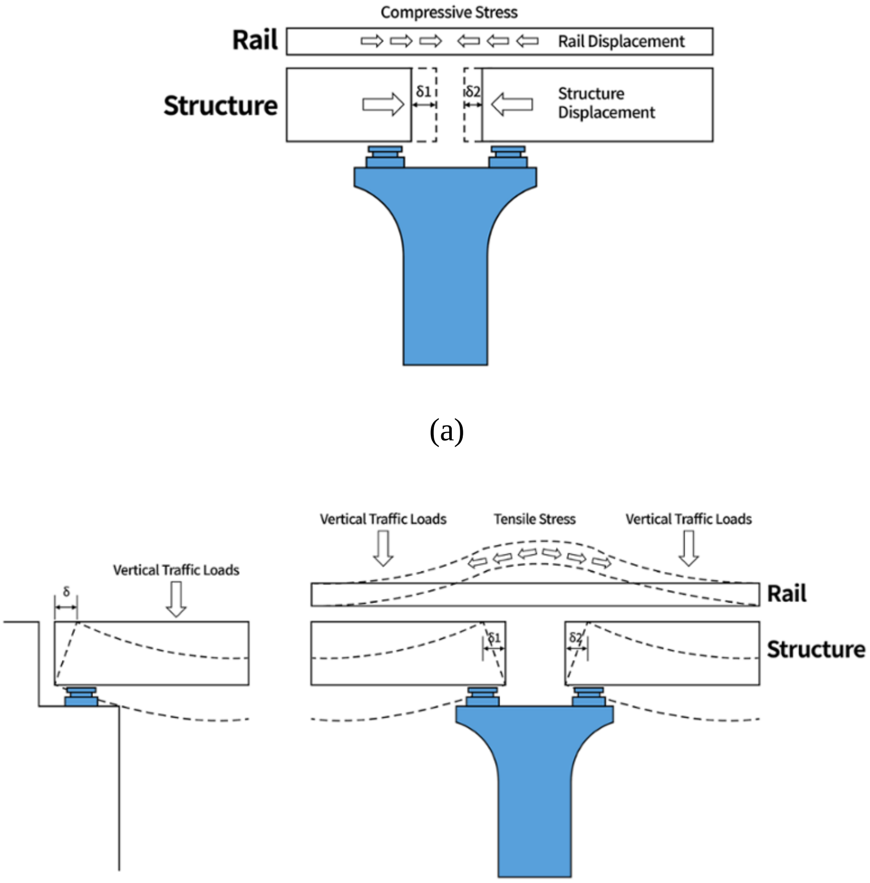

(a)

(b)

Figure 1.2. Illustration of transfer mechanism between track and bridge under (a) thermal and (b) vertical train loads (https://resource.midasuser.com/en/solution/rail-structure-interaction, 2023)

CHAPTER 2

LONGITUDINAL TRACK BRIDGE INTERACTION IN SIMPLY SUPPORTED PRECAST CONCRETE GIRDER RAILWAY BRIDGES

2.1 Introduction

Advancements in welding technology have led to replacement of jointed high speed rail tracks with continuous welded rails (CWRs) in an attempt to have a safer track under high-speeds, reduced maintenance costs, increased service life properties, increased passenger comfort, and reduced noise emission (Tzepushelov and Troyitzky 1974). Although CWRs have several advantages (Enshaeian and Rizo 2021) when compared with conventional jointed tracks, continuous nature of these tracks prevents free expansion/contraction under thermal and mechanical loading. Such a restraint results in additional compressive and tensile stresses in the rails, which must be taken into consideration during track design. International railway design codes usually provide limits for additional rail stresses (ARSs) and displacements for bridge superstructure under thermal and train loads (UIC 774-3R (2001), (EN 1991-2 (2003), DIN Fb 101 (2003), KR C-08080(2014)). ARSs represent the longitudinal stresses developing in the rail due to interaction between the rail and the superstructure, which is a phenomenon known as track-bridge interaction (TBI) or rail-structure interaction (RSI). The sources that lead to ARSs are temperature difference between the rail and bridge deck as well as the vertical and braking/accelerating forces of the train passing over the bridge. In order to provide the required safety margin, design codes provide maximum tensile and compressive stress limits for rails (Mirković et al. 2018). These limits, however, usually do not include the rail stresses due to temperature changes in the rail.

In numerical modeling of railway bridges, the interaction between the bridge superstructure and the rails is simulated with interface elements and the behavior of these elements is defined by the so-called longitudinal resistance-displacement curves (RDCs). Depending on the presence or absence of a vertical train loading, the RDC is termed as either loaded or unloaded. As the RDCs represent the degree of interaction between the bridge deck and the railway track, they have a significant effect on the TBI response of the bridge system.

Two aspects of TBI need special consideration in the design of high-speed railway bridges. Vertical aspect of the problem has previously been investigated in detail (Kim et al. 2010, Chellini et al. 2011, Rocha et al. 2012, Kwark et al. 2004, Liu et al. 2008, Song et al. 2003, Galvin et al. 2018, Karoumi et al. 2005, Cheng et al. 2001, Guo et al. 2012, Sung and Chang 2019, Alijani et al. 2022). This aspect mainly focuses on vibration analysis of the system and utilizes dynamic properties of the bridge, track, and train. The second aspect, which has not been investigated as thoroughly as the first one in the literature, is the longitudinal response of the track-bridge system. The longitudinal response of TBI is commonly studied by considering temperature and moving loads according to several international standards (EN 1991-2 (2003), DIN Fachbericht 101 (2003), TB10015 (2012), KR C-08080 (2014), UIC 774-3R (2001)). In this case, the adopted approach generally involves treating the problem statically by ignoring the dynamic effects.

Discussions on the phenomena of TBI date back to the effort driven by Stokes (1867) in order to solve differential equations related with the braking of trains over railway bridges. Frýba (1996) solved the problem analytically based on the linear elastic relation between rail and bridge deck under thermal loads. For the longitudinal aspect of TBI, some of the recent studies focus on the difference between the so called “separate” and “sequential” analysis approaches. The separate (i.e., simplified) analysis approach, as described in design codes, assumes superposition of forces resulting from the individual effects of thermal, bending, and braking/accelerating. The rationale behind this assumption is that linear superposition of the ARSs should always result in higher stresses. Such a linear superposition of various effects may produce inaccurate forces when any of the components in the system exhibits a nonlinear behavior. In this case, the procedure specified in design codes may overpredict the actual ARSs and underpredict the relative displacements. In the case of sequential (i.e., complete) analysis approach, a separate load effect is considered at each analysis step with the final condition in the previous load step taken as the initial condition for the next step. The separate analysis approach is more practical and common than sequential analysis among bridge designers in the light of international provisions, since it requires less effort and can be completed by many of the available FE software without a need to implement the loaded/unloaded states to the same model. However, there might be cases where a separate analysis indicates a safe design while a sequential analysis indicates otherwise depending on the level of loading, geometric properties of the bridge system, and the properties of the rail interface elements used to model TBI.

Sanguino and Requejo (2009) showed the effect of numerical analysis method (i.e., separate versus sequential) on the results of test cases given in the Appendix of UIC 774-3R (2001). Ruge and Birk (2007) were one of the pioneers who investigated arbitrary sequence of loads using coupling interface based on the implementation of an exact formulation. Widarda (2009) studied the track-bridge interaction problem through dynamic analyses by utilizing appropriate dynamic properties of trains. Zhang et al. (2015) conducted experiments on several types of fasteners used in urban rail transit and obtained RDCs in order to improve the accuracy of numerical TBI analyses. Huang et al. (2021) studied the effect of the mechanical behavior of the fasteners to seismic performance of urban rail viaduct. Yan et al. (2012) analyzed a railway bridge consisting of both simply supported and continuous spans and concluded that the effect of the longitudinal stiffness of piers on TBI analysis results are different for the simply supported and continuous spans. Yang and Jang (2016) proposed a practical solution using interface elements that are adaptive to various loading cases based on their experimental findings. Yun et al. (2019) monitored the last span of a 38-span simply supported prestressed concrete (PSC) girder railway bridge with ballasted track in order to collect the temperature values at different locations along the span, as well as to extract the unloaded RDCs. Furthermore, numerical analysis of the bridge system was conducted for unloaded condition and the numerical results agreed with the measured response. Dai et al. (2020) provided an analytical algorithm for calculating longitudinal TBI forces especially for long span bridges with rail expansion devices. Mirza et al. (2016) conducted an FE numerical investigation on the behavior of rails under thermal action after replacement of timber transoms with fiber reinforced urethane cross beams in an existing railway. Kašpárek et al. (2020) monitored a highly skewed arch bridge equipped with a special steering bar system in order to measure the resistance displacement behavior at track-bridge interface. Ryjáček and Vokáč (2014) conducted a long-term monitoring on a four-span simply supported steel truss bridge utilizing both ballasted and ballastless tracks. A parametric study was conducted by Ramos et al. (2019) to determine a limiting bridge length by adjusting rail and deck expansion joints on PSC girder bridges. Chen et al. (2013) developed a numerical analysis tool using an existing material library to establish a common computer model for TBI on arch bridges with CWRs. Recently, Kang et al. (2021) indicated that TBI rail stress limits specified in design codes were developed based on theoretical models and track systems that are outdated nowadays due to the rapid advancement in the field of high-speed rail transportation. They provided recommendations to increase the current stress limits in order to allow for longer railway bridges. In addition, ARSs also develop as a result of earthquakes or other disasters. Recently, ARSs due to earthquake loads on the tracks for high-speed railway bridges also studied by several authors (Hu et al. (2022a), Hu et al. (2022b)).

Zhang et al. (2020) proposed an equivalent modeling approach for analysis of multi-span simply supported railway bridges under seismic excitations. The proposed model was reported to reduce the overall complexity of the model and hence improve the computational efficiency. Wang et al. (2022) investigated the seismic response of a specific type of simply supported railway bridge system under near-fault ground motions with changing fault distance, spatial location characteristics and ground acceleration. It was concluded that the regional ground motion analysis approach adopted in their study can be employed for selection of high-speed railway routes to improve line safety. Analyses on railway bridges considering the interaction between train and bridge have recently been conducted by several researchers (Peixer et al. (2021), Kohl et al. (2023), Jin et al. (2022), Eroglu et al. (2023)). Peixer et al. (2021) investigated the effect of track irregularities on railway line safety by considering a continuous nine-span steel-concrete composite bridge. Jin et al. (2022) studied the probability of train derailment under the combined effect of seismic events and track irregularities by utilizing a multispan simply supported bridge model. Eroglu et al. (2023) conducted dynamic analysis of a train-track-bridge system to investigate the effects of various parameters, such as train speed, bridge span length and track stiffness. Kohl et al. (2023) considered many different vehicle models to study the accuracy of the simplified approach (i.e., additional damping approach) for vehicle-bridge interaction. Kang et al. (2018) provided a review of structural systems employed in high-speed railway bridges in Germany and indicated that simply supported box girder bridges are the most commonly used bridge type. The reported span lengths for this type of bridges are 25 m for small overpasses, while longer spans of 44 m and 58 m are typically used for valley crossings and large viaducts.

Although RDCs are the essential variable that determines TBI in terms of separate and sequential analysis results, this aspect has not been studied in detail in the literature. Therefore, the primary interest in the current study is to determine how sensitive the TBI response is to changes in RDCs with both separate and sequential analysis approaches. The effort was focused on the combined effects of RDC type, expansion length, and substructure stiffness on the TBI response. Apart from expansion length, substructure stiffness and RDCs, parameters related with geometrical and material properties of the bridge were also investigated both in terms of ARSs and longitudinal displacements. Separate and sequential numerical TBI analyses on several railway bridges were conducted using a commercial FE software MIDAS Civil (2012). Analytical verification was performed by considering linear elastic RDCs for thermal loads driven by Frýba (1996). Results from previous research by Yun et al. (2019) were used for verification of the FE modeling approach.

Following the verification of the FE model a parametric study was conducted. A flowchart of the analysis steps followed in the current study is given in Figure 2.1.

2.1.1 Motivation for Present Study and Discussion of Methodology

The present chapter addresses the need for a detailed investigation of the sensitivity of the TBI response to changes in RDCs with both separate and sequential analysis approaches. Although RDCs are the essential variable that determines TBI in terms of separate and sequential analysis results, this aspect has not been studied in detail in the literature. Moreover, there is a need for a thorough investigation of the ability of the RDCs specified in design codes to represent the actual TBI response. The initial stiffness and resistance capacity of the track-bridge interface elements depend on many factors, such as the presence and type of ballast, type of fastening system, type of sleepers, as well as the friction between these components. With these multiple factors affecting the behavior of the track-bridge interface, there is a growing necessity for a comprehensive investigation. Therefore, the primary interest in the current study is to fill these gaps in the literature.

The methodology adopted in this study involves a numerical investigation in an attempt to provide a better understanding of TBI for bridges incorporating CWRs. TBI analyses on several railway bridges were conducted using a commercial FE software MIDAS Civil (2012). Analytical verification of the numerical results was performed by considering linear elastic RDCs for thermal loads driven by Frýba (1996). Empirical data reported in previous research by Yun et al. (2019) was used for further verification of the FE modeling approach. Following the verification of the FE model against analytical benchmark and real-world data, the model was utilized to conduct a parametric study. The effort was focused on the combined effects of RDC type, expansion length, and substructure stiffness on the TBI response. Apart from expansion length, substructure stiffness and RDCs, parameters related with geometrical and material properties of the bridge were also investigated both in terms of ARSs and longitudinal displacements. A flowchart of the analysis steps followed in the study is given in Figure 2.1.

2.2 TBI Modeling

2.2.1 Two Dimensional Modeling Approach

TBI modeling details adopted in the current study are illustrated in Figure 2.2(a) and Figure 2.2(b), respectively for the cases of a single-span single-track bridge and multi-span double-track bridge. It should be noted that these figures are presented for the illustration of the general modeling details, and the number of spans utilized in analyses varied, as mentioned in the subsequent sections. Deck and rails were modeled using 2D beam elements considering both axial and flexural properties. Elements simulating the bridge deck and girders were located at the centroid of the composite section. These elements were connected to the nodes located at the top surface of the deck and to the nodes located at girder supports with rigid beam elements. Flexibility provided in the longitudinal direction due to girder support assembly and bridge pier was represented with a linear elastic spring. Rail elements were defined at the centroid of rails along the track. The geometric properties for the rail elements were determined based on the UIC60 EN 13674-1 (2002) type rail.

The rail elements were connected to the bridge superstructure with bilinear springs. Multilinear elastic link elements available in MIDAS Civil (2012) element library have been used for this purpose. As mentioned earlier, the interaction between rail and bridge superstructure in typical TBI analysis is represented with resistance-displacement curves (RDCs). Several different RDCs that were reported based on laboratory and field measurements as well as those specified by design standards were used in the present study, as discussed in the following sections. The bilinear spring elements utilized in the numerical model were assigned initial stiffness values corresponding to the track resistance in the longitudinal direction based on the RDC considered. In the transverse and vertical directions, the rail elements were connected to the bridge superstructure through linear elastic springs with a relatively high stiffness. Spring stiffness in the vertical and transverse directions was taken to be 106 times the stiffness in the longitudinal direction, based on the approach previously used by Pertangeli and Tortolini (2008) and Lie et al. (2021). Behavior of the track-bridge interface springs in the longitudinal direction is a function of the vertical load available on the track. Thus, depending on whether there is a train loading (i.e., loaded case) or no train loading (i.e., unloaded case) present on the track, different resistance-displacement behaviors were assigned to the interface spring elements.

A 300 m embankment length on both sides of the bridge was considered for all studied cases. The track-bridge interface springs were typically provided at 1.0 m intervals. Utilizing a 1.0 m element length provides sufficiently accurate results both in terms of ARSs and displacements, as reported previously by Yang and Jang (2016). It should be noted that the embankment length and element length values utilized in the current study satisfy the corresponding limits specified in point 1.7.3 of the UIC 774-3R Code (2001) (i.e., a minimum embankment length of 100 m and a maximum element length of 2 m). For more details of the verification please see Appendix A.

2.2.2 Difference between Separate and Sequential Analysis Approaches

As specified in point 1.7.1 of UIC 774-3R (2001), the TBI response can be obtained through either a separate analysis or a sequential analysis. The separate loading approach is simply based on the application of temperature, vertical, and braking/accelerating loads separately followed by the superposition of the corresponding results. Temperature loading was applied on a model utilizing unloaded resistance-displacement behavior for the interface elements, while the vertical and horizontal loads are applied on a separate model utilizing loaded RDCs. The results from these two separate models are then superimposed to obtain the total response. Because this approach is based on the superposition of responses from two separate analyses with RDCs exhibiting nonlinear behavior, the results are only approximate. The sequential analysis approach, on the other hand, utilizes a single model, where temperature loads are applied first, followed by the application of vertical and braking/acceleration effects simultaneously with the interface elements already deformed.

A comparison of the separate and sequential analyses in terms of rail resistance-displacement response is illustrated in Figure 2.3. For the case where the loaded track resistance is reached under sequence of thermal, vertical and horizontal train loads, separate analysis indicates larger ARSs but smaller relative displacements as reported by Sanguino and Requejo (2009). Therefore, for bridges designed with rail stresses as the governing effect as opposed to displacements, using separate analysis will be a conservative approach. However, it is necessary to check the displacement results carefully if separate analysis is to be used. For simply supported test cases defined in the appendix D of UIC 774-3R, Sanguino and Requejo (2009) reported higher relative and deck displacements in sequential analysis as compared to separate analysis, indicating that linear superposition is not conservative in terms of displacements. The maximum difference between separate and sequential analyses was reported to be 28% in these test cases. Therefore, in a sequential analysis special attention should be paid to the displacements when they are close to the code specified limits. The effect that the analysis type (i.e., separate versus sequential) has on TBI response of railway bridges has been investigated earlier by several researchers (Sanguino and Requejo (2009), Widarda (2009), Ruge and Birk (2007)). The primary interest in the current study is to determine how sensitive the TBI response is to changes in RDCs with both separate and sequential analysis approaches. The initial stiffness and resistance capacity of the track-bridge interface elements depend on many factors, such as the presence and type of ballast, type of fastening system, type of sleepers, as well as the friction between these components. Li et al. (2021), gave an insight on how to consider the friction spring systems. With these multiple factors affecting the behavior of the track-bridge interface, the ability of the RDCs specified in design codes to represent the actual response requires further investigation. The current study reports the findings of such an investigation.

2.3 Longitudinal Track Resistance-Displacement Curves (RDCs)

The longitudinal track resistance-displacement curves considered in the numerical analyses conducted as part of the current investigation are shown in Figure 2.4 and Figure 2.5, respectively for the unloaded and loaded track cases. The resistance values for the RDC curves are specified in terms of resistance per unit length along the track. The curves are either based on experimental results reported in the literature or taken from the related design codes. For ballastless track, the Korean Code KR-C08080 (2014) and UIC 774-3R (2001) specify the same initial stiffness and resistance limit values for both unloaded and loaded cases. In Figure 2.4(a) the RDC reported by Yun et al. (2019) based on field measurements from a recently constructed ballasted track lies between the UIC good and moderate maintenance RDCs. The measurements were collected on a ballasted track with Pandrol e-clip fasteners and UIC60 rails supported on prestressed concrete sleepers. It should be noted that the RDC reported by Yun et al. has a yield displacement of 2.7 mm, as opposed to a 2.0 mm yield displacement in point 1.2.1.2 of RDCs specified in UIC 774-3R (2001).

Unloaded ballastless RDCs utilized in the numerical study are given in Figure 2.4(b). The RDC reported by Yang and Jang (2016) is based on the laboratory tests on tracks with resilient base plate pad type fastening system. Zhang et al. (2015) also conducted laboratory testing on ballastless tracks with a low resistance type fastener that is commonly used for urban rail transit in China. As evident in the plots, the RDC reported by Zhang et al. has slightly lower initial stiffness and approximately 50% higher resistance limit than those reported by Yang and Jang. It is noteworthy that the RDCs reported in both studies consistently fall far below the RDC specified in KR-C08080 (2014) and UIC 774-3R (2001) Codes for unloaded ballastless tracks, in terms of initial stiffness and resistance limit. In an attempt to examine the effect of changing track resistance limit with the same initial stiffness, a new RDC was proposed in this study by extending the RDC reported by Yang and Jang (2016) up to a resistance limit of 20 kN/m. This new RDC is labelled as “fictive extension” in Figure 2.4(b).

The RDCs investigated as part of the current study for loaded track condition are presented in Figure 2.5. For ballastless tracks, the RDCs reported by Zhang et al. (2015) and Yang and Jang (2016) based on laboratory measurements are provided in Figure 2.5(b) together with the RDC specified in KR-C08080 (2014) and UIC 774-3R (2001) Codes. Even though the RDCs that are based on experimental measurements have similar initial stiffness values, there is approximately 3.3 times difference between the resistance limits. This might be attributed to the fact that the vertical loads applied on the tracks to simulate the loaded track condition were different in two studies. Yang and Jang tested their track with 30 kN of vertical load on the fastening system, whereas 40 kN of vertical load was used by Zhang et al. In addition to such a difference in the amount of vertical loading applied on tracks, different fastening systems were utilized in these studies. This can be another reason for the difference in the measured resistance limits reported by Zhang et al. (2015) and Yang and Jang (2016). The RDC specified in KR-C08080 (2014) and UIC 774-3R (2001) Codes has approximately three times larger initial stiffness than the experimentally determined relations with the resistance limit in between the measured values but somehow close to the one reported by Zhang et al. (2015).

2.4 Verification of Numerical Modeling Approach

2.4.1 Verification with Analytical Solution of a Single Span Bridge under Temperature Loading

Frýba (1996) provided a closed form solution for the differential equation for TBI under temperature loading assuming a linear elastic response for the track-bridge interface elements. System of *i* bars were connected to each other to represent the bridge and CWRs. The problem was divided into four bar segments, where segments 1-3 represent the rails while segment 4 represents the bridge itself (Figure 2.6). The interface elements were assumed to be distributed along the bridge with linear spring constants (k_i) per unit length of the i^{th} bar. For the investigated case, the bridge was assumed to have a single span with one fixed and one moveable support.

It is usually assumed that rail temperature does not have any influence on the bridge since the cross-sectional area of the rail compared to bridge is significantly small (Strauss et al. (2018)), whereas a change in bridge temperature results in a change in rail stresses. The following equation is valid for each part of the investigated bar according to Hooke’s Law.

$$N = EA(u' - \alpha\Delta t) \tag{2.1}$$

where u = u(x) is the longitudinal displacement of the bar element, u' is the relative elongation (strain) of the bar, α is the coefficient of thermal extension of the bar, and $\Delta t = t\text{-}t_0$ is the temperature change with respect to initial temperature t_0.

For a bar element with length *dx*, the force equilibrium equation can be written as follows

$$-N + N + N'dx - kudx \ = \ 0 \tag{2.2}$$

where *N* = *N(x)* is the longitudinal force at location *x* on the bar element.

Equation (2.2) can be rewritten using the Hooke’s law given in Equation (2.1).

$$-EAu'' + \ ku = \ 0 \tag{2.3}$$

Solving the differential equation results in the displacements of individual segments as follows.

More details for the intermediate steps can be found in Frýba’s (1996) study.

$$u_1(x) = \frac{\alpha_0\, \Delta T}{2\lambda}\left[1 - (1 + \lambda l_2)\, e^{-\frac{\lambda}{2}}\right] e^{\lambda x}$$

$$u_2(x) = \frac{\alpha_0\, \varDelta T}{2\lambda}\left[2\lambda x + e^{-\lambda x} - (1 + \lambda l_2)\, e^{-\frac{\lambda}{2} - x}\right]$$

$$u_3(x) = \frac{\alpha_0\, \varDelta T}{2\lambda}\left(\lambda l_2 - 1 + \; e^{-\frac{\lambda}{2}}\right) e^{-\lambda x}$$

$$u_4(x) = \alpha_0 \Delta T x \tag{2.4}$$

where α_i is the coefficient of thermal extension of the rails and $\alpha_0 = \alpha_4$ is the coefficient of thermal extension of the bridge, $\lambda^2 = \lambda_i^2 \; = \frac{k_i}{E_i A_i} = \frac{k}{EA}$ assuming the same modulus of elasticity and areas for segment 1-3.

$\varDelta t$ is the difference in temperature for rail bars from initial temperature t_{i0}.

$$\Delta t = \Delta t_i = \; t_i - t_{i0}, \; for\; i = 1 - \; 3 \tag{2.5}$$

ΔT is the difference in temperature for bridge bar from initial temperature t_{40}.

$$\Delta T = \Delta T_4 = \; t_4 - t_{40} \tag{2.6}$$

The corresponding bar forces are:

$$N_1(x) = -EA\alpha\varDelta t\; \{\frac{\alpha_0\, \varDelta T}{2\lambda}\left[1 - (1 + \lambda l_2)\, e^{-\frac{\lambda}{2}}\right] e^{\lambda x}\}$$

$$N_2(x) = -EA\alpha\varDelta t\; \{\frac{\alpha_0\, \varDelta T}{2\lambda}\left[2\lambda x + e^{-\lambda x} - (1 + \lambda l_2)\, e^{-\frac{\lambda}{2} - x}\right]\}$$

$$N_3(x) = -EA\alpha\varDelta t\; \{\frac{\alpha_0\, \varDelta T}{2\lambda}\left(\lambda l_2 - 1 + \; e^{-\frac{\lambda}{2}}\right) e^{-\lambda x}\}$$

$$N_4(x) = 0 \tag{2.7}$$

The stress σ_i for each bar is determined by dividing the axial force N_i by the rail area A.

Numerical model of the bridge and track system for which the analytical solution is presented above has been created and analyzed under temperature loading following the modeling assumptions as given in Figure 2.2(a). Linear elastic springs were used for the bridge-track interface elements in the numerical model and the bridge was assigned a temperature increase of 35^0C. The geometric and material properties used in the numerical model and the analytical solution are given in Table 2.1. Comparisons between the analytical and numerical solutions are provided in Figure 2.7 in terms of ARSs and longitudinal displacements. Displacement of the bridge increases linearly from the fixed support to the movable support (Figure 2.7(c)), while the rail displacement has a nonlinear variation along the bridge (Figure 2.7 (b)). As a result of such bridge and rail displacement distributions, tensile and compressive stresses develop within the rail with the distribution shown in Figure 2.7(a). As evident, the maximum compressive rail stress occurs at the movable support location, while the maximum tensile stress occurs at a location between the fixed support and midspan. The agreement between the two sets of results in terms of displacements and rail stresses indicates that the assumptions and the element size adopted in the numerical model are acceptable for the investigated problem.

2.4.2 Verification with Measured Response from Multi-span Bridge with Unloaded Ballasted Track

Rail displacements, ARSs, and relative displacements between rail and bridge have previously been monitored by Yun et al. (2019) on a ballasted track. The studied bridge has 38 simply supported spans with each span consisting of 25 m long precast/prestressed concrete girders. The investigation by Yun et al. (2019) focused on the final span of the bridge, which is the most critical span in terms of TBI under thermal loading. As part of the current study, the last six spans of the same bridge that had previously been monitored by Yun et al. (2019), was modeled based on the geometric and material properties given in the study. This is done in order to increase modeling efficiency since after 6 spans the analysis results converged to same relative displacement and ARSs. According to the measurements reported by Yun et al. the rail-bridge attachment devices have a longitudinal resistance limit of 18 kN/m and a corresponding longitudinal displacement of 2.7 mm. Numerical analyses discussed in this section utilized the RDC values that are based on the authors' measurements.

Rail stresses and relative displacements between the bridge deck and the rail are compared, respectively in Figure 2.8(a) and Figure 2.8(b). The figures show the numerical results from the current study and the measured values reported by Yun et al. (2019) for a temperature drop of 10^0C, 20^0C, and 30^0C in the bridge deck which were retrieved from daily temperature change data collected on site. Due to temperature decrease in the bridge deck, the bridge contracts in each span at the roller support location. As a result of this motion, the relative displacement between the bridge deck and the rail changes sign within each span. The amount of rail stress that develops as a result of bridge temperature change depends directly on the level of relative longitudinal displacement between the bridge deck and the rail. A comparison of Figure 2.8(a) and Figure 2.8(b) indicates that relatively small stresses develop within the rail at locations where the deck-rail relative displacements are small (i.e., near midspan location). Similarly, largest relative displacements occur at the right end (i.e., roller support) of the investigated span, and this results in relatively large rail stresses at this location. The numerically determined rail stresses provide an accurate estimation of the measured values along the final span of the bridge and the abutment. As for the relative displacement between the rail and the deck, the numerical results underestimate the measured values at the roller support of the last span.

Effect of the temperature drop within the bridge deck on the ARSs is shown in Figure 2.9 at four different locations along the investigated span of the bridge. For all four locations considered, ARSs increase almost linearly with increasing temperature drop applied to the bridge deck. The rate at which ARSs change with temperature drop increases when moving from the midspan location towards the right support. As depicted in Figure 2.8 2.8 and 2.9, the numerically predicted relative displacements and ARSs agree well with the trend that is based on the measured values.

The final span of the bridge reported by Yun et al. was further analyzed under a temperature decrease of 30^0C by considering both the moderate maintenance and good maintenance ballasted RDCs specified in point 1.2.1.2 of UIC 773-4 (2001), in addition to the RDC that is based on measurements. As mentioned earlier, Yun et al. (2019) reported a resistance limit of 18 kN/m and a corresponding longitudinal displacement of 2.7 mm based on their measurements on the bridge. For ballasted tracks under unloaded condition with good maintenance UIC 774-3R (2001) specifies 20 kN/m resistance limit and 2 mm longitudinal displacement. The resistance limit drops to 12 kN/m for the case of moderate maintenance. The relation between these three RDCs is shown in Figure 2.4(a). Results from the analyses performed by utilizing these three RDCs are presented in Figure 2.10. The type of RDC does not have an appreciable effect on relative displacements as presented in Figure 2.10(b). However, the corresponding rail stresses are affected to a certain degree. As evident, the level of ARSs developing as a result of similar levels of rail-deck relative displacements depends on resistance and stiffness levels of the RDC used. The maximum difference in ARSs is 14% when the RDC proposed by UIC for good maintenance track is used instead of the RDC reported by Yun et al. In this case, the UIC RDC produces more conservative values. The RDC proposed by UIC for moderate maintenance track, on the other hand, resulted in 15% lower maximum rail stress than the experimental RDC reported by Yun et al. The results indicate that for this specific bridge with 25 m long simply supported concrete girders, utilizing the RDC that is specified in point 1.2.1.2 of UIC 774-3R (2001) for good maintenance tracks is conservatively acceptable in the absence of measured data from monitoring of the tracks.

2.5 Parametric Investigation

In order to investigate the effect of major parameters on TBI, additional numerical analyses were conducted on the precast concrete girder bridge reported by Yun et al. (2019) considering both ballasted and ballastless track cases. Similar to the model used for the experimental verification study, the last six spans of this bridge were modeled based on the geometric and material properties given by Yun et al.(2019). As part of the investigation, the RDCs given in Figures 2.4 and 2.5 were utilized with 35^0C thermal loading in bridge deck, as well as vertical and horizontal (i.e., braking and acceleration) loadings. For ballasted track condition, the UIC moderate maintenance RDC and the RDC reported by Yun et al. (2019) were not included in the analyses, as they cannot be used in loaded track case.

Two tracks were considered on the bridge for vertical and horizontal loadings, and the loading arrangements were adjusted such that maximum compressive ARS occurs at roller support location of the last span. Accordingly, positive temperature loading was considered together with braking/acceleration force directions and train positions indicated in Figure 2.11. As indicated, the train on track-2 is 30 m into the bridge and creates an acceleration force of 33 kN/m, while the front end of the train on track-1 is about to leave the bridge with a braking force of 20 kN/m. A uniformly distributed load of 80 kN/m was used for vertical moving loading based on LM71 train model. For longitudinal loading, acceleration force was taken as 33 kN/m for 30 m and braking force was taken as 20 kN/m for 300 m as per UIC 774-3R (2001). It is worth mentioning that the horizontal braking/acceleration forces as well as the vertical loading values employed in the analyses are those specified in point 1.4.3 by UIC 774-3R (2001) and Annex G of EN 1991-2 (2003).

2.5.1 Effect of RDC on ARSs and Relative Displacements

ARS distributions under various loading effects are presented in Figure 2.12, both for the cases of ballasted and ballastless track. An increase in maximum compressive ARS is observed under temperature loading with increasing initial stiffness of RDC. Among all unloaded RDCs considered, the one specified in UIC 774-3R (2001) and KR-C08080 (2014) for ballastless track has the largest stiffness of 80kN/mm/m. On the other hand, the RDC that has the smallest stiffness (i.e., 10 kN/mm/m) is the one specified in point 1.2.2 by UIC 774-3R (2001) for ballasted track with good maintenance. These two RDCs, representing the largest and smallest stiffness, result in respectively 39.9 MPa and 23.7 MPa additional compressive stress in rails under a temperature increase of 35^0C in bridge deck. The ratio of the maximum and minimum thermal ARS values is 1.68, which is much smaller than the stiffness ratio of the two RDCs. The reason for the amount of change in ARSs being much smaller than the difference in the RDC stiffness is due to the track-bridge interface spring elements reaching the resistance limit (i.e., “yielding”) under the effect of considered loading and undergoing significant relative displacements. Variation of track-bridge relative displacements along the span length under thermal loading is illustrated in Figure 2.13(a) and Figure 2.13(b) for the two RDCs specified in point 1.2.1.2 by UIC 774-3R (2001) for ballasted track with good maintenance and ballastless track. The span length was divided into five equal segments and the range of track-bridge relative displacements within each segment is indicated on the corresponding RDC curve. As evident, all track-bridge interface spring elements in segment-4 and segment-5 reached the resistance limit for both RDCs. In the case of ballastless track, segment-1 also reached the resistance limit. This is due to the lower displacement resistance limit of 0.5 mm for ballastless track. For segment-2, ballasted track spring elements remain in the linear elastic zone, whereas a portion of the elements reached the resistance limit in the case of ballastless track.

ARS distribution under vertical moving loading is given in Figure 2.12(b). Results are provided only for track-2, because vertical loading on this track creates the most unfavorable condition due to the neighboring span being only partially loaded (Figure 2.11). As evident in Figure 2.12(b) stiffness of track-bridge interface elements has a profound impact on the compressive ARSs for vertical moving loads. On the other hand, the resistance value in loaded RDCs does not have an appreciable influence on the resulting ARSs. This is because of the fact that under vertical moving loading the interface elements mostly remain within the initial linear portion of the corresponding RDC.

ARS behaviors with changing RDCs under braking and acceleration forces are presented in Figure 2.12(c)-(e). Longitudinal forces created on rails due to acceleration and braking of trains are transferred from rail to bridge deck based on the RDC stiffness. Plots in Figure 2.12(c)-(e) indicate that the RDC with higher initial stiffness (i.e., the one specified by KR-C 08080 and UIC 774-3R) results in smaller rail stress under braking and acceleration forces than the other RDCs. The reason is that this RDC develops the resistance capacity under a relatively small relative displacement of 0.5 mm and results in large slip between rail and bridge deck, which in turn causes relatively small ARSs. Furthermore, the RDC with higher yield displacement capacity (i.e., the one suggested by Zhang et al. (2015)) creates higher rail stress than the other RDCs due to delayed yielding. This behavior is observed for the loading cases of braking on track-1 (Figure Figure 2.12(c)) and acceleration on track-2 (Figure Figure 2.12(d)), as well as the simultaneous application of these two loadings (Figure Figure 2.12(e)).

The total ARSs are determined as the summation of stresses due to temperature, vertical, and braking/acceleration loadings. Total ARS distributions determined this way are shown in Figure Figure 2.12 (f). Among all loadings, the largest portion of ARSs is caused by thermal loading. Another observation is that ARS in none of the cases exceeds the compressive stress limit of 72 MPa defined in point 1.5.2 by UIC 774-3R (2001).

2.5.2 Effect of Span Length on ARSs and Relative Displacements

As mentioned in the previous section, temperature loading contributed the most to the total ARS in the investigated bridge. The thermal component of the ARS changes directly in relation with the expansion length. In order to investigate the effect of expansion length on ARS due to different loading components, the bridge reported by Yun et al. (2019) was further investigated by changing the span length from 25 m to 40 m with 5 m increments. The maximum span length was considered to be 40 meters due to the practical span limit of precast girder bridges. The parameters regarding material and section properties were based on the following assumptions. The cross-sectional dimensions of the bridge was increased with increasing span length such that the ratio of vertical displacement to span length under uniformly distributed load remains constant. The cross-sectional area and total height of the bridge cross section were increased linearly with the span length. Relative location of the center of gravity of the bridge cross section was kept constant in relation to the section height. The parameters determined based on these assumptions are tabulated in Table 2.2. It should be mentioned that a modulus of elasticity value of 35.22 GPa was used for the bridge superstructure to represent the C40 grade concrete.

Maximum compressive ARS results are plotted in Figure 2.14. As evident, the total rail compressive stress is dominated by thermal stresses. The rail stress due to temperature loading corresponds to 56% of the total stress in 25 m span length, whereas it increases to 63% for 40 m span length, indicating that after a certain point rail stresses due to braking/acceleration and vertical loadings are not increasing as much as the thermal loading. Increasing the span length for simply supported bridges leads to an increase in the expansion length, which affects thermal stresses the most. The higher increase in the thermal stresses may also be attributed to obvious increase of the cross-sectional area of the bridges as the span length increases.

Similar to the ARS, a significant portion of the total displacements is produced by the thermal loading. Temperature loading contributes to 84% to 86% of the total bridge top deck displacement, and 82% to 86% of the total deck-rail relative displacement depending on the span length. Braking/acceleration loading produces very small bridge top deck displacement and deck-rail relative displacement with almost no change with the span length. Therefore, the impact of the span length on the relative displacements due to braking/acceleration and vertical loadings is insignificant.

2.5.3 Effect of Substructure Stiffness on ARSs and Relative Displacements

Another design parameter that has an impact on TBI response is the longitudinal stiffness present at bridge supports. Petrangeli and Tortolini (2008) stated that longitudinal stiffness of a short abutment/pier roughly corresponds to 100 mN/m/m. Based on this substructure stiffness value, additional analyses were conducted on the test bridge reported by Yun et al. (2019) with different substructure stiffness levels using the RDC specified in point 1.2.1.2 by UIC 774-3R (2001) for ballasted track. It should be noted that, the analyses mentioned in previous sections utilized idealized roller and pin boundary conditions. In addition to these idealized boundary conditions, the bridge model was also analyzed with linear elastic springs provided at girder supports to represent the substructure stiffness. Two spring stiffness values of 2500 mN /m (25 m span x 100 mN/m/m) and 250 mN /m (25 m span x 10 mN/m/m) were utilized in these analyses. The bridge model was further analyzed with bridge piers and elastomeric girder supports included in the model instead of the elastic springs simulating the substructure stiffness. This type of modeling approach is believed to represent the actual substructure response more accurately. In these analyses two pier heights of 2 m and 10 m were used together with 2 m diameter circular pier cross section. The 2 m and 10 m heights can be considered to represent a short and medium length pier, respectively.

ARS results from the bridge models mentioned above are plotted in Figure 2.15(a) to Figure 2.15(f). Maximum ARSs under thermal loading vary between 18.9 and 23.4 MPa (Figure 2.15(a)), with the largest ARSs occurring with idealized roller and pin girder boundary conditions, and the smallest ARSs occurring with 10 m tall piers. Any increase in bridge substructure stiffness provides a larger restraint at girder supports against longitudinal movement, which in turn, results in larger rail stresses under temperature loading. Similar result is also valid for vertical loading, as shown in Figure 2.15(b). This is due to the increased substructure stiffness resulting in higher top deck displacement, which leads to higher ARS.

The effect of substructure stiffness on rail stresses due to braking/acceleration loading is different than that of temperature and vertical loading. As braking/acceleration loading is applied directly on rails any increase in substructure stiffness results in smaller rail stresses. This is the reason for the model with 10 m tall piers (i.e., the model with smallest substructure stiffness) having the largest maximum compressive ARS among all cases studied (Figure 2.15(c)-Figure 2.15(e)). Under the combined effect of braking on track-1 and acceleration on track-2, maximum compressive ARSs vary between 12.1 to 35.4 MPa (Figure 2.15 (e)). Such a variation indicates that substructure stiffness has a significant influence on ARSs under braking/acceleration loading.

Variation of ARSs along the bridge span under the combined effect of all loadings (i.e., thermal, vertical and braking/acceleration) with all studied substructure stiffness levels is presented in Figure 2.15(f). Maximum compressive rail stress occur in models with 10 m tall piers and 250 mN/m support stiffness. It is worth to note that none of the ARSs exceeds the compressive stress limit of 72 MPa defined in point 1.5.2 of UIC 774-3R (2001). A comparison of the stress plots in Figure 2.15(f) indicates that the 100 mN/m/m longitudinal stiffness as suggested by Petrangeli and Tortolini (2008) is a proper representation of stiffness level for short piers (i.e., 2 m pier height with 2 m diameter circular pier cross section). For the bridge model considered, the idealized pin and roller girder support conditions closely represent this substructure longitudinal stiffness level. As evident in the plots, in the presence of medium length or slender piers, braking/acceleration loading becomes the dominant effect in terms of rail stresses. It should be noted that using idealized pin and roller girder support conditions without modeling the support stiffness leads to unconservative rail stress estimates. This is mainly due to the effects caused by braking and acceleration forces getting larger when bridge piers are of medium or high slenderness, as discussed previously by Wenner et al. (2019).

2.6 Comparison of Separate and Sequential Analysis Results

As illustrated in Figure 2.3 separate and sequential analyses might lead to different track-bridge interaction responses. This difference may be especially critical in the cases where the ARSs are close to the limits specified in the standards. In order to investigate the extent of difference between the responses obtained with separate and sequential analysis approaches, the verified numerical model of the bridge monitored by Yun et al. (2019) was further studied. Table 2.3 shows the analysis parameters used for this purpose. In these analyses, thermal loads were defined as 35^0C increase in the bridge deck and the train loadings were applied on the numerical model as illustrated in Figure 2.11.

The level of difference between separate and sequential analysis results was analyzed with different support conditions, span lengths, and RDC behaviors. Results of this investigation are presented in Figure 2.16(a)-(d) in terms of total ARSs. There is no appreciable difference in ARS values from separate and sequential analyses for the case of ballasted track, irrespective of the span length and support condition. Among the cases investigated, the largest difference between ARS values from separate and sequential analyses occurs when ballastless track is considered and the substructure stiffness is included in the analysis model. With 250 MN/m support stiffness (i.e., equivalent to a stiffness of 10 MN/m per meter of span length) and 25 m span, the maximum compressive ARS is 68.5 MPa and 62.8 MPa, respectively for separate and sequential analyses (Figure 2.16(b)). The reason of having 9% difference between these two ARS values can be explained by the yielding of the longitudinal RDCs. The RDCs exceed the 0.5 mm resistance limit with a support stiffness of 250MN/m. As a result, the displacements under vertical and longitudinal moving loads result in higher deck-rail relative displacements, which in turn, leads to additional force in the loaded track in the case of separate analysis. A similar behavior is also valid for the span length of 40 m. When this span length is considered together with a ballastless track and 400 MN/m support stiffness (i.e., equivalent to a stiffness of 10 MN/m per meter of span length) the maximum ARS of 84.6 MPa and 76.9 MPa is obtained, respectively from sequential and separate analyses (Figure 2.16(d)). These values indicate an increase of 10% in the maximum compressive ARS when changing the analysis method from separate to sequential. Even though, this much increase may seem insignificant, conducting a sequential analysis can eliminate using rail expansion joints for threshold bridges.

The results presented in Figure 2.16 indicate that performing a separate analysis instead of a sequential analysis does not result in an appreciable difference in ARS values for ballasted tracks and for ballastless tracks over bridges with relatively high substructure stiffness. It should be noted that the maximum compressive ARSs presented in Figure 2.16(b) remain below the compressive stress limit of 72 MPa defined in point 1.5.2 of UIC 774-3R (2001), while those in Figure 2.16(d) exceed this limit, irrespective of whether a sequential or a separate analysis is used.

Table 2.1 Material and geometrical properties used in verification of the numerical model with analytical solution

Element	Description	Properties
Rail	Cross sectional area, A (m^2)	0.1534
	Elasticity modulus, E (kN/m^2)	2.1 x 10^8
	Thermal expansion coefficient, α_i (/^{0}C)	1.0 x 10^{-5}
	Rail length on span, l_2 (m)	60
Bridge	Span length, l_4 (m)	60
Embankment	Embankment length, l_1, l_3 (m)	100
Spring	Spring constant per unit length, k_i (kN/m^2)	1 x 10^5

Table 2.2 Parameters used for various span lengths

Span length, L (m)	25	30	35	40
Moment of inertia, I (m^4)	7.19	12.42	19.73	29.45
Area, A (m^2)	11.09	19.16	30.42	45.41
Depth of girder, D (m)	2.60	3.12	3.64	4.16
L / D	9.62	9.62	9.62	9.62
Center of gravity from bottom (m)	1.70	2.04	2.38	2.72

Table 2.3 Analysis parameters used for comparison of separate and sequential analysis results

Span Length (m)	Support Condition	RDC
25	Pin-Roller	UIC 774-3R (2001) Ballasted
25	250 mN/m	UIC 774-3R (2001) Ballasted
40	Pin-Roller	UIC 774-3R (2001) Ballasted
40	400 mN/m	UIC 774-3R (2001) Ballasted
25	Pin-Roller	UIC 774-3R (2001) KRC 08080 (2014) Ballastless
25	250 mN/m	UIC 774-3R (2001) KRC 08080 (2014) Ballastless
40	Pin-Roller	UIC 774-3R (2001) KRC 08080 (2014) Ballastless
40	400 mN/m	UIC 774-3R (2001) KRC 08080 (2014) Ballastless

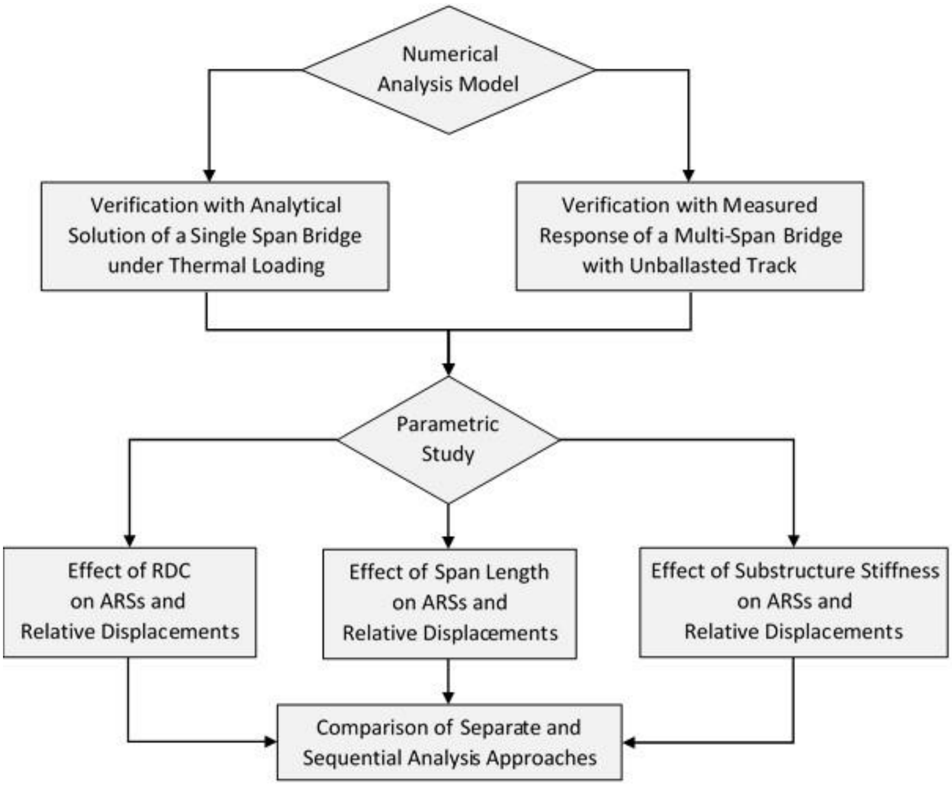

Figure 2.1. Flowchart of analysis steps

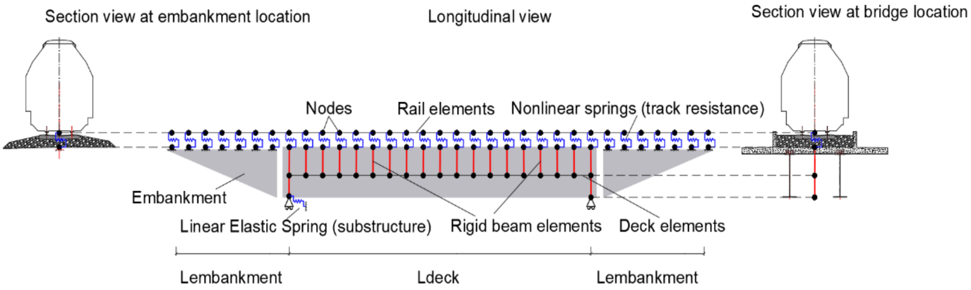

(a)

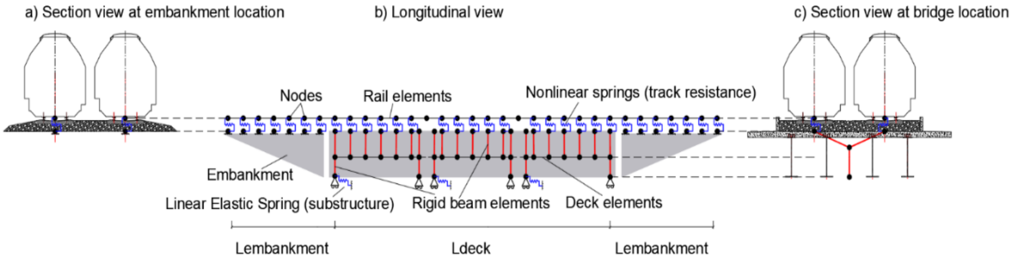

(b)

Figure 2.2. Details of modeling for (a) single-span single-track bridge (b) multi-span double-track bridge

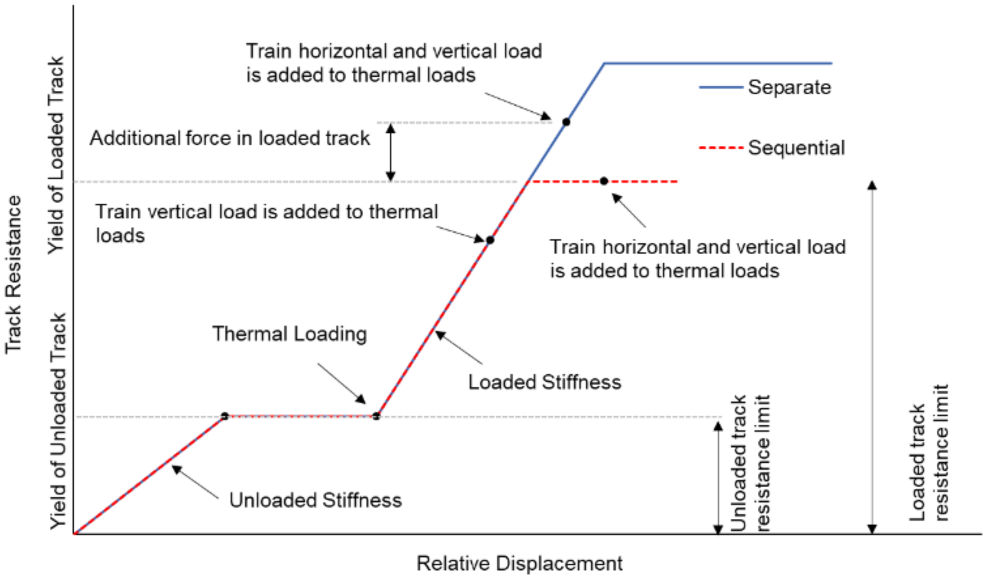

Figure 2.3. Track resistance-displacement responses for separate and sequential analyses (based on MIDAS Civil Manual (2012))

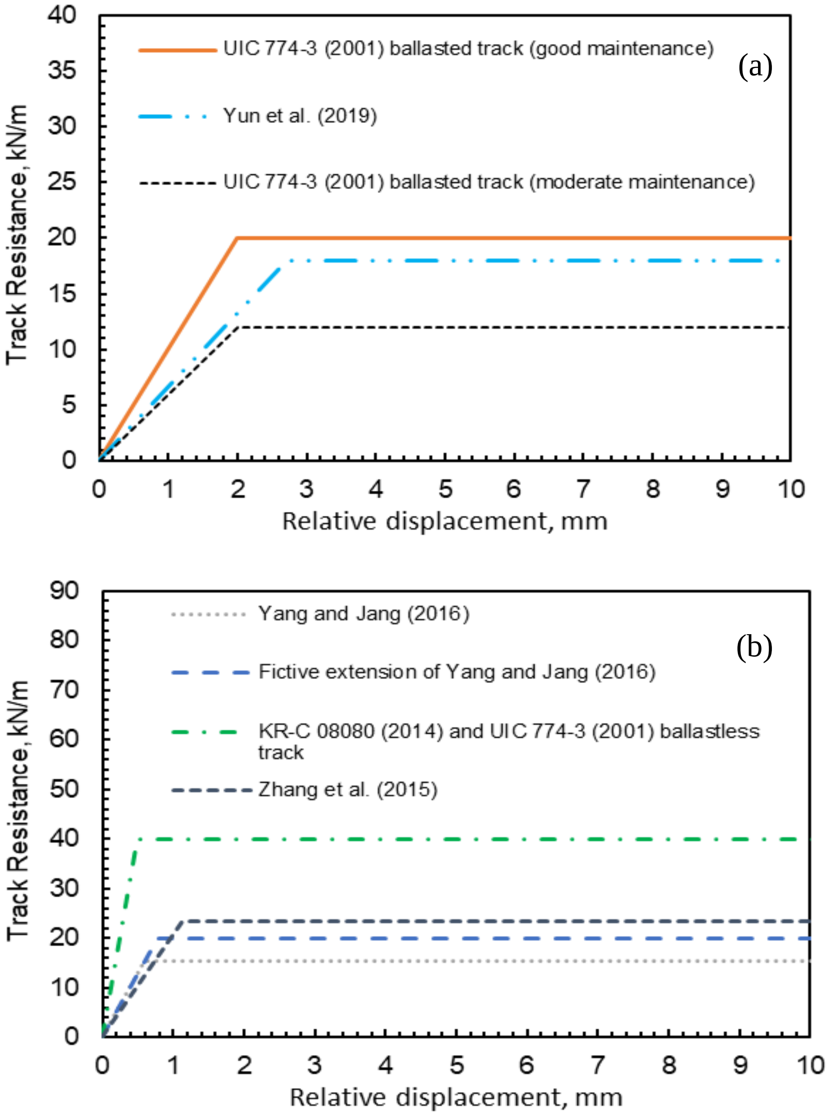

Figure 2.4. Longitudinal resistance-displacement curves considered in the current study for unloaded track condition: (a) ballasted track, (b) ballastless track

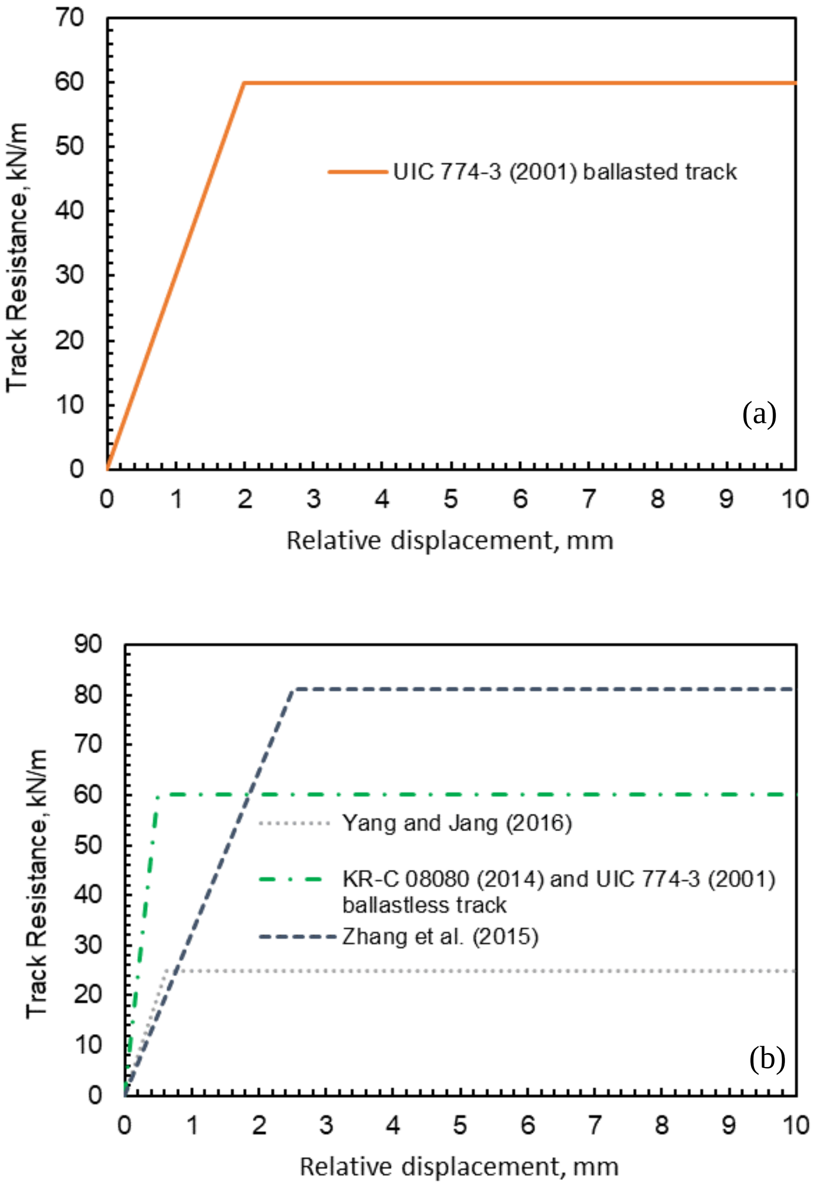

Figure 2.5. Longitudinal resistance-displacement curves considered in the current study for loaded track condition: (a) ballasted track, (b) ballastless track

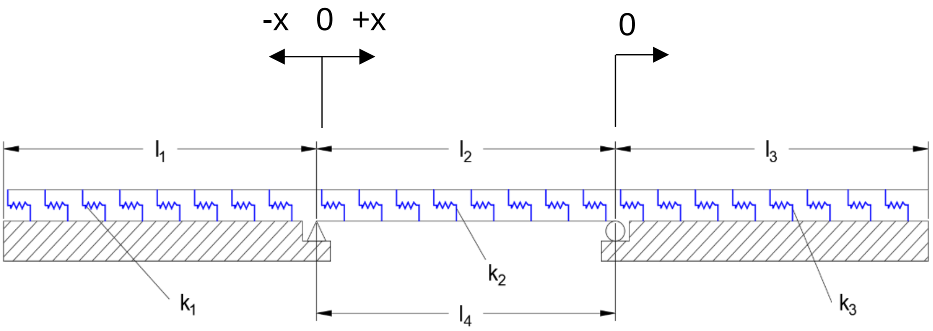

Figure 2.6. Modeling of railway bridge used for verification with analytical solution under temperature loading

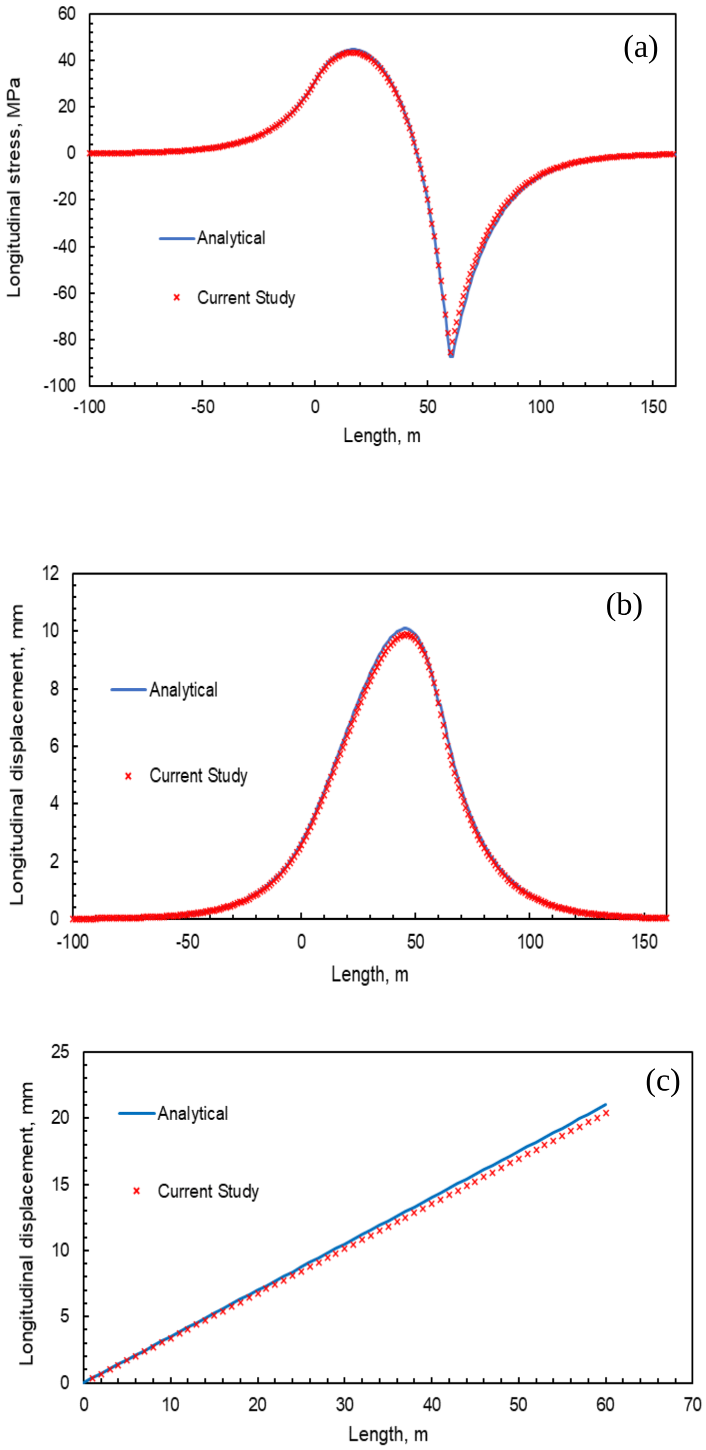

Figure 2.7. Comparison of numerical result with analytical solution: (a) rail stresses; (b) rail displacements; (c) bridge displacements

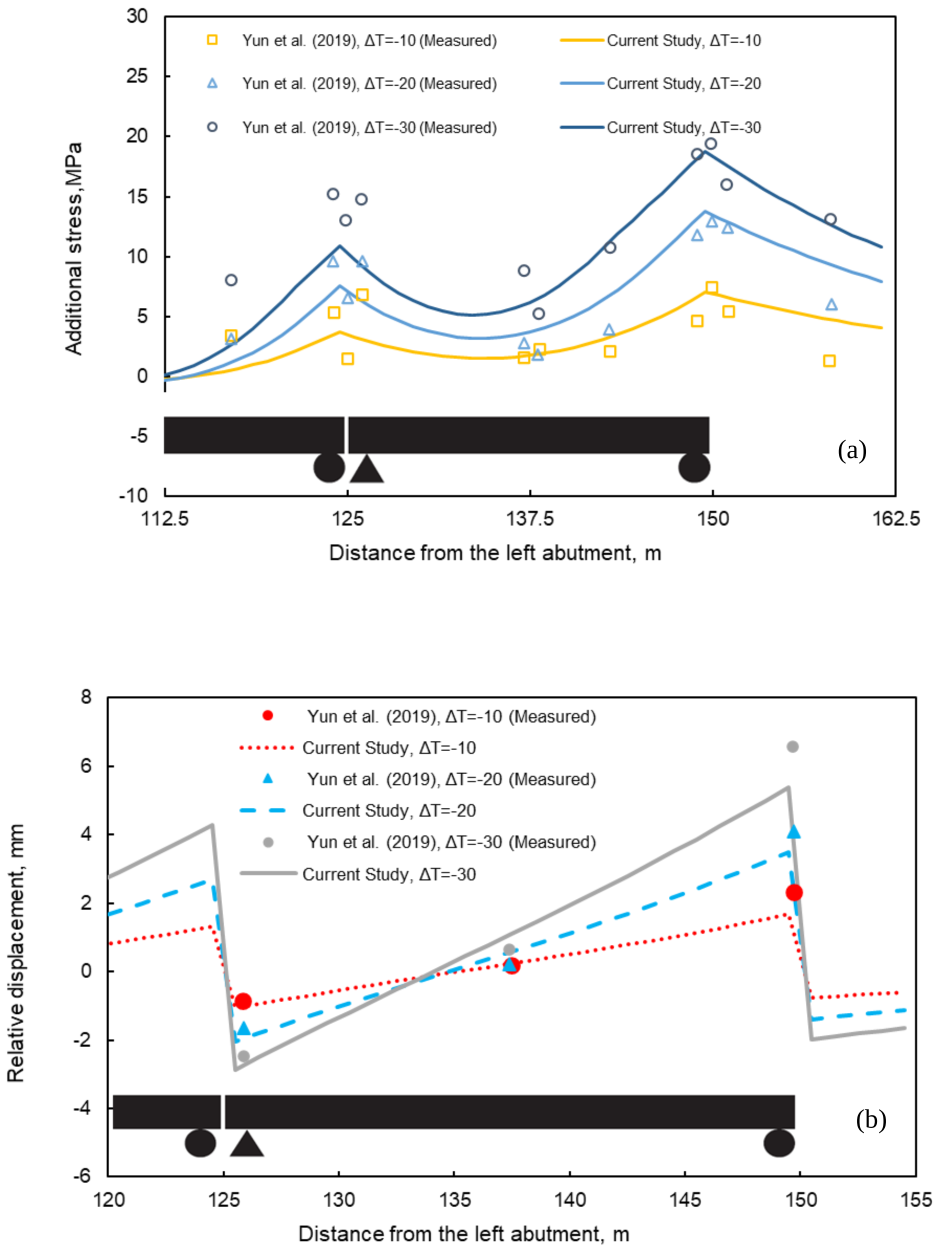

Figure 2.8. Variation of (a) additional rail stress; (b) bridge-rail relative displacement along span for the bridge studied by Yun et al. (2019)

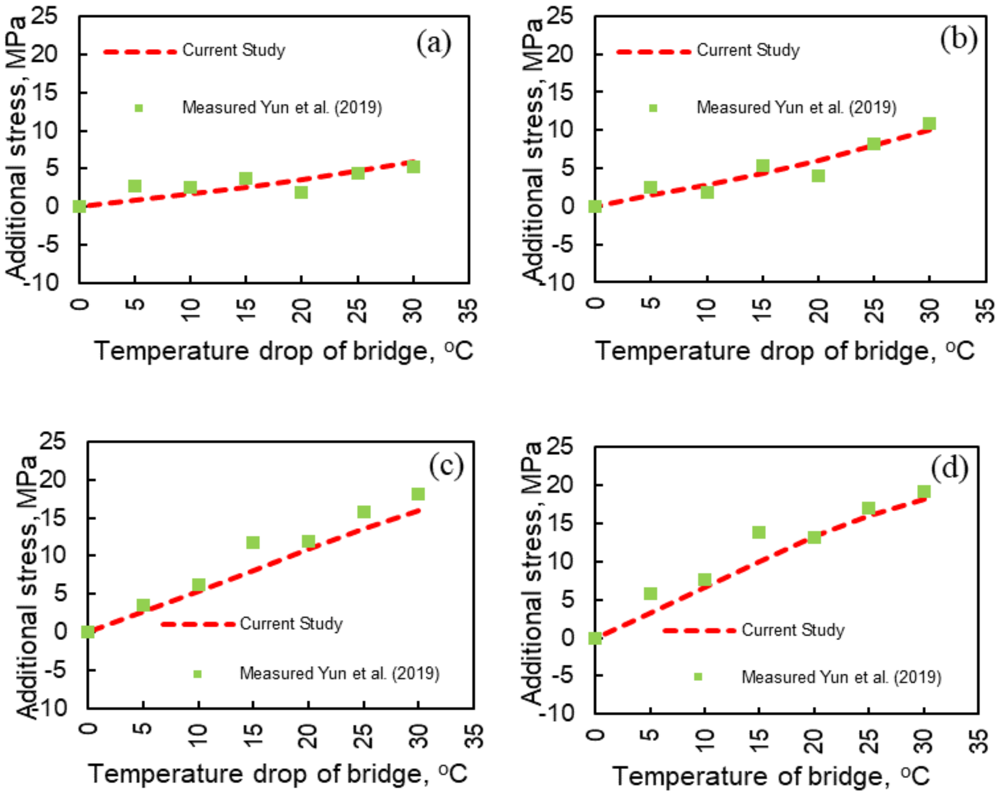

Figure 2.9. Variation of ARS for the bridge studied by Yun et al. (2019) with temperature change at (a) 13 m, (b) 18m, (c) 24m, (d) 25m from left end of the last span

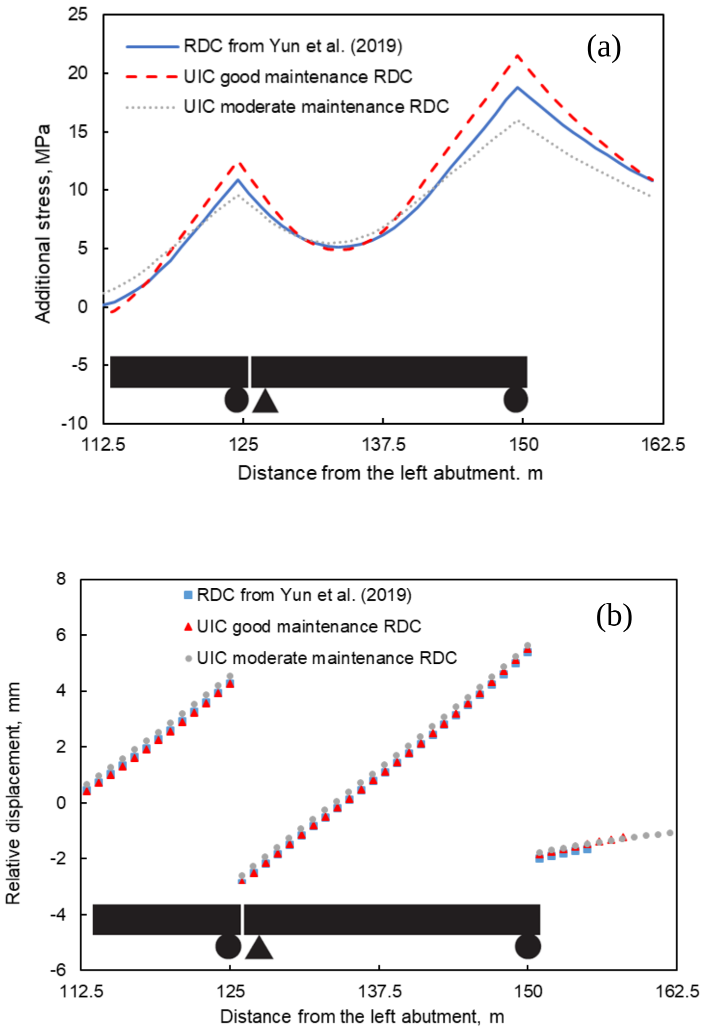

Figure 2.10. Effect of RDC for the bridge studied by Yun et al. (2019): (a) ARS, (b) rail-deck relative displacement

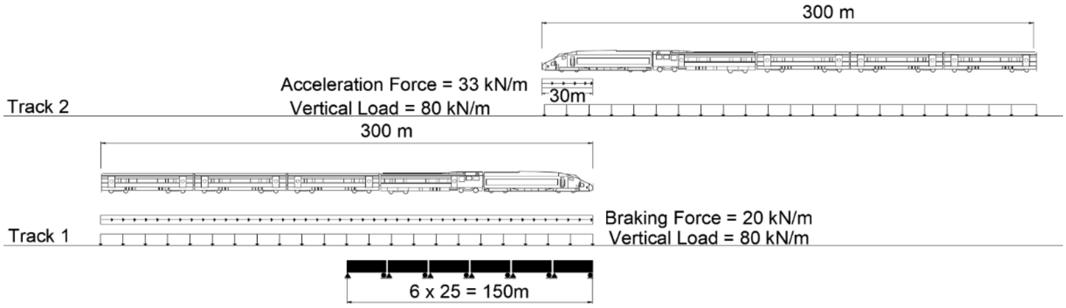

Figure 2.11. Train loading positions considered in numerical models

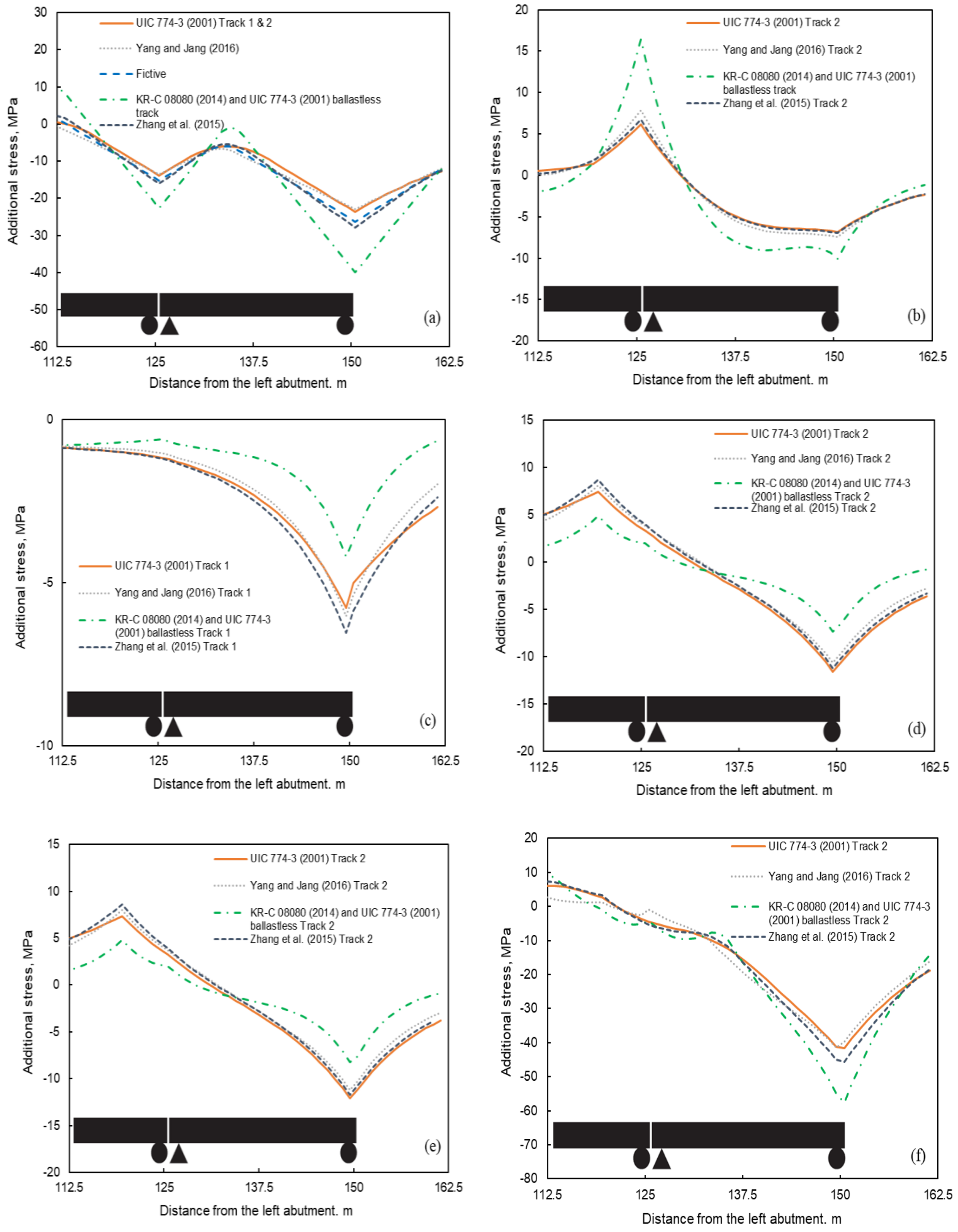

Figure 2.12. ARS distributions with ballastless track (a) thermal loading, (b) vertical loading, (c) braking on track-1, (d) acceleration on track-2, (e) braking on track-1 and acceleration on track-2, (f) total

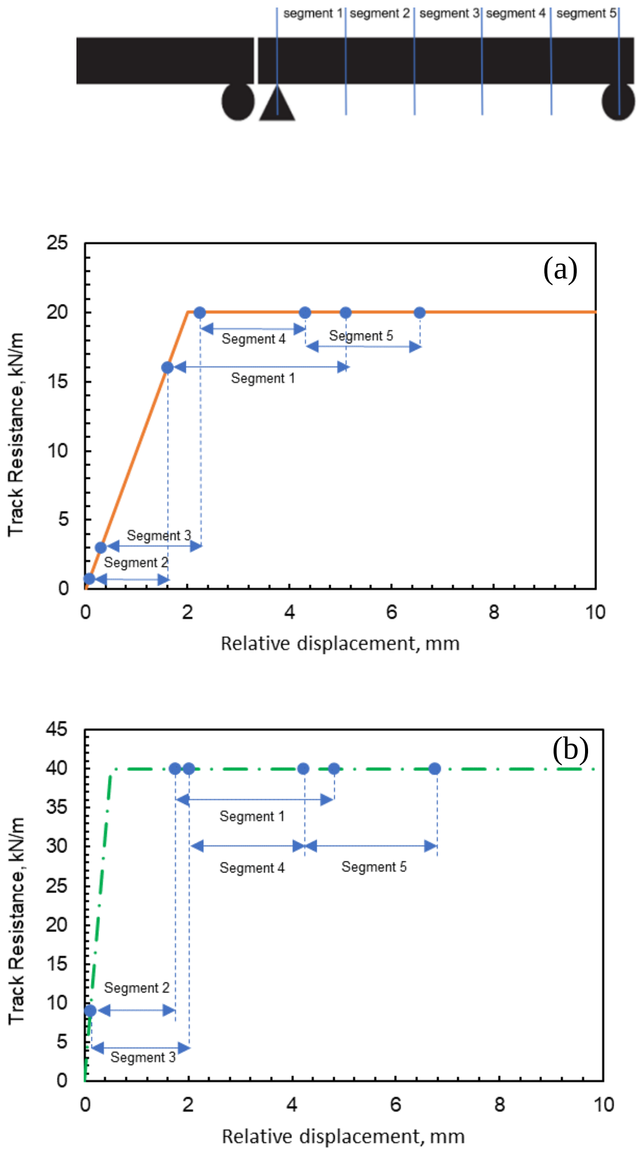

Figure 2.13. Range of track/deck relative displacements along bridge span with (a) UIC 774-3R (2001) ballasted track RDC with good maintenance, (b) UIC 774-3R (2001) and KR-C08080 (2014) ballastless track RDC

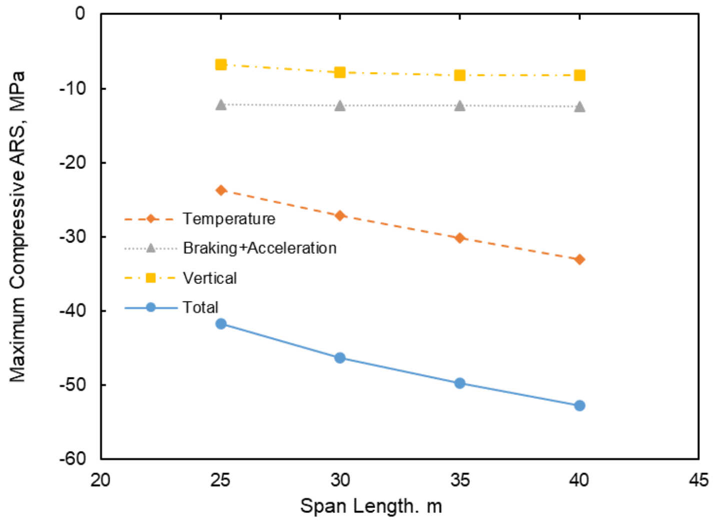

Figure 2.14. Maximum compressive ARS distribution with different span lengths

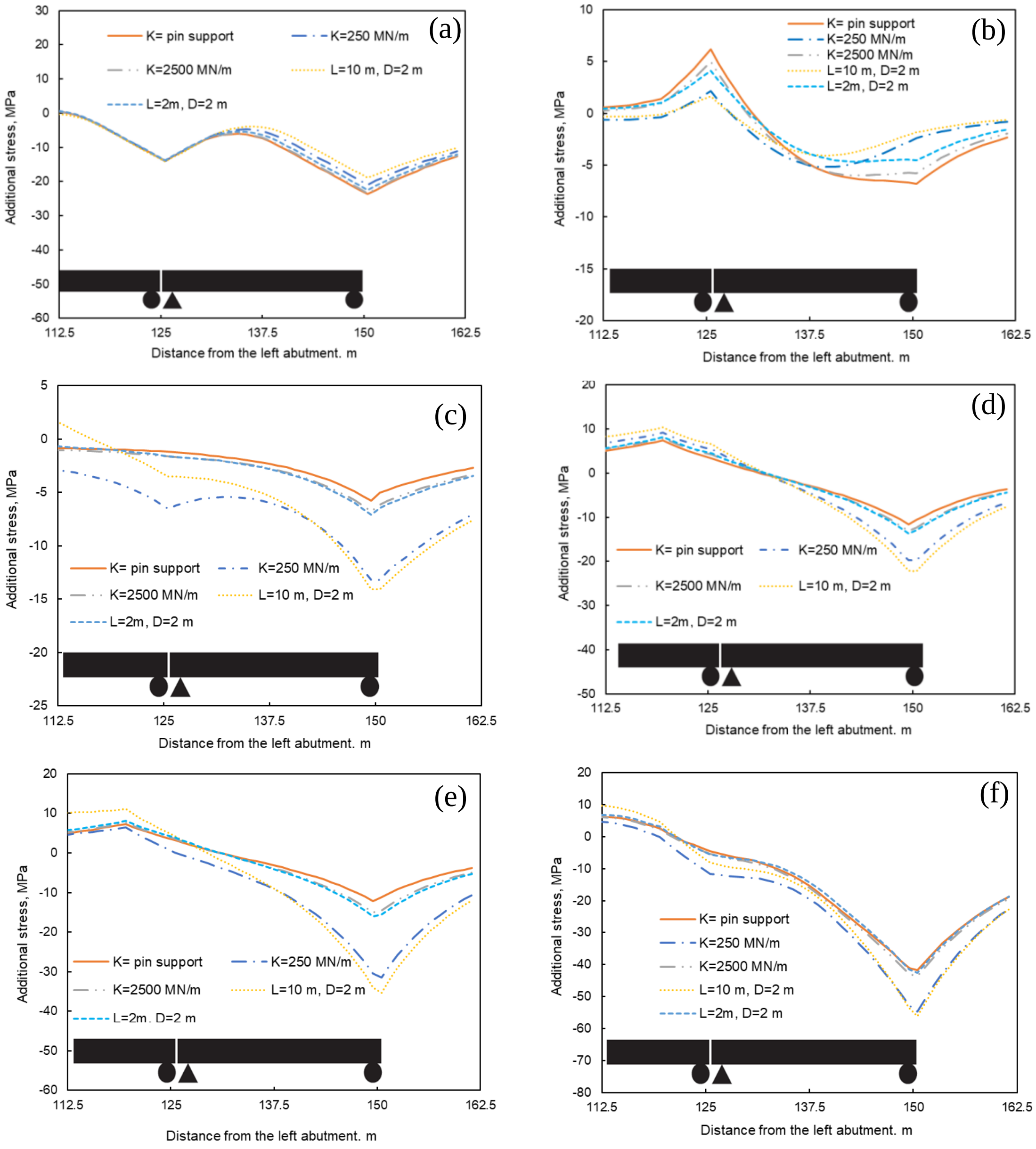

Figure 2.15. Effect of substructure stiffness ARS distribution: (a) thermal loading, (b) vertical loading, (c) braking on track-1, (d) acceleration on track-2, (e) braking on track-1, acceleration on track-2, (f) total

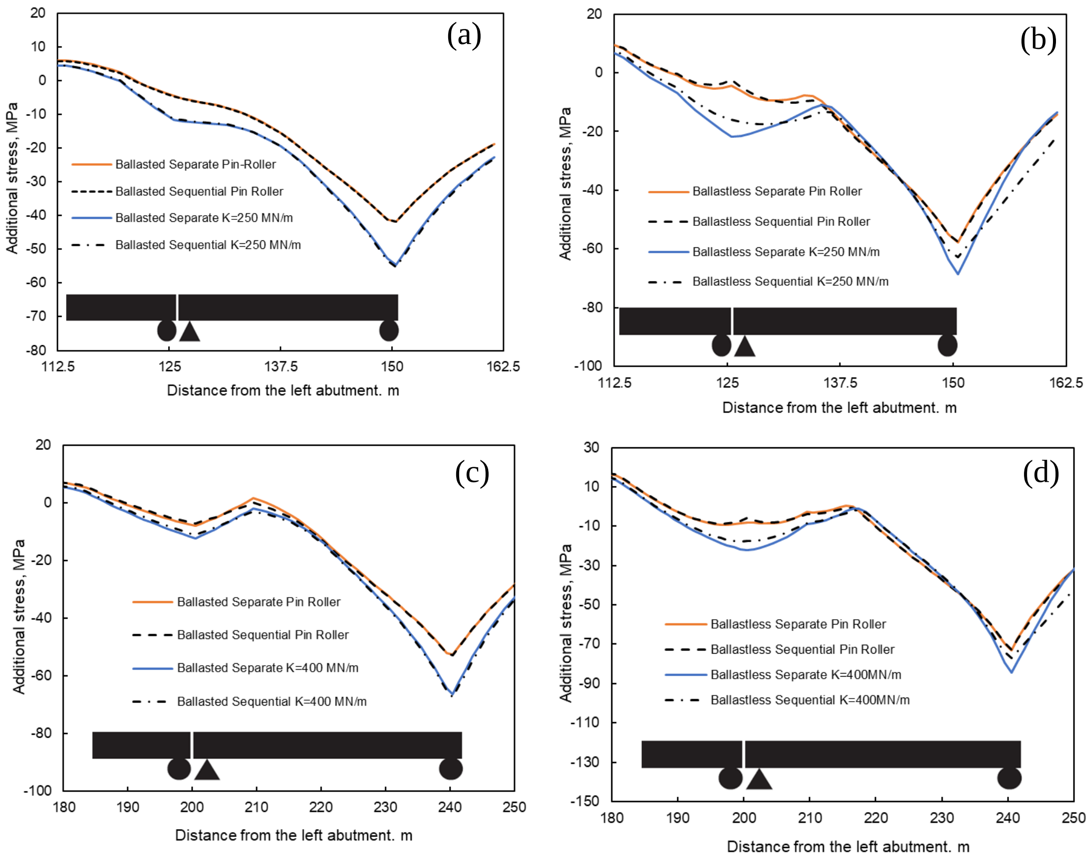

Figure 2.16. Effect of separate vs sequential analysis on ARS distribution: (a) ballasted 25 meter span, (b) ballastless 25 meter span, (c) ballasted 40 meter span, (d) ballastless 40 meter span

CHAPTER 3

INVESTIGATION OF LONGITUDINAL TRACK BRIDGE INTERACTION IN RAILWAY BRIDGES UNDER SEISMIC GROUND MOTION

3.1 Introduction

TBI analysis is extensively employed in bridge engineering practice to evaluate the impact of the interaction between rails and the bridge structure on ARSs and rail-deck relative displacements. Established railway bridge design standards, including UIC 774-3R (2001) and EN-1991-2 (2003), set forth limitations on both the ARSs and relative displacements caused by different loading sources. The primary aim of these design standards is to ensure the structural integrity and safety of railway bridges under such operational conditions. The loadings specified in design standards include thermal effects resulting from temperature differences between rail and deck, as well as the acceleration, braking forces, and vertical bending effects induced by passing trains. The loadings to be considered in TBI analysis and the corresponding permissible stresses and displacements date back to an ERRI (1997) project titled “Improved knowledge of forces in CWR track”. However, seismic actions were not considered as a load effect in this project, therefore the outcomes are primarily applicable to railway systems located in regions with lower seismic activity. Among the relevant national guidelines, Technical Memorandum Track-Structure Interaction TM 2.10.10 (2010) reported by California High-speed Rail Authority includes a specific load case, which is identified as lower-level design earthquake, for superposition of earthquake and train loads. For this load case, designers are allowed to increase the allowable rail stress limits from 68 MPa to 137 MPa for compression and from 89 MPa to 165 MPa for tension. Taiwan High-Speed Railway Provision (2000) is another national design code that considers seismic loading as part of TBI investigation. This design document utilizes an equivalent service earthquake, which is defined as one-third of the repairable damage earthquake, and combines the seismic loading with thermal and train loadings. Similar to TM 2.10.10 (2010), the Taiwan Code (2000) also increases ARS and relative displacement limits when considering the earthquake loading. While both aforementioned national guidelines incorporate seismic loading in TBI analysis, it is worth noting that this loading has not been included in international standards such as UIC 774-3R (2001) and EN-1991-2 (2003).

Several experimental and numerical studies have been reported on the longitudinal aspect of TBI under thermal and train load effects during the past two decades (Sanguino and Requejo (2009), Chen et al. (2013), Ruge and Birk (2007), Ramos et al. (2019), Sung and Chang (2019), Ryjáček and Vokáč (2014), Yan et al. (2012), Yun et al. (2019), Yang and Jang (2016), Dai et al. (2020), Zhang et al. (2015), Liu et al. (2021), Kang et al. (2021)). Results from these studies have made significant contribution to the understanding of TBI phenomenon under the effects of thermal and train loadings. However, there is still an ongoing need for extensive investigation of TBI with the presence of seismic loading. This need is particularly critical as high-speed railways with CWR (continuously welded rail) tracks become increasingly popular around the world, including the seismically active regions. In addition to the ARS limits to be imposed in the presence of seismic loading, there is also a lack of consensus regarding the proper combination of other load effects with earthquake loads. In order to establish standardized earthquake loads and ARS limits, a deeper understanding of the impact of seismic loading on the behavior of track-bridge interaction is necessary. However, due to the complex nature of earthquakes, accurate representation of seismic loading is relatively more complicated than defining the temperature or other mechanical loading effects. Additionally, the combination of load effects may vary depending on the specific type of railway service. For instance, designers may need to consider thermal, train, and service earthquake loads for urban railway bridges due to the high frequency of passing trains. On the other hand, bridges on major railway lines may primarily require the combination of only thermal and service earthquake loads.

The influence of various parameters on track-bridge interaction, including service earthquake intensity measure, soil property, distance to fault, and deck expansion joint locations, calls for extensive investigation in order to gain insights into their effects. Among the notable research in this field, Hu et al. (2022) proposed a classification of damage grade based on lateral displacement and train velocity, which can be directly applied in seismic vulnerability analysis. In another study, Hu et al. (2022) investigated an optimal intensity measure consisting of spectral acceleration and mass participation for high-speed railway bridges. Denghani et al. (2019) conducted a comprehensive finite element analysis of a concrete bridge. The study included pushover analyses to assess the strength and elastic behavior, followed by incremental dynamic analyses to investigate the load and structural capacity uncertainties. Their results demonstrate the benefits of incorporating track-bridge interaction in earthquake analysis and shed light on why railways tend to exhibit favorable performance during seismic events. Kim et al. (2013) examined the dynamic response of steel monorail bridges subjected to strong earthquakes, considering the train loading as an additional mass and a dynamic system. It was concluded that modeling the train as an additional mass overestimated the seismic performance of the monorail bridge. Davis (2009) conducted a parametric study on multi-pier ballasted track viaducts of a high speed railway by employing nonlinear time history analyses (NTHA) and reported that NTHA resulted in smaller relative displacements than response spectrum analysis. The author also highlighted the importance of the accurate modeling of foundation stiffness and the nonlinear interface between the track and the bridge structure. Petrangeli and Tortolini (2007) conducted a case study in order to assess the earthquake effects on railway bridges using nonlinear finite element analyses. The authors investigated the impact of substructure stiffness and the presence of rails on bridge displacements under seismic actions. Their findings revealed that both factors had a substantial influence on bridge displacements.

The majority of the numerical studies on TBI investigation with seismic loading have primarily focused on the behavior and damage assessment of bridge elements, rather than the track itself. Moreover, only a limited number of these studies have explored the TBI response through numerical simulations for specific design cases. The present study aims to advance the understanding of TBI response in railway bridges subjected to earthquakes and provide insights into numerical modeling based on a bridge type commonly used in Türkiye. The influence of various parameters, including soil conditions, distance to fault, earthquake magnitude, foundation stiffness, presence of expansion joints at pier locations, were systematically investigated to gain a comprehensive understanding of their impact on TBI. In addition, ARS results from loaded/unloaded conditions of RDCs were compared under a representative ground motion. The primary objective of the study is to assess the railway system's ability to remain operational in the case of frequent earthquakes from the perspective of TBI.

3.2 Methodology

The TBI investigation under earthquake ground motions was conducted for two existing railway bridges, designated as K8 and K9, located on the eastern part of Türkiye (i.e., on the Kars-Iğdır-Dilucu Railway line). Geometric details of the bridges are shown in Figure 3.1. Both bridges are straight in plan and have no skew. The structural system of the bridges is of simply supported precast prestressed concrete girder type. The K8 bridge has two 31.4 m side spans, and a 32.8 m middle span, while the K9 bridge has two 31.4 m spans. For the K9 bridge the girder ends are restrained in both the longitudinal and transverse directions at the pier location while no restraint is provided at the abutments. The K8 Bridge exhibits different girder end restraints depending on the pier axis. At one of the piers, the girder ends are restrained. At the other pier, no restraint is provided for one girder, while the girders of the neighboring span are restrained in both the longitudinal and transverse directions. No girder end restraint is present at the abutments. The bridge piers are formed by reinforced concrete columns with a 3.0x5.0 m rectangular cross-section. The K8 bridge has pier heights of 7.42 and 6.92 m, while the pier height in the K9 bridge is 6.92 m. The abutments are formed by 1.6 m thick abutment walls and 1.2 m thick wing walls. The typical section shown in Figure 3.1(c) is common to both bridges. The section consists of 10 precast concrete girders with a height of 1.9 m, supporting a 0.25 m thick and 12.0 m wide cast-in-place reinforced concrete deck. The ballasted track supported by the bridge deck accommodates two train lanes.

3.2.1 TBI Modeling

Details of the bridge numerical model used for the TBI analysis are illustrated in Figure 3.2. Elements simulating the bridge deck and girders were located at the centroid of the composite section. These elements were connected to the nodes located at the top surface of the deck and to the nodes located at girder supports with rigid beam elements. Bridge piers, deck, and rails were modeled with linear elastic beam elements. The element length for the rail and bridge deck was maintained at 1.0 m along bridge spans and reduced to 0.138 m in regions near the expansion joints or bridge ends, where there is a relatively steep gradient in stress and relative displacements. The expansion joints were incorporated in the bridge numerical model by reducing the axial stiffness of the deck between the girders to a fraction of the actual value. In the transverse and vertical directions, the rail elements were connected to the bridge superstructure through linear elastic springs possessing a relatively high stiffness. Spring stiffness in the vertical and transverse directions was taken to be 106 times the stiffness in the longitudinal direction based on the approach previously used by Pertangeli and Tortolini (2008) and Lie et al. (2021).

The main difference between the numerical models utilized in TBI analysis with and without seismic action lies in the modeling of RDCs. For thermal and train loads, the RDCs were represented as bilinear spring elements. However, in order to consider the nonlinear hysteretic behavior of the bridge model under seismic ground motion, these spring elements were replaced with general link elements with hysteretic capability. For this purpose, the element library available in Midas Civil (2012) was utilized. In the analyses, unloaded RDCs specified in UIC 774-3R (2001) for ballasted tracks in good maintenance condition were utilized. The nonlinear hysteretic behavior was defined with the yielding exponent value of 2, the post-yield stiffness ratio of zero, and the Bouc-Wen hysteretic loop parameters of α=0.5 and β=0.5.

The investigated bridges are located in a region with Soil Class D according to NEHRP (2003), which is the equivalent of ground type C as per EN 1998-1 (2004). The foundation at the base of piers was modeled by following two approaches. In the first approach, the pier bases were fixed against all six degrees of freedom (DOFs), which is referred to as fixed boundary condition (BC) in the remaining part of this paper. As a second approach for modeling pier foundations, 6-DOF spring elements were utilized with the method proposed by Dobry and Gazetas' (1986) for spread footings. More details on this modeling method are provided in the following sections.

3.2.2 Time History Analysis Procedure

To analyze the TBI response of bridge models under different ground motion scenarios, Nonlinear Time History Analysis (NTHA) approach was employed. The target design spectrum chosen for these analyses represents a service level earthquake with a return period of 72 years, as specified by the Turkish Earthquake Hazard Map. Therefore, the analysis results represented in this study is based on seismic activity corresponding to a service level earthquake. For NTHA, a direct implicit integration was used together with the Newmark method with constant acceleration for time integration. To account for damping, mass and stiffness proportional damping were implemented using a Rayleigh damping model. The modal damping parameters were defined based on the periods corresponding to the first two vibration modes (Chopra (1995)). Gravity loads were considered at the initial time step prior to NTHA. Gravity loading consisted of the self-weight of bridge components, including handrails (1.5 kN/m), protection concrete (10 kN/m), ballast and sleepers (115 kN/m), precast concrete side panels (1.9 kN/m), seismic blocks (70 kN), bearing pedestals (1.2 kN at abutments and 5.0 kN at piers), and diaphragm beams (60 kN/m). Each ground motion record was incorporated into the TBI model as scaled acceleration records consisting of two horizontal components. Each ground motion pair was employed in both the longitudinal and transverse directions of the bridge. The ground motion directions were denoted as XH1_YH2 and XH2_YH1 pairs. The XH1_YH2, for example, denotes the pair where the first component of the ground motion was applied in the longitudinal direction of the bridge, while the second component was applied in the transverse direction.

As mentioned earlier, both K8 and K9 bridges were originally designed and constructed with expansion joints at each abutment and pier locations. Both bridges are located on Class D type soil and were constructed with pile foundations underneath the piers. In order to study the effects of these construction details, the presence or absence of expansion joints at pier locations (i.e., intermediate expansion joints) and the type of boundary condition utilized at the base of piers were used as the analysis parameters (Table 3.1). The other parameter that was investigated in the study is the ground motion characteristics.

3.3 Ground Motion Record Selection and Scaling

Four primary sets of ground motions (GMs) with different earthquake magnitude, distance to fault, and soil type (Table 3.2) were chosen from the Pacific Earthquake Engineering Research Next Generation Attenuation West2 database (PEER, 2005) in order to investigate the effects of these parameters on the TBI response. The ground motions were selected as pulse-free and strike-slip type, due to the active faults in the vicinity of the investigated bridges exhibiting strike-slip characteristics. Each ground motion set comprised seven earthquake records, as specified by EN 1998-2 (2005). Only the horizontal ground motion components were considered in analyses, due to the fact that vertical ground motion has negligible impact on longitudinal TBI response in terms of bridge/rail relative displacements and ARSs.

GM Set-1 includes earthquakes with magnitudes ranging from Mw=6.5 to 7.5, corresponding to NEHRP Soil Class D, and distance to fault between 40 and 60 km. GM Set-2 consisted of earthquakes with magnitudes ranging from Mw=4.5 to 5.5, also associated with NEHRP Soil Class D, and distance to fault between 15 and 25 km. GM Set-3 and Set-4 are identical to Set-1 and Set-2, respectively, in terms of distance to fault and magnitudes, except that the records were selected for NEHRP Soil Class C.

EN 1998-2 (2005) specifies an amplitude scaling method based on bounding the spectrum between the periods of 0.2*Tp* and 1.5*Tp*, where *Tp* represents the period corresponding to the first vibration mode of the bridge. The arithmetic mean of the square root of the sum of the squares (SRSS) spectra representing the seven pairs of GM records is expected to remain above the target spectrum, which is 1.3 times the design spectrum. For the K8 and K9 bridges, the first vibration mode is in the longitudinal direction with a period of *Tp*=0.34 s. Therefore, scaling of the GMs was conducted by considering the target spectrum between the periods of 0.068 and 0.51 s. The unscaled and scaled spectra for the four GM sets utilized in the analyses are shown, respectively in Figures 3.3 and 3.4, with the corresponding scale factors provided in Table 3.3. As evident in the insets in plots provided in Figure 3.4, the scale factors were mostly dictated by the lower boundary (0.2*Tp*) for GM Set-1 and Set-2, and by the upper boundary (1.5*Tp*) for GM Set-3 and Set-4.

3.4 Analysis Results

3.4.1 Influence of Ground Motion Parameters

The impact of earthquake magnitude and distance to fault is investigated by comparing the TBI responses under GM sets with a higher magnitude and a longer distance to fault (Mw=6.5-7.5, 40-60 km distance) (i.e., GM Set-1 and Set-3) and a lower magnitude and a shorter distance to fault (Mw=4.5-5.5, 15-25 km distance) (i.e., GM Set-2 and Set-4). ARS due to seismic ground motions is significantly affected by the value of the spectral acceleration corresponding to the first vibration mode of bridge models. The mean spectral acceleration at the first vibration mode of bridge models in the longitudinal direction (i.e., Tp=0.34 s) is 0.67g, 0.46g, 0.55g and 0.57g, respectively for GM Set-1, Set-2, Set-3 and Set-4.

Variation of ARSs under four GM sets is presented in Figure 3.5. It should be noted that these rail stresses are those due to GM and self-weight of bridge components only and do not include the effects of thermal and train loadings. In the figure, the maximum tensile (positive) and compressive (negative) rail stresses obtained from time history analyses are plotted along the rail. For each analysis two plots are provided, one showing the maximum tensile stresses and the other one showing the maximum compressive stresses. These plotted stresses represent the average of the maximum rail stresses from the seven GM records in each GM set. It should be noted that the results shown in Figure 3.5 were obtained from bridge models with fixed boundary conditions at pier bases and without intermediate expansion joints. For all cases studied, maximum rail stresses occur at abutment locations. For ground motions recorded at NEHRP soil class D (i.e., GM Set-3 and Set-4), a change in earthquake magnitude and distance to fault does not result in a clear trend in the change of maximum ARS. Part of the reason for such a behavior is the fact that the mean spectral acceleration at the first vibration mode of bridge models is close to each other for these two GM sets. For ground motions recorded at NEHRP soil class C (i.e., GM Set-1 and Set-2), on the other hand, the GM set with a higher earthquake magnitude and a longer distance to fault results in 25% larger tensile ARS and 33% larger compressive ARS than the GM set with a lower earthquake magnitude and a shorter distance to fault. This is an indication that even though the same target spectrum is used for scaling GM records, there may be significant variation in rail stresses produced by different GM sets. Therefore, selection of proper GM records is of critical importance when conducting TBI analysis.

3.4.2 Influence of Expansion Joints

In railway bridges, the use of expansion joints is highly common, especially in simply supported multi-span bridges. Indeed both bridges studied in the current investigation were constructed with expansion joints at all abutment and pier locations. However, there are some cases in bridge design practice, where expansion joints are omitted at certain girder ends mainly in an attempt to avoid the cost associated with the installation and maintenance of expansion joint devices. Additional analyses were conducted as part of the present study to investigate the difference in TBI response with the presence and absence of expansion joints at pier locations. It is worth noting that for both of these cases, expansion joints were present at abutment locations. Figure 3.6 provides a summary of ARSs with and without intermediate expansion joints at pier locations under various GM sets. As evident in the plots, the magnitudes of ARSs change significantly depending on whether or not there are expansion joints at pier locations. For all of the studied cases, a consistent trend is evident: the inclusion of expansion joints at pier locations leads to a reduction in the maximum tensile rail stresses and an increase in the maximum compressive rail stresses at abutment locations. Another observation that is valid in the plots provided in Figure 3.6 is that for the two-span K9 bridge additional tensile rail stresses develop at the pier location with the inclusion of expansion joint at this location. As a matter of fact, for some of the analyzed cases the maximum tensile rail stresses at the pier location with intermediate expansion joint get larger than the maximum tensile rail stresses at the abutments. The reduction in the maximum tensile rail stresses varies between 10% and 33%, while the increase in the maximum compressive rail stresses is between 14% and 37%. It is noteworthy that among all cases considered, Analysis 1c/1d (i.e., Bridge K8 analyzed under GM Set-1) results in the largest percent reduction in the maximum tensile rail stress and the smallest percent increase in the maximum compressive rail stress.

3.4.3 Influence of Pier Support Modeling

The original designs of both K8 and K9 bridges include pile foundation for piers, as illustrated in Figure 3.1. In the numerical model used for the analyses the interaction between the piles and the surrounding soil was neglected and fixed boundary condition idealization was used at pier bases. Similar modeling approach has previously been adopted in earlier studies and based on guidelines (Dicleli et al. (2005), Aviram et al. (2008), Turkish Seismic Bridge Design Code (2020)). In order to examine the effect of soil stiffness on the behavior of the bridges, the analyses were repeated with spread footing foundation for piers. The method proposed by Dorby and Gazetas (1986) was employed to model the spread footing foundation. This method utilizes empirical equations to determine the equivalent dynamic stiffness properties corresponding to all six degrees of freedom based on the shape of the footing as well as the shear modulus and Poisson's ratio of the soil beneath the footing. The initial shear modulus of the soil was taken as G_{max}=207,000 kPa based on the typical values provided by the Federal Highway Administration (1997). This value was then multiplied with the reduction factor of λ_G=0.865 (Turkish Seismic Bridge Design Code, 2020) to determine the effective shear modulus. The spring stiffness values corresponding to all six degrees of freedom determined according to the method proposed by Dorby and Gazetas (1986) are presented in Table 3.4 for both K8 and K9 bridges. These stiffness values were assigned to the spring elements used at the base of piers in bridge numerical models.

Rail stress distributions with the fixed BC idealization and soil springs utilizing the stiffnesses explained above are presented in Figure 3.7. As evident in the plots, for all cases considered there is no appreciable difference between the rail stress responses with the two support modeling approaches. The largest change in the maximum tensile rail stress is 11% in Analysis-1d, while the largest change in the maximum compressive rail stress is 9% in Analysis-1c. These observations indicate that for the studied bridges and soil types, using idealized fixed support at pier bases provides sufficiently accurate rail stresses when compared to modeling the supports with soil springs utilizing the appropriate stiffnesses. It should be noted that this conclusion holds only for the soil shear modulus level used in the analyses. With a lower soil shear modulus value, one can anticipate a more significant variation in the rail stress values between the two pier support modeling approaches.

3.4.4 Influence of Utilizing Unloaded and Loaded RDCs

The analyses explained in previous sections were conducted with RDCs representing the unloaded condition of the track, due to the fact that no train was assumed to be present over the bridge during the earthquake. However, one viable loading scenario, especially for design of urban railway bridges, is the occurrence of a service-level earthquake with a train located over the bridge. In this scenario, the RDCs corresponding to the loaded condition of the track should be used for TBI analysis. In order to investigate how sensitive the TBI response is to the use of unloaded versus loaded RDC, additional analyses were conducted under the scaled ground motion record from Station RSN 1636 (Manjil, Iran). The numerical model of K9 bridge without intermediate expansion joints was utilized in these analyses.

The unloaded and loaded RDCs used in the analyses are shown in Figure 3.8(a). These are the RDCs provided by UIC 774-3R (2001) for ballasted tracks. The ARS distributions along the length of the bridge with both of these two RDCs are plotted in Figure 8(b). As evident in the plots, with loaded RDC 2.2 times higher tensile stress and 2.10 times higher compressive stress develop in rails due to the ground motion. Another observation that is valid in these plots is that the type of RDC had no appreciable effect on the distribution of rail stresses along the track. Figure 3.8(c) displays a comparison of the hysteretic force-displacement response of rail-deck interface elements with unloaded and loaded RDCs under the ground motion record from Station RSN 1636. These hysteretic force-displacement responses were obtained from rail-deck interface elements located at the left roller support location of the bridge, where the element length is 138 mm. For both RDCs the yield limit of 2 mm was exceeded during the ground motion, indicating nonlinear behavior. The results indicate that the maximum relative displacement between the deck and rail is 9.72 mm and 6.85 mm, respectively with the unloaded and loaded RDCs. It should be noted that these rail/deck relative displacements are significantly larger than the 4 mm limit defined in UIC 774-3R (2001) under braking/acceleration forces. Unfortunately, no displacement limit is provided in UIC 774-3R provisions under seismic loading. Nevertheless, the Taiwan High-Speed Railway Provision (2000) provides a relatively large value of 25 mm as the rail/deck relative displacement when the service earthquake loading is combined with thermal and train loads. The relative displacements obtained in the present study remain below the limit provided by the Taiwan High-Speed Railway Provision (2000).

The rail stress and acceleration time histories obtained with unloaded and loaded RDCs are presented in Figure 3.9. The ground motion acceleration plot exhibits short-duration peaks for a duration of 1.5 seconds between t=15.5-17.0 s, while the rail stress and rail acceleration peak duration extends to approximately 3 seconds. This behavior may be attributed to the yielding of RDCs and the subsequent redistribution of stresses within the rail. The plots in Figure 3.9 also reveal that rail stresses are affected by the type of RDC more than rail accelerations.

Table 3.1 Analysis Parameters

Analysis #	Ground Motion Set	Expansion Joint at Pier	Bridge
1a	Set-1	No	(K9)
1b	Set-1	Yes	(K9)
1c	Set-1	No	(K8)
1d	Set-1	Yes	(K8)
2a	Set-2	No	(K9)
2b	Set-2	Yes	(K9)
3a	Set-3	No	(K9)
3b	Set-3	Yes	(K9)
4a	Set-4	No	(K9)
4b	Set-4	Yes	(K9)

Table 3.2 Properties of the GM sets used in analyses

Ground Motion Set	Magnitude Mw	Distance to Fault (km)	NEHRP Soil Class
Set-1	6.5-7.5	40-60	D
Set-2	4.5-5.5	15-25	D
Set-3	6.5-7.5	40-60	C
Set-4	4.5-5.5	15-25	C

Table 3.3 Scale factors used for the selected GMs

GM Set-1							
RSN	36	166	862	1144	1636	3890	8522
Name	Borrego Mtn	Imperial Valley-06	Landers	Gulf of Aqaba	Manjil Iran	Tottori Japan	Cucapah Mexico
Year	1968	1979	1992	1995	1990	2000	2010
Scale Factor	2.00	2.00	2.00	2.10	1.10	1.10	1.00
GM Set-2							
RSN	18	200	229	2024	8622	11502	18166
Name	Imperial Valley-04	Imperial Valley-07	Anza-01	Gilroy	40204628	10275733	14519780
Year	1953	1979	1980	2007	2007	2007	2009
Scale Factor	3.00	2.00	3.00	3.00	3.50	3.00	3.00
GM Set-3							
RSN	897	1620	1627	3922	4054	5842	6949
Name	Landers	Duzce Turkey	Caldiran Turkey	Tottori Japan	Bam Iran	Cucapah Mexico	Darfield New Zealand
Year	1992	1999	1976	2000	2003	2010	2010
Scale Factor	2.80	3.00	2.80	3.00	2.85	3.00	2.85
GM Set-4							
RSN	224	8742	9048	9478	11333	11364	18010
Name	Livermore-02	40204628	14151344	10410337	9064093	10275733	14517500
Year	1980	2007	2005	2009	1998	2007	2009
Scale Factor	6.30	6.30	6.30	6.30	6.30	6.30	6.30

Table 3.4 Spring stiffness values used for spread footing at pier bases

Bridge	K_x (kN/m)	K_y (kN/m)	K_z (kN/m)	$K_{\theta x}$ (kNm/rad)	$K_{\theta y}$ (kNm/rad)	$K_{\theta z}$ (kNm/rad)
K8	7.25×10^6	7.25×10^6	4.07×10^6	450×10^6	450×10^6	599×10^6
K9	7.91×10^6	7.77×10^6	4.47×10^6	678×10^6	516×10^6	797×10^6

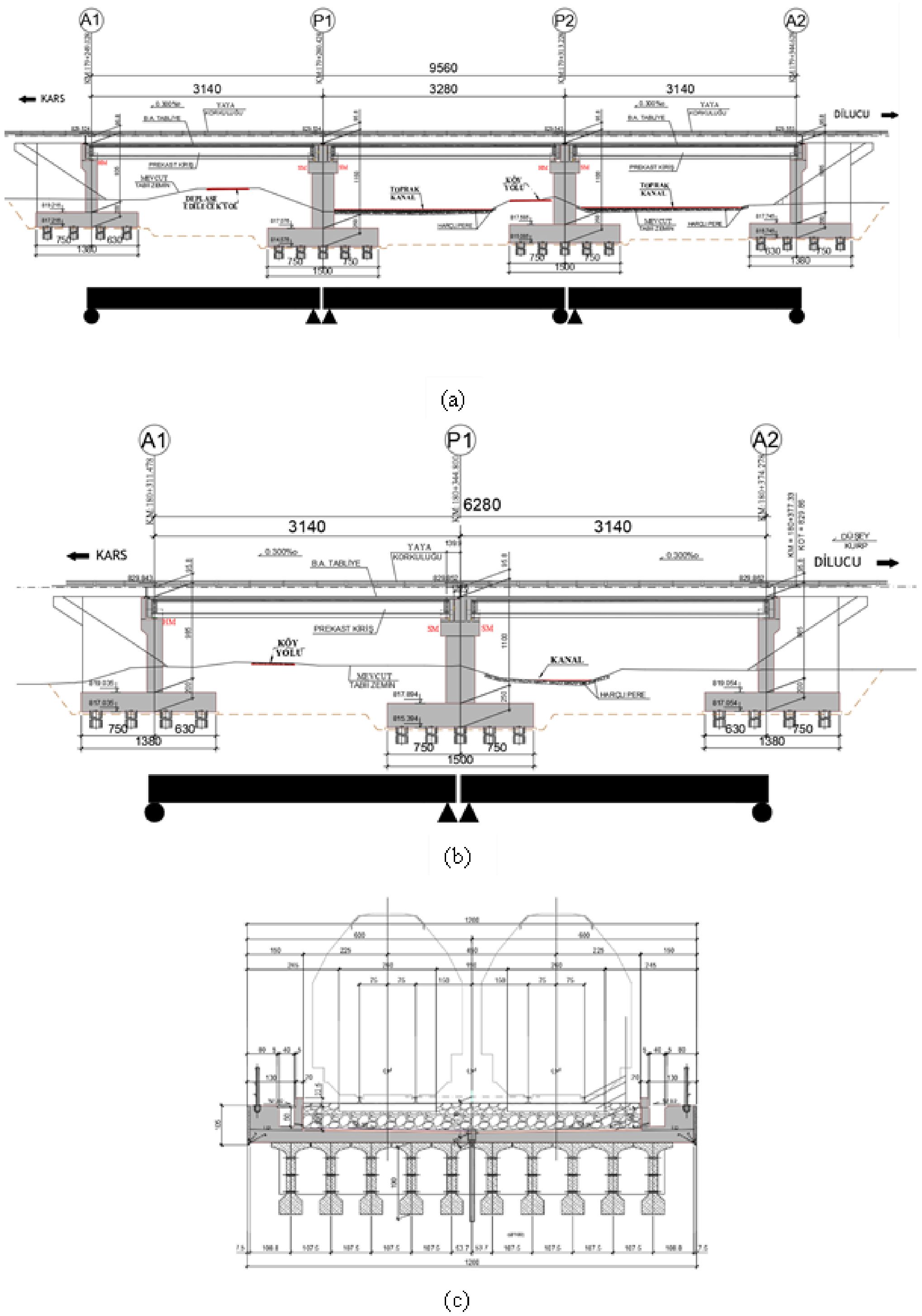

Figure 3.1. Geometric details of the investigated bridges: (a) details of K8 bridge; (b) details of K9 bridge; (c) section view of precast prestressed girders for both bridges

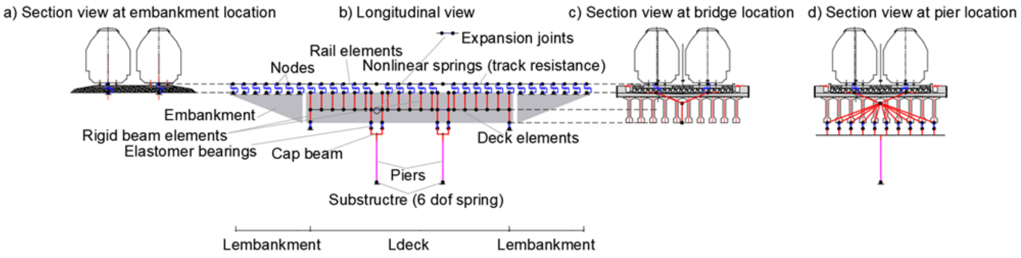

Figure 3.2. Modeling details used for bridges

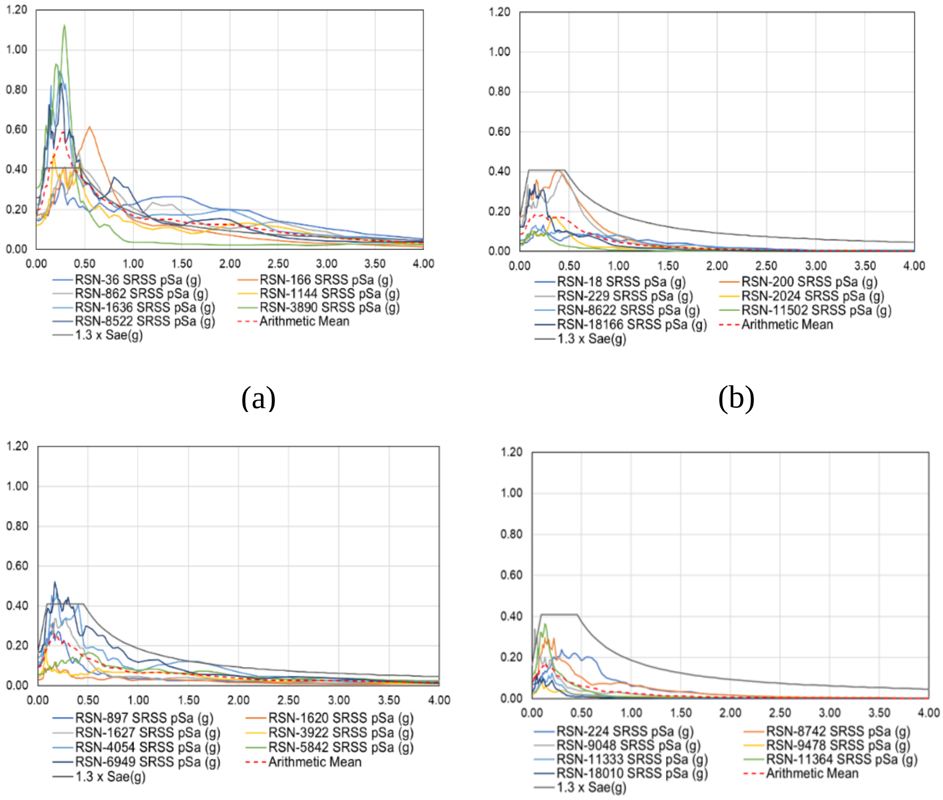

(a) (b)

(c) (d)

Figure 3.3. Unscaled ground motion spectra and target spectrum for: (a) GM Set 1; (b) GM Set 2; (c) GM Set 3; (d) GM Set 4

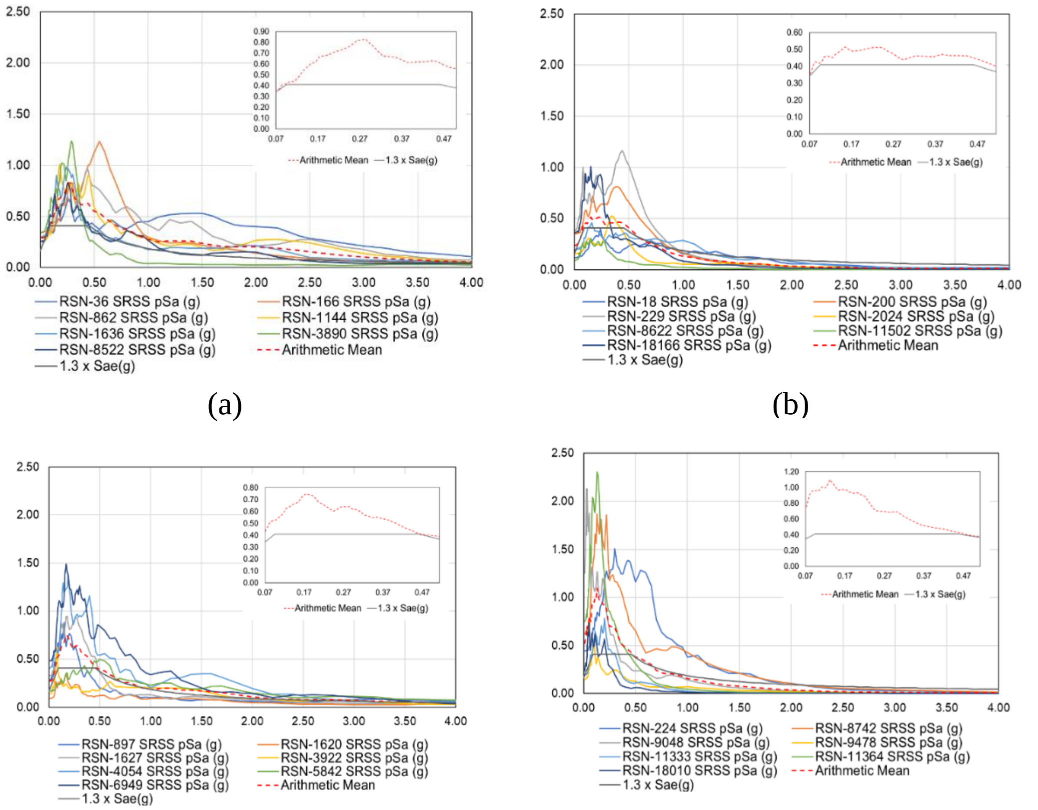

(a) (b)

(c) (d)

Figure 3.4. Scaled ground motion acceleration spectra and target spectrum for: (a) GM Set-1; (b) GM Set-2; (c) GM Set-3; (d) GM Set-4

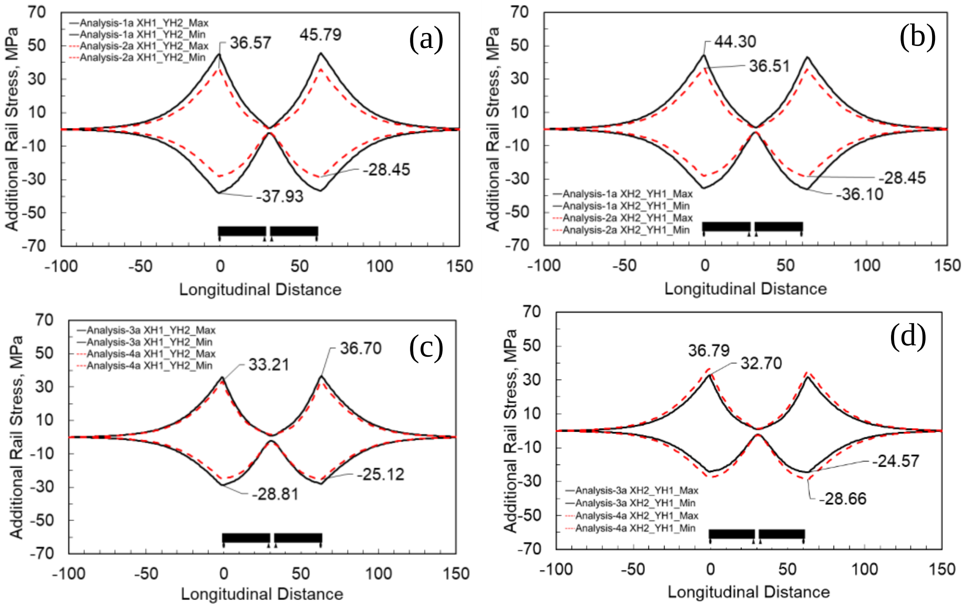

Figure 3.5. Variation of ARSs due to GM in Bridge K9: (a) Analysis 1a/2a XH1_YH2 direction; (b) Analysis 1a/2a XH2_YH1 direction; (c) Analysis 3a/4a XH1_YH2 direction; (d) Analysis 3a/4a XH2_YH1 direction

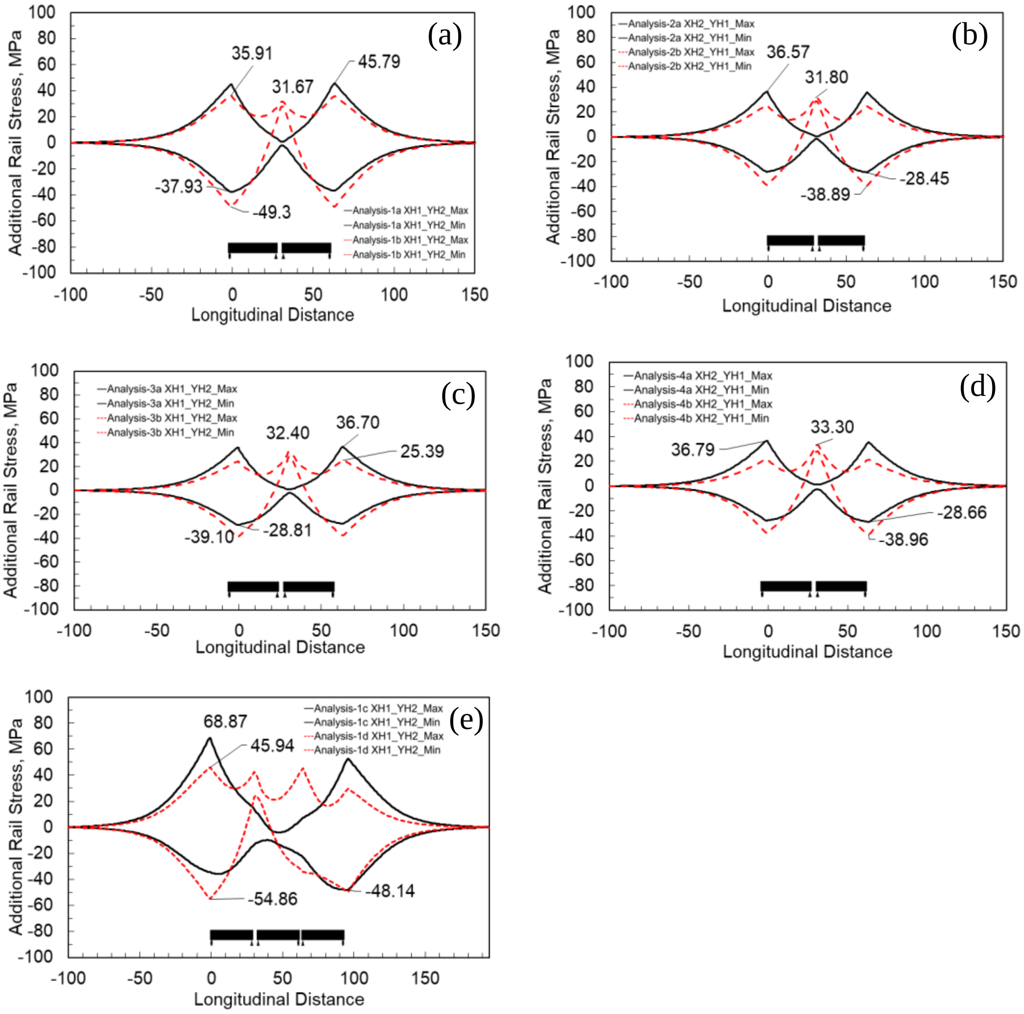

Figure 3.6. Effect of the presence of intermediate expansion joints on ARSs: (a) Analysis 1a/1b; (b) Analysis 2a/2b; (c) Analysis 3a/3b; (d) Analysis 4a/4b; (e) Analysis 1c/1d

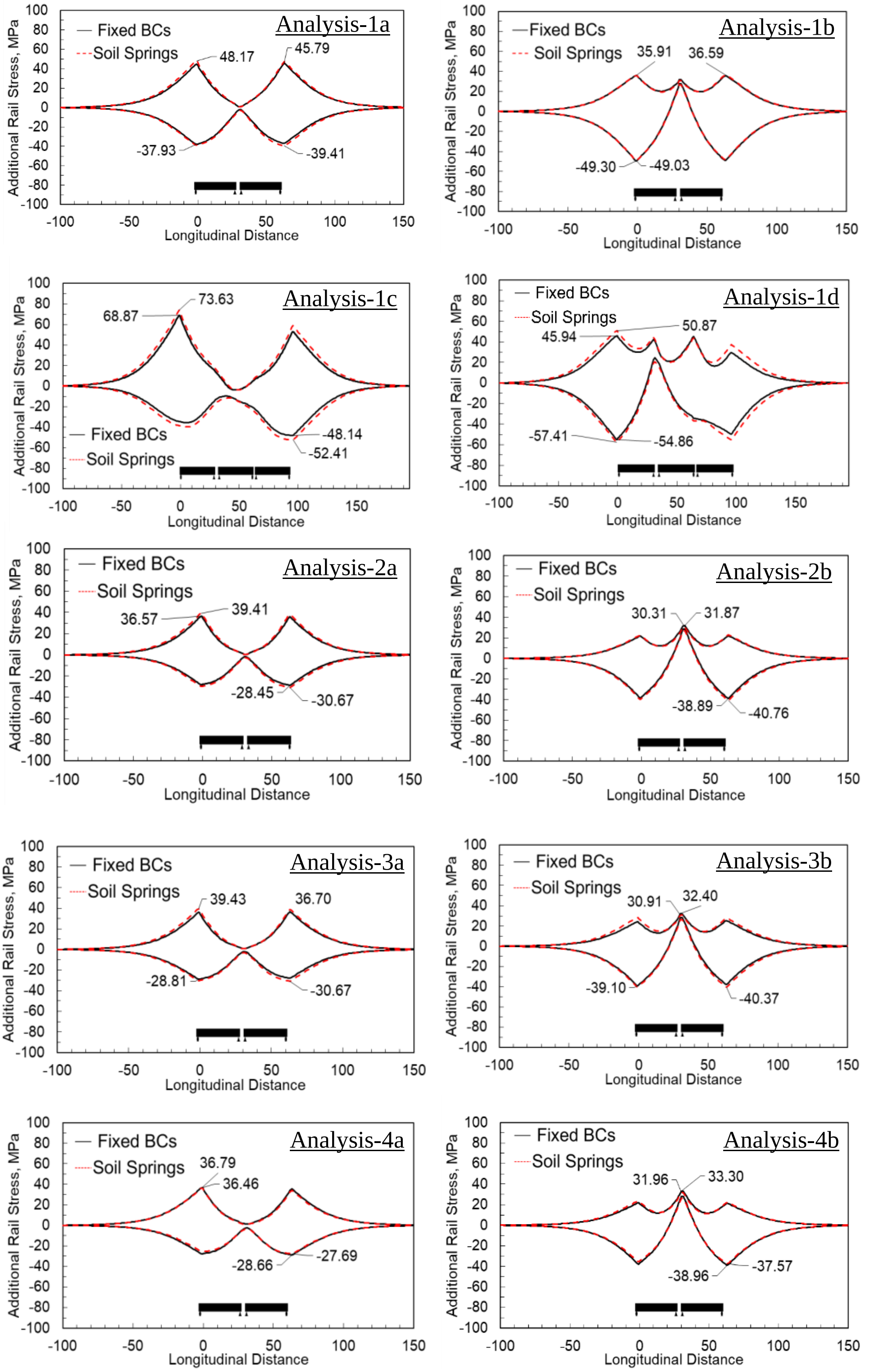

Figure 3.7. Effect of the pier supports in ARSs due to GM

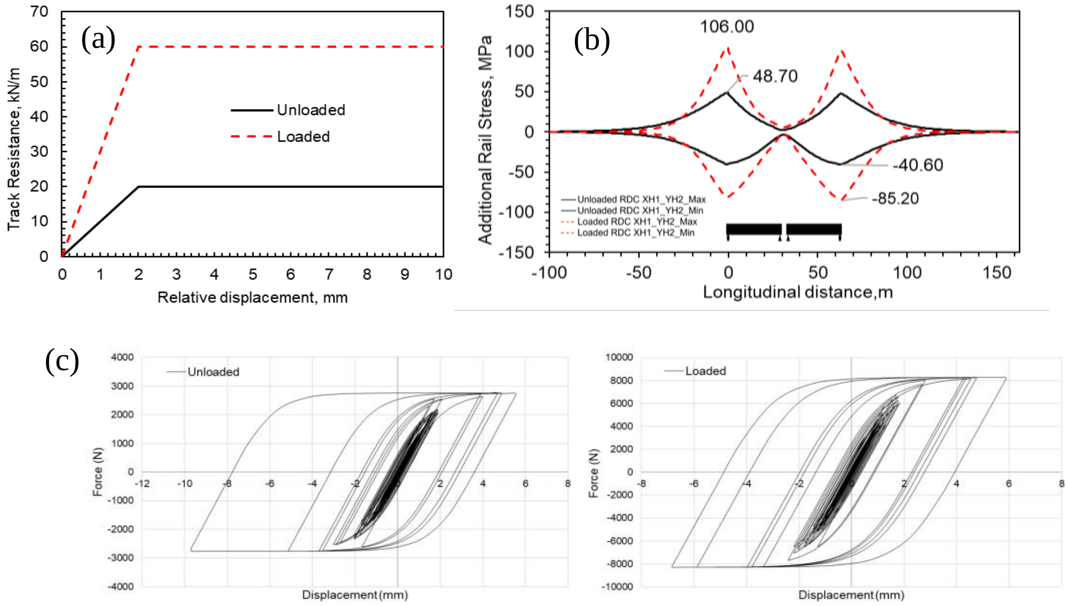

Figure 3.8. Influence of the type of RDC in Bridge K9 under GM RSN 1636: (a) unloaded and loaded RDCs used in analyses; (b) ARSs with unloaded and loaded RDCs; (c) force-displacement response of interface elements at the left roller support location

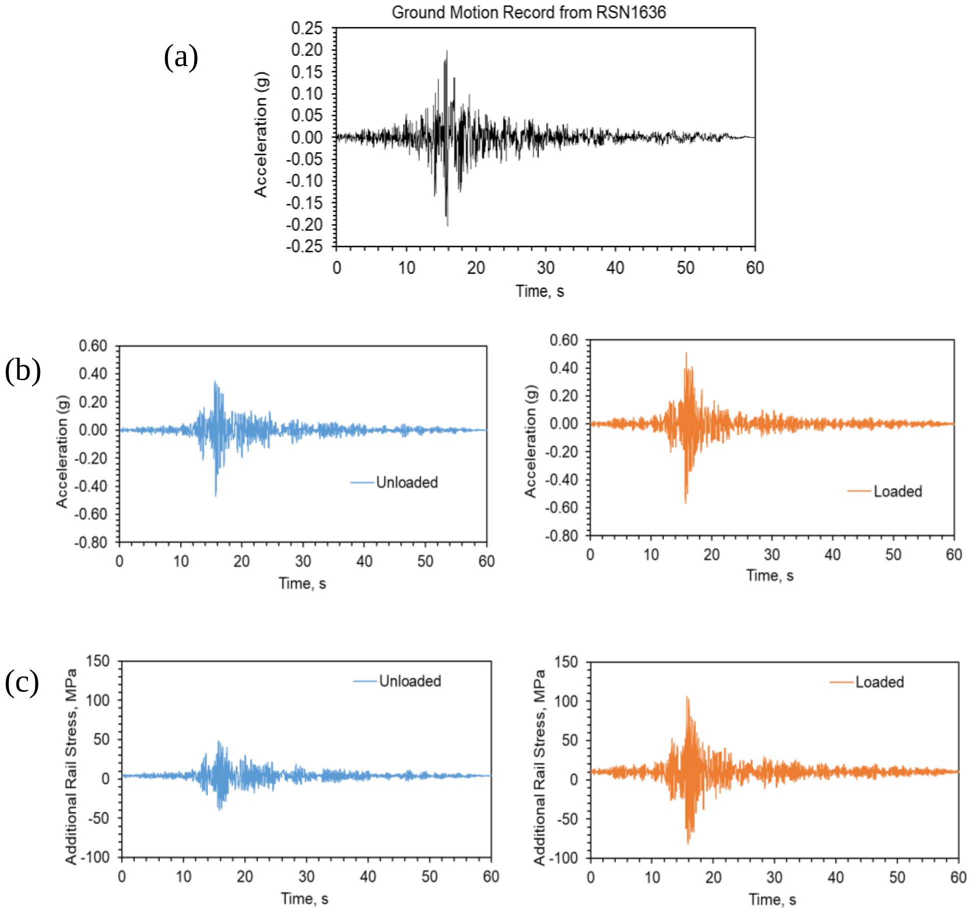

Figure 3.9. Ground motion record and time history response at the left roller support location in Bridge K9: (a) ground motion record from RSN1636; (b) acceleration response with unloaded and loaded RDCs; (c) ARSs with unloaded and loaded RDCs

CHAPTER 4

TRACK BRIDGE INTERACTION BEHAVIOR OF RAILWAY BRIDGE SUBJECTED TO PAZARCIK-ELBİSTAN EARTHQUAKES

Unfortunately, on February 6, 2023, at 04:17 local time (01:17 GMT), a strong earthquake of moment magnitude Mw=7.7 occurred on the East Anatolian Fault, as reported by the Disaster and Emergency Management Presidency (AFAD, www.afad.gov.tr). The epicenter of this seismic event was located in Pazarcık-Kahramanmaraş. Roughly 9 hours later, at 13:24 (10:24 GMT), another substantial earthquake with a moment magnitude Mw=7.6 struck Elbistan-Kahramanmaraş. After these two significant earthquakes, over 10,000 aftershocks were recorded.

This chapter focuses on a series of numerical analyses to investigate TBI behavior further, based on the earthquake records of these two devastating events, along with selected aftershocks ranging from Mw=5.5 to Mw=6.6. Only the records falling within the timeframe of February 6 to April 1, 2023, were included to align with the predetermined time limit for the PhD study.

This chapter of the study differs from the preceding chapter in two key aspects, apart from the ground motion records used in the analyses. The first divergence involves the methodology used for scaling in the analyses. The second significant difference lies in the direct utilization of ground motion records associated with recent earthquakes, without any scaling process. Further details regarding both aspects are elaborated in the following sections.

4.1 Numerical Modeling

The numerical model of the K9 bridge explained in Chapter 3 was utilized for the analyses explained in this chapter. The details for the bridge are given in Figures 3.1(b) and 3.1(c). A two-span simply supported superstructure, the K9 bridge features girder pin supports at pier locations, and girder roller supports at abutment locations. It was originally designed with pile foundation underneath the pier, leading to the presumption that the node at the base of the pier was rigidly fixed in all six degrees of freedom. The modeling approach as well as the time history procedure mirrors the one used in Analysis 1b from the previous chapter. A general link element with hysteretic behavior was employed. The TBI link element aligns with the UIC 774-3R (2001) unloaded RDC, which represents the ballasted track system used in the K9 Bridge. The reasoning behind using UIC recommended ballasted RDC is because there has been comparatively less exploration of ballasted track resistance although several studies (Zhang et al. (2015), Yang and Jang (2016), Zeng et al. (2019)) evaluated fastener resistance in ballastless slabs (i.e., track slabs). Even though Yun et al. (2019) conducted a study on ballasted tracks to measure RDCs, yet these findings were not applied in the numerical models due to their divergence from UIC standards in lower initial stiffness and higher yield capacity, potentially not accurately representing the actual conditions of the K9 bridge.

Acknowledging that the goal is to gain insights of TBI behavior rather than conduct a seismic assessment of the bridge, certain nonlinear properties related to piers, bearings, and soil-structure interaction (SSI) for backfill of the abutments were not considered. For embankment locations, including the backfill material behind the abutment, the modeling assumed uniform lateral and vertical stiffness across the entire length of the embankment. For this study, the Turkish Seismic Bridge Design Code (2020) guidelines were utilized to ascertain the effective stiffness properties specific to the superstructure elements. Turkish Seismic Bridge Design Code (2020) advocates for an effective stiffness in flexure and shear set at 50% of gross stiffness, while no reduction is recommended for axial behavior for superstructure of the bridge. Effective torsional and flexural stiffnesses of T-shape cap beams and pier columns were taken respectively as 20% and 50% of the corresponding gross stiffnesses. Additionally, for the elastomeric bearings present to girder supports, a lateral stiffness of 5818 kN/m in each direction was utilized, as described by Equation (4.1). Notably, the shear modulus of the elastomeric bearing, G was taken as 931 kN/m² as per given in K9 bridge design report (2020), while the plan area of the elastomer is A_{bp} is 0.2 m² and the thickness of the elastomeric bearing h_{pb} is 32 mm. It should be noted that the stiffness of bearings may change due to temperature change and aging, but in the analyses nominal stiffness was considered.

$$k_h = \frac{GA_{bp}}{h_{bp}} \tag{4.1}$$

4.2 Ground Motion Scaling Methodology

4.2.1 Selecting of Ground Motions

TBI design primarily targets assessing the safety of tracks during seismic events, ensuring their stability in such circumstances. A comprehensive data set comprising 180 ground motion records (i.e., 12 events and 15 records for each event) were compiled from various recording stations accessed through tadas.afad.gov.tr.

Table 4.1 details the classification of stations based on their distance from the epicenter for each event used in the analyses. More details regarding the distribution of the ground motion records are presented in Annex C. Originally, the aim was to obtain ground motion data uniformly across distance intervals, intending to secure three records for each interval and thus totaling 15 ground motion records (i.e., five distance intervals and three records for each event). Given the limited number of available stations near the epicenter, gathering additional ground motion records from shorter distances was prioritized. This approach aimed to compensate for the shortage of stations within the 0-15 km and 15-30 km intervals with the data provided by Disaster and Emergency Management Presidency. Table 4.2 represents the distribution of the total of 12 earthquake events and 180 ground motion recordings based on their magnitudes. Eventually, 75% of the earthquake records used in the analysis are between Mw/ML = 5.5-6.0.

In the previous chapter, amplitude scaling was conducted according to EN 1998-2 (2005). This scaling method was based on the arithmetic mean of seven records, which were found to be below 1.3 times the target spectrum within the specified period range of $0.2Tp$ and $1.5Tp$. The method has a drawback related with the scale factors mostly being dictated either by the lower ($0.2Tp$) or the upper boundary ($1.5Tp$), as depicted in Figure 3.4. In this part of the study, the scaling of the ground motion records specifically targeted the first longitudinal mode vibration period of the K9 bridge, Tp = 0.34 seconds, by multiplying the ground motion spectrum to fit the target spectrum at this period. It should be mentioned that the target spectrum was the one provided by the Turkish Seismic Bridge Design Code (2020) for a service level earthquake with a return period of 72 years. The scaling procedure notably omitted the utilization of standard multipliers, such as 0.9 for ASCE 7-16 (2016), ASCE 41-17 (2017) or 1.3 for EN 1998-2 (2005).

Figure 4.1 and Figure 4.2 depict the unscaled and scaled ground motion spectra for the Pazarcık Kahramanmaraş Mw=7.7 event respectively, demonstrating how each spectrum was anchored to the first longitudinal period. The mean spectral acceleration at the first vibration mode of bridge models in the longitudinal direction is the same, which is 0.32g, for all the records. As evident in Figure 4.2, the spectral accelerations change rapidly in the vicinity of the first longitudinal mode vibration period for some records. This indicates any change in the vibration period of the bridge due to a reduction in the stiffness will result in a marked effect on the response. Hence, this adjustment will eventually be expected to appear as variations in maximum ARSs. The unscaled and scaled spectrum for the rest of the events are provided in Appendix B, as the core concept remains consistent throughout different ground motion spectra.

The scale factors used for all ground motion records are provided in Table 4.3. The scatter valid in the scaling factors is due to significant variation of the records in terms of the spectral acceleration values at first vibration period of the K9 Bridge.

4.3 Analysis Results

ARS distribution 15 ground motion pairs are given in Figures 4.3 to 4.14. It should be noted that these stresses are those resulting from ground motions only, with no other loading. Four different plots represent the maximum compressive and tensile ARS distributions through the longitudinal distance. Each ground motion pair was employed in both the longitudinal and transverse directions of the bridge which is denoted as XH1_YH2 and XH2_YH1 as explained in the previous chapter. Each plot includes 15 curves (i.e., for 15 ground motion records) and each analysis pair is plotted in gray lines, to illustrate the range of ARS results. During the analysis, the "yielding" of the RDC links decreased the overall system stiffness, which in turn resulted in a change in the vibration period. Consequently, rail forces were increased or decreased depending on the variation of the spectral accelerations, as depicted in the inset of Figure 4.2 and Appendix B. This explains the main reason why the TBI response under different ground motion records differed even though they were scaled to the same acceleration spectrum at the first mode vibration period of the bridge. This behavior is similar to the one explained in the previous chapter even though the scaling method was different. Another noteworthy finding is related with the maximum tensile and compressive ARSs obtained from the analyses from different events, given in Table 4.4. As evident, there is not a major difference in the maximum ARS values obtained from events with significant difference in magnitude. Even though this behavior can be attributed to the fact that all ground motion records were scaled to the same target spectrum, this is not the main reason. The main reason for all investigated ground motions producing similar levels of ARSs is related with the 2 mm yielding capacity of the RDC used for the ballasted, unloaded RDCs. This issue is further elaborated in the subsequent section by utilizing TBI analyses with unscaled ground motion records.

4.4 Selecting of Unscaled Ground Motions

This section originates from a curiosity of how TBI behavior is influenced in the case of analysis with unscaled ground motions records. Special attention was devoted to the relation between the PGA and PGV values of the ground motions and the resulting ARSs and displacements. To accomplish this objective, PGA, PGV, and distance to rupture values were gathered from Annex A2 of the Preliminary Reconnaissance Report (2023) detailing the Pazarcık Kahramanmaraş (Mw = 7.7) and Elbistan Kahramanmaraş (Mw = 7.6) Earthquakes. These values were carefully selected to encompass a broad spectrum of possibilities for the study. The distribution of PGA and PGV values with respect to distance to epicenter and rupture are provided in Appendix C. In addition to the two earthquakes mentioned earlier, the Nurdağı Gaziantep Earthquake (Mw = 6.6), Yayladağ Hatay Earthquake (Mw = 6.4), and Yeşilyurt Malatya Earthquake (ML= 5.8) were also taken into account. Unfortunately, for these three events, specific distance to rupture data was not available. Instead, epicenter distances were utilized based on the information sourced from the website of the Disaster and Emergency Management Presidency. For each earthquake event five different station records were selected. Spectral accelerations for all five earthquakes are given in Figures 4.15 to 4.19. The response spectra, PGA, and PGV values exhibited variation across different events as well as within the same events across different stations. This variability was observed in both inter-event and intra-event analyses, highlighting diverse seismic behaviors across multiple locations and within individual seismic occurrences which is in line with the objective.

4.5 Analysis Results of Unscaled Ground Motions

4.5.1 Influence of Distance to Rupture on ARSs

For the five earthquakes mentioned above, the maximum compressive and tensile ARS results throughout the time history analyses are plotted in Figure 4.20 to Figure 4.24. In Figure 4.20 which represents the response to Pazarcık event, the maximum compressive and tensile stresses are 59.0 MPa and 45.3 MPa, respectively. For all five ground motions considered, the maximum rail stresses occur at the two ends of the bridge. Notably, the ARSs are observed to be close to each other for distances to rupture of 11.1, 14.4, 15.2 and 21.6 km. However, when the distance to rupture is 86.1 km, significantly smaller maximum compressive and tensile stresses of 30.2 MPa and 32.0 MPa, respectively were determined. These disparities in the ARSs are related to the effects associated with the proximity to the fault line. Even tough significantly larger ARSs were observed in events with relatively small distances to rupture, they are still below the stress limits given by the Taiwan Code (2000), as summarized in Table 4.5. The difference between the ARS limits with and without the earthquake effect yields a stress margin of 75 MPa according to the code. This margin could be considered as the recommended allowance for railway bridges subjected to a service level seismic event. A close examination of the ARS values indicates that when unloaded RDCs are used, slip occurs between the rail and the bridge structure once the 2 mm limit is exceeded. As a result, the significance of ARSs as a valuable design parameter diminishes, despite notably higher values with closer distances to rupture during the Pazarcık event.

The ARS distribution results for the Elbistan earthquake are illustrated in Figure 4.21, showcasing distances to rupture ranging from 22.7 to 73.7 kilometers. Interestingly, the maximum tensile stresses remained largely consistent across all cases, primarily attributed to gravity loads that were considered at the initial time step prior to NTHA, as addressed in previous chapter. However, the maximum compressive stresses exhibited a notable variation, ranging from 7.0 MPa to 37.8

MPa, corresponding to the results obtained from the largest and smallest distances to rupture, respectively. In the case of the Elbistan event, there seems to be a consistent relation between distance to rupture and the ARS results as expected.

ARS results for Nurdağı Mw=6.6 earthquake is provided in Figure 4.22. The maximum compressive ARS spans from 36.7 MPa to 62.1 MPa, while the maximum tensile ARS extends from 32.1 MPa to 48.7 MPa. In contrast to Pazarcık and Elbistan events, when spectral acceleration plots were considered for Nurdağı event, as provided in Figure 4.17, it becomes apparent that Station 2712 exhibits maximum ARS values, surpassing even Station 4616, despite the latter's proximity to the epicenter. This discrepancy can be predominantly attributed to the variations in spectral acceleration, PGA, and PGV values at these respective stations. The PGA and PGV values are in line with respect to distances to rupture, however it is not the case for epicenter distances. By comparing Figure 4.18 with Figure 4.23, and Figure 4.19 with Figure 4.24, similar conclusions can be reached regarding the ARS results for Yayladağ (Mw=6.4) and Yeşilyurt (ML=5.8) seismic events.

4.5.2 TBI Response in Terms of Displacements

The results for the maximum and minimum deck displacement are plotted in Figure 4.25 to Figure 4.29. Deck displacements along the bridge axis were retrieved from the centroid of the superstructure where beam elements were defined. As indicated in Table 4.5 a 25 mm limit is specified in the Taiwan Code (2000) for displacement of bridge deck. The purpose of such a displacement limit is to ensure stability during a seismic event. Considering that this limit also accounts for braking/acceleration forces and temperature effects, it leaves an 18 mm displacement margin for the seismic effects. Four out of the five analyses exceeds for the Pazarcık event (Mw=7.7) surpassed this limitation (Figure 4.25), which is intriguingly not the case for the Elbistan event (Mw=7.6) (Figure 4.26). Despite the similarity in high earthquake magnitudes, this contrast might be due to the larger distance to rupture of the chosen stations in Elbistan, resulting in lower spectral acceleration values.

Furthermore, in the instances of the Nurdağı (Mw=6.6) and Yayladağ (Mw=6.4) events (Figure 4.27 and Figure 4.28), the displacement limit is exceeded in only one of the analyses for both events (Stations 2712 and 3124, respectively). Notably, these two stations stood out with the highest PGA and PGV values among the set of five. The main conclusion based on the displacement results is that displacements have a decisive role in terms of TBI design, especially for bridges in earthquake prone regions. It is important to highlight that the investigated bridge has a column length of 6.92 meters. In the case of more slender columns the deck longitudinal displacements under seismic action are also expected to be higher than those determined in the current analyses. Considering the preceding discussion, deck horizontal displacements hold significant importance even for a typical, simply supported ordinary railway bridge. The upcoming section aims to establish the correlation between both ARSs and displacements concerning seismic intensity measures, specifically PGA and PGV values.

4.5.3 Influence of Intensity Measures on TBI Response

The design of railway bridges following the TBI analysis as outlined in UIC 774-3R (2001) predominantly relies on adhering to ARS limits, particularly when exposed solely to thermal and train loads. Building upon earlier results from analyses utilizing unscaled ground motions, the significance of displacements should be emphasized, especially concerning bridges susceptible to higher magnitude earthquakes. In this case, ARSs cease to be a valid design parameter.

ARS and deck displacement responses explained in the previous sections offer a qualitative understanding of the variation of these parameters along the bridge under different ground motions. However, presenting a collective overview of all conducted analyses in relation to seismic intensity measures PGA, PGV, Housner-Intensity (H-I) and Cumulative Absolute Velocity (CAV) would offer a more comprehensive illustration.

Relation of maximum ARSs with respect to PGA and PGV values is provided in Figure 4.30a and Figure 4.30b respectively. In Figure 4.30a, it is evident that as the PGA of the ground motion increases, there is a slight rise in the maximum tensile ARSs. The limited increase in the tensile ARSs with PGA values can be attributed to a significant portion of the initial tensile ARS being established during the first stage of NHTA due to static loads. Variation of maximum compressive ARSs with PGA level shows a different behavior. While the maximum compressive ARSs increase initially with respect to PGA, the rate of this increase diminishes notably as PGA values approach to approximately 350 cm/s² and remains almost becoming unchanged for higher PGA values. This behavior illustrates that beyond a specific threshold of lateral load, attributed to the yielding of RDCs, the rails cease to bear additional force and begin to slide atop the bridge structure. A similar trend is valid with respect to PGV values, as provided in Figure 4.30b. At a PGV value of approximately 40 cm/s, a similar pattern emerges, where the maximum rail in compressive stress stays almost the same.

Figure 4.31 presents deck longitudinal displacements in relation to both PGA and PGV values. A noticeable increasing trend in displacements is evident with both PGA and PGV values. Notably, for PGA values exceeding 300 cm/s² and PGV values exceeding 40 cm/s, deck longitudinal displacements exceed the 18 mm level. These specific thresholds can serve as indicative parameters governing the design process.

Relation of maximum ARSs with respect to H-I and CAV values is provided in Figure 4.32a and Figure 4.32b respectively. As depicted in the figures, for tensile ARSs, there is a limited increase with respect to increased H-I and CAV due to the initial state of the tensile ARSs at the first stage of NHTA due to static loads. On the other hand, variation of compressive ARSs initially increases with respect to H-I and CAV values. The rate of increase diminishes after 200 cm of H-I and 1500 cm/s of CAV value.

Figure 4.33 presents maximum longitudinal deck displacements in relation to H-I and CAV values. Similar to the relation of deck displacements in relation to PGA and PGV values, a noticeable increasing trend in deck displacements is evident with respect to H-I and CAV values. For H-I values exceeding 140 cm and CAV values exceeding 1200 cm/s, deck displacements exceed the 18 mm level margin left for the seismic effects.

In Elhout's study (2020), the PGA/PGV ratio served as an empirical parameter for assessing ground motion frequency content and classifying ground motion sets in NTHAs. The relationship between PGA/PGV (g/m/s) and maximum ARSs, as well as relative displacements, is depicted in Figure 4.34a and Figure 4.34b, respectively. Notably, both ARS and relative displacement data were populated in the intermediate range of PGA/PGV ratios (0.8-1.2 g/m/s), as defined by Tso et al. (1992). Beyond a PGA/PGV ratio of 1.2 g/m/s, corresponding to the high range category, relative displacements consistently remained below the specified limits. However, it is worth noting that this trend is not as clear when considering ARSs.

4.5.4 Acceleration Response at Different Locations on Bridge

The acceleration response was extracted from Pazarcık Earthquake (Mw=7.7) simulation at Station 4625 at several different locations on the bridge to discern the influence of RDCs on rail accelerations, particularly focusing on the amplification of ground motion. As a result, specific locations, such as the footing base, pier column top, deck, and rail centers atop the columns, were chosen for presentation of the acceleration results. To assess the impact of RDCs on the overall response, a parallel analysis was conducted using linear elastic RDC properties. These properties mirrored the stiffness of the initial nonlinear hysteretic curves, originally derived from the unloaded UIC 774-3R (2001) curves and RDCs remained linear elastic throughout the NTHA. Figure 4.35a and Figure 4.35b present the acceleration responses utilizing bilinear and linear RDCs, respectively. Evidently, the ground motion records and acceleration responses at the footing base exhibit identical patterns. However, noticeable amplification is observed at both the column top and deck center, which aligns with a consistent trend due to their connections via rigid links and elastomeric bearings, as illustrated in Figure 3.2. However, the rail elements exhibit a different response. With the use of bilinear RDCs, these elements experienced additional amplification, reaching an acceleration value of approximately 1.7g at a time of around the 60 seconds, as depicted in Figure 4.35a. In the case of linear elastic RDCs, on the other hand, no such amplification is observed in rail elements. In this case the rail accelerations remained consistent at approximately 0.75 g with those of the deck center elements, as depicted in Figure 4.35b. Therefore, it can be concluded that “yielding” of RDCs caused amplification of accelerations on rails at pier location more than two times when compared with the case of nonyielding RDCs.

Table 4.1 Selected ground motions

Pazarcık, Kahramanmaraş (Mw = 7.7)

Epicenter Distance, km	Number	Station Name (Scale Factor)
0-15	1	4615
15-30	5	NAR, 4616, 4630, 4625, 4632
30-50	3	2703, 4620, 8002
50-100	3	8004, 2707, 2716
100-150	3	3132, 3142, 0143

Elbistan, Kahramanmaraş (Mw = 7.6)

Epicenter Distance, km	Number	Station Name
0-15	-	-
15-30	1	4631
30-50	1	4611
50-100	7	4409, 4620, 4625, 4617, 4612, 4406, NAR
100-150	6	4405, 0131, 8002, 0133, 5809, 0122

Nurdağı, Gaziantep (Mw = 6.6)

Epicenter Distance, km	Number	Station Name
0-15	1	4616
15-30	5	2712, 4615, NAR, 4624, 4625
30-50	3	4620, 4619, 2718
50-100	3	2716, 2711, 3138
100-150	3	3142, 3115, 3126

Table 4.1 (continued)

Yayladağ, Hatay (Mw = 6.4)

Epicenter Distance, km	Number	Station Name
0-15	1	3140
15-30	4	3147, 3136, 3125, 3124
30-50	2	3141, 3135
50-100	5	3146, 3133, 3115, 3117, 3121
100-150	3	2716, 2708, 3305

Samandağ, Hatay (Mw= 5.8)

Epicenter Distance, km	Number	Station Name
0-15	-	-
15-30	4	3124, 3135, 3141, 3136
30-50	4	3115, 3147, 3142, 3116
50-100	4	3121, 3138, 3143, 2716
100-150	3	2718, 3305, 0122

Yeşilyurt, Malatya (ML= 5.8)

Epicenter Distance, km	Number	Station Name
0-15	-	-
15-30	1	4406
30-50	2	4412, 4407
50-100	9	4404, 2310, 4405, 2309, 0213, 4413, 0205, 4409, 4410
100-150	3	2409, 5809, 4625

Table 4.1 (continued)

Islahiye, Gaziantep (ML= 5.7)

Epicenter Distance, km	Number	Station Name
0-15	4	2708, 8002, 2712, 2718
15-30	2	2716, 2717
30-50	4	3143, 8003, 4616, 3137
50-100	3	4624, 4613, 0131
100-150	2	3124, 0140

Doğanşehir, Malatya (Mw= 5.6)

Epicenter Distance, km	Number	Station Name
0-15	-	-
15-30	1	4408
30-50	2	4631, 4406
50-100	7	4611, 4409, 4412, 6304, 4628, 4624, 4617
100-150	5	2704, 4405, 4407, 2703, 3802

Yeşilyurt, Malatya (Mw= 5.6)

Epicenter Distance, km	Number	Station Name
0-15	-	-
15-30	1	4406
30-50	4	4412, 0216, 0215, 4414
50-100	5	4407, 4404, 0210, 4405, 4631
100-150	5	NAR, 2307, 2302, 6203, 2710

Table 4.1 (continued)

Nurdağı, Gaziantep (ML= 5.6)

Epicenter Distance, km	Number	Station Name
0-15	-	-
15-30	3	4615, NAR, 2712
30-50	6	4624, 2703, 8002, 4614, 2718, 4617
50-100	3	2711, 3143, 3137
100-150	3	0127, 0120, 3124

Pazarcık, Kahramanmaraş (Mw= 5.5)

Epicenter Distance, km	Number	Station Name
0-15	1	4615
15-30	-	-
30-50	3	2712, 2703, 2711
50-100	6	4611, 2710, 4613, 8003, 8004, 3134
100-150	5	3121, 0131, 3116, 3115, 6304

Ekinözü, Kahramanmaraş (ML= 5.5)

Epicenter Distance, km	Number	Station Name
0-15	-	-
15-30	-	-
30-50	1	4611
50-100	9	4409, 4412, 0213, NAR, 5807, 4613, 0132, 4410, 4412
100-150	5	4405, 3804, 2703, 0127, 0209

Table 4.2 Total number of ground motions used in the analyses

Mw/ML Range	Total Number of Earthquake Events	Total Number of Ground Motions
5.5-6.0	8	120
6.0-6.5	1	15
6.5-7.0	1	15
>7.0	2	30

Table 4.3 Scale factors used for selected ground motions

Pazarcık, Kahramanmaraş (Mw = 7.7)				
4615	**NAR**	**4616**	**4630**	**4625**
0.17	0.33	0.133	0.74	0.22
4632	**2703**	**4620**	**8002**	**8004**
0.34	0.70	0.33	3.00	0.56
2707	**2716**	**3132**	**3142**	**0143**
1.40	0.47	0.172	0.34	3.90
Elbistan, Kahramanmaraş (Mw = 7.6)				
4631	**4611**	**4409**	**4620**	**4625**
0.28	0.96	1.45	1.95	1.15
4617	**4612**	**4406**	**NAR**	**4405**
1.76	0.96	0.40	1.60	1.65
0131	**8002**	**0133**	**5809**	**0122**
0.49	1.80	1.25	1.35	1.90
Nurdağı, Gaziantep (Mw = 6.6)				
4616	**2712**	**4615**	**NAR**	**4624**
0.44	0.20	1.05	1.40	0.45

Table 4.3 (continued)

Nurdağı, Gaziantep (Mw = 6.6)

4625	**4620**	**4619**	**2718**	**2716**
1.00	0.52	0.73	0.37	0.81
2711	**3138**	**3142**	**3115**	**3126**
5.10	0.79	1.39	1.39	0.60

Yayladağ, Hatay (Mw = 6.4)

3140	**3147**	**3136**	**3125**	**3124**
0.45	6.20	0.42	0.18	0.22
3141	**3135**	**3146**	**3133**	**3115**
0.305	0.29	0.63	2.67	1.00
3117	**3121**	**2716**	**2708**	**3305**
0.48	0.88	2.40	2.12	7.20

Samandağ, Hatay (Mw= 5.8)

3124	**3135**	**3141**	**3136**	**3115**
4.15	5.80	9.50	4.70	20.00
3147	**3142**	**3116**	**3121**	**3138**
156.00	51.50	70.00	12.50	16.50
3143	**2716**	**2718**	**3305**	**0122**
58.50	27.50	44.50	67.00	224.00

Yeşilyurt, Malatya (ML= 5.8)

4406	**4412**	**4407**	**4404**	**2310**
1.01	2.93	10.10	2.35	2.55
4405	**2309**	**0213**	**4413**	**0205**
5.65	6.10	3.80	27.00	8.30
4409	**4410**	**2409**	**5809**	**4625**
8.30	5.70	8.50	10.40	5.80

Table 4.3 (continued)

Islahiye, Gaziantep (ML= 5.7)

2708	**8002**	**2712**	**2718**	**2716**
0.355	1.55	1.35	3.60	7.80
2717	**3143**	**8003**	**4616**	**3137**
40.00	9.65	6.55	1.29	18.00
4624	**4613**	**0131**	**3124**	**0140**
1.61	5.87	28.70	2.92	22.70

Doğanşehir, Malatya (Mw= 5.6)

4408	**4631**	**4406**	**4611**	**4409**
2.42	6.50	16.00	18.60	34.70
4412	**6304**	**4628**	**4624**	**4617**
41.50	20.90	32.00	13.90	51.60
2704	**4405**	**4407**	**2703**	**3802**
26.45	39.00	75.00	12.52	37.00

Yeşilyurt, Malatya (Mw= 5.6)

4406	**4412**	**0216**	**0215**	**4414**
13.50	20.50	27.50	21.00	4.40
4407	**4404**	**0210**	**4405**	**4631**
46.00	17.00	21.00	36.50	49.00
NAR	**2307**	**2302**	**6203**	**2710**
87.00	166.00	110.00	58.50	18.00

Nurdağı, Gaziantep (Mw= 5.6)

4406	**4412**	**0216**	**0215**	**4414**
13.50	20.50	27.50	21.00	4.40
4407	**4404**	**0210**	**4405**	**4631**
46.00	17.00	21.00	36.50	49.00

Table 4.3 (continued)

Nurdağı, Gaziantep (Mw= 5.6)

NAR	2307	2302	6203	2710
87.00	166.00	110.00	58.50	18.00

Pazarcık, Kahramanmaraş (Mw = 5.5)

4615	2712	2703	2611	4611
2.45	4.40	3.50	26.70	42.00
2710	**4613**	**8003**	**8004**	**3134**
15.80	32.60	26.50	23.80	16.40
3121	**0131**	**3116**	**3115**	**6304**
315.00	54.00	19.00	11.30	20.50

Ekinözü, Kahramanmaraş (ML= 5.5)

4611	4409	4612	0213	NAR
5.80	25.50	1.66	15.70	51.50
5807	**4613**	**0132**	**4410**	**4412**
17.20	19.00	63.00	36.50	33.50
4405	**3804**	**2703**	**0127**	**0209**
45.00	86.00	20.50	34.40	58.40

Table 4.4 Summary of maximum ARSs

Location	Magnitude	ARS Maximum Tension	ARS Maximum Compression
Pazarcık, Kahramanmaraş	Mw=7.7	33.2	-41.4
Elbistan, Kahramanmaraş	Mw=7.6	33.5	-41.0
Nurdağı, Gaziantep	Mw=6.6	33.1	-43.0
Yayladağ, Hatay	Mw=6.4	32.8	-41.0
Samandağ, Hatay	Mw=5.8	34.4	-41.9
Yeşilyurt, Malatya	ML=5.8	33.1	-41.3
Islahiye, Gaziantep	ML=5.7	40.8	-41.9
Doğanşehir, Malatya	Mw=5.6	35.7	-42.3
Yeşilyurt, Malatya	Mw=5.6	36.7	-41.0
Nurdağı, Gaziantep	ML=5.6	33.0	-41.3
Pazarcık, Kahramanmaraş	Mw=5.5	37.5	-41.3
Ekinözü, Kahramanmaraş	ML=5.5	33.4	-41.9

Table 4.5 Design limits for TBI given by Taiwan High-Speed Railway Provision (2000)

	ARS	Displacement
Braking, traction and 20^0C temperature variation between rails and deck	-72/+92 MPa	7 mm: between decks or deck and abutment, 4 mm: between bridge deck and rail.
Braking, type II earthquake (service earthquake defined as 1/3 x repairable damage earthquake) and 20^0C temperature variation between rails and deck	-147/+167 MPa	25 mm : between decks or between deck and abutment

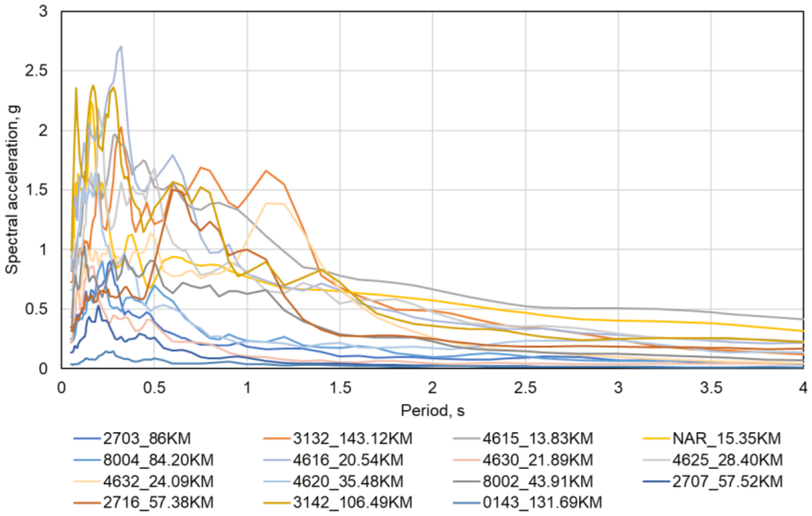

Figure 4.1. Unscaled Spectra of selected ground motions for Pazarcık Kahramanmaraş Mw = 7.7 Earthquake

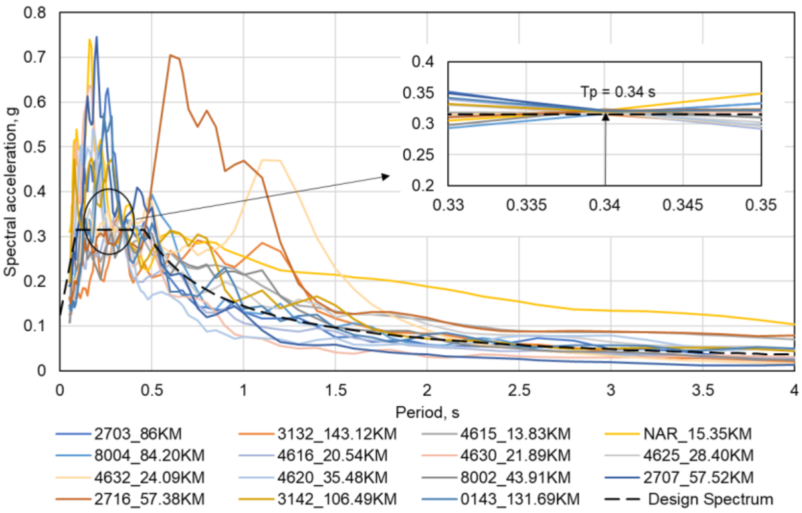

Figure 4.2. Scaled Spectra of selected ground motions for Pazarcık Kahramanmaraş Mw = 7.7 Earthquake

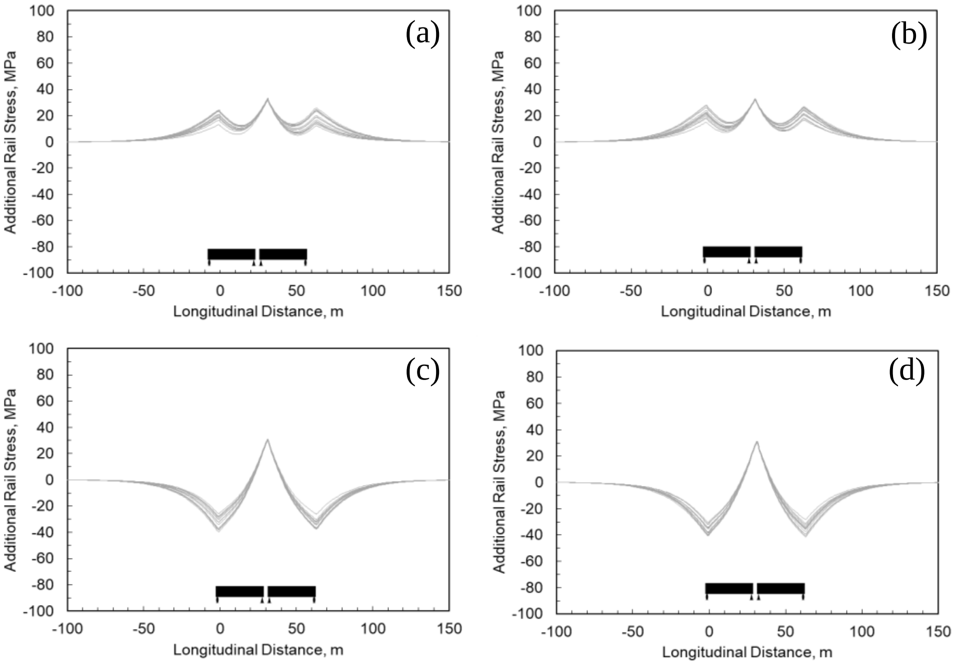

Figure 4.3. ARS results for Pazarcık Kahramanmaraş Mw=7.7 Earthquake: (a) XH1_YH2 maximum tensile; (b) XH2_YH1 maximum tensile; (c) XH1_YH2 maximum compressive; (d) XH2_YH1 maximum compressive

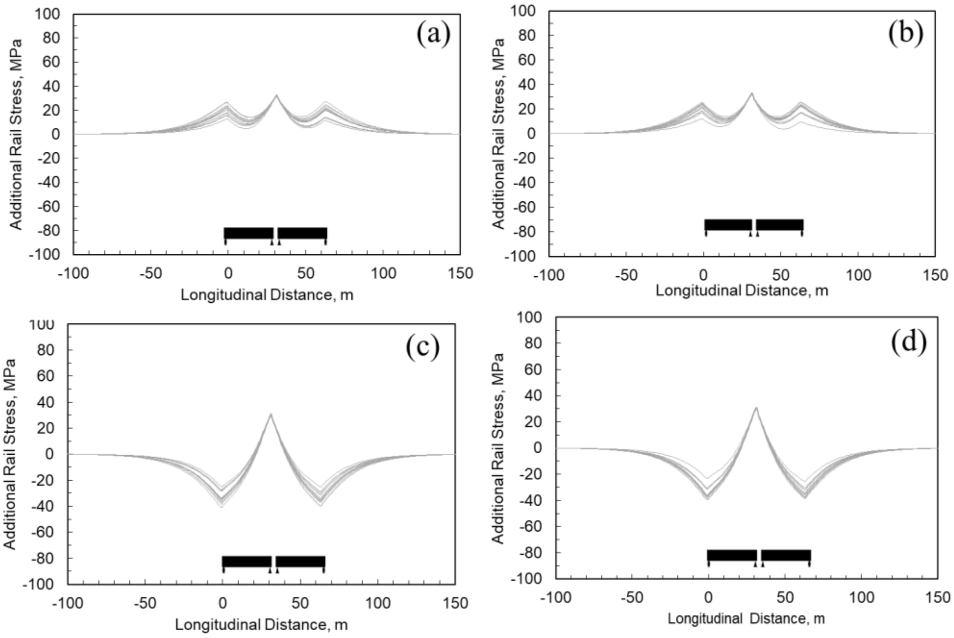

Figure 4.4. ARS results for Elbistan Kahramanmaraş Mw=7.6 Earthquake: (a) XH1_YH2 maximum tensile; (b) XH2_YH1 maximum tensile; (c) XH1_YH2 maximum compressive; (d) XH2_YH1 maximum compressive

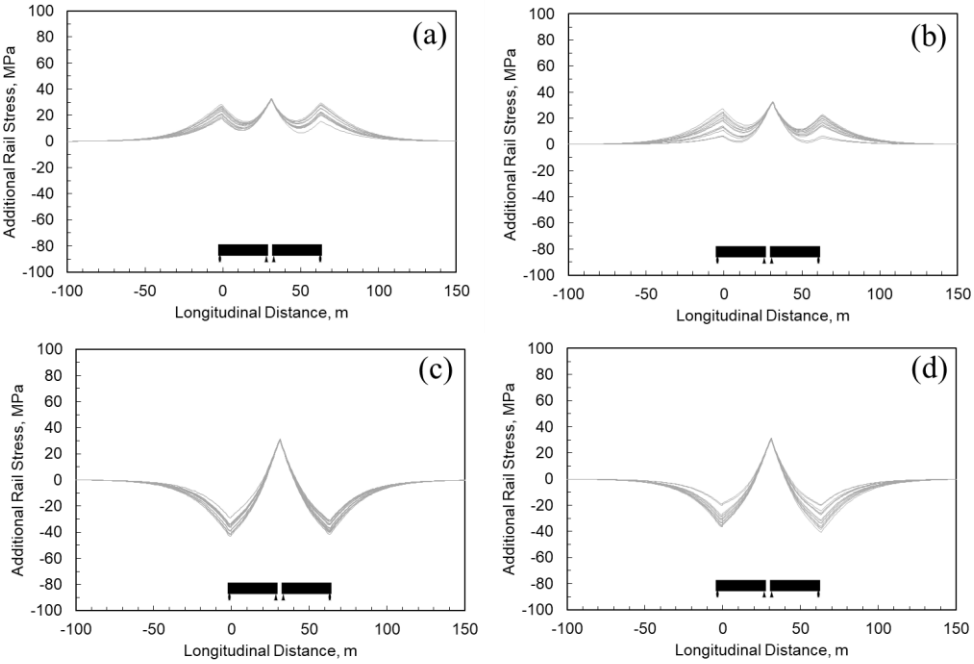

Figure 4.5. ARS results for Nurdağı Gaziantep Mw=6.6 Earthquake: (a) XH1_YH2 maximum tensile; (b) XH2_YH1 maximum tensile; (c) XH1_YH2 maximum compressive; (d) XH2_YH1 maximum compressive

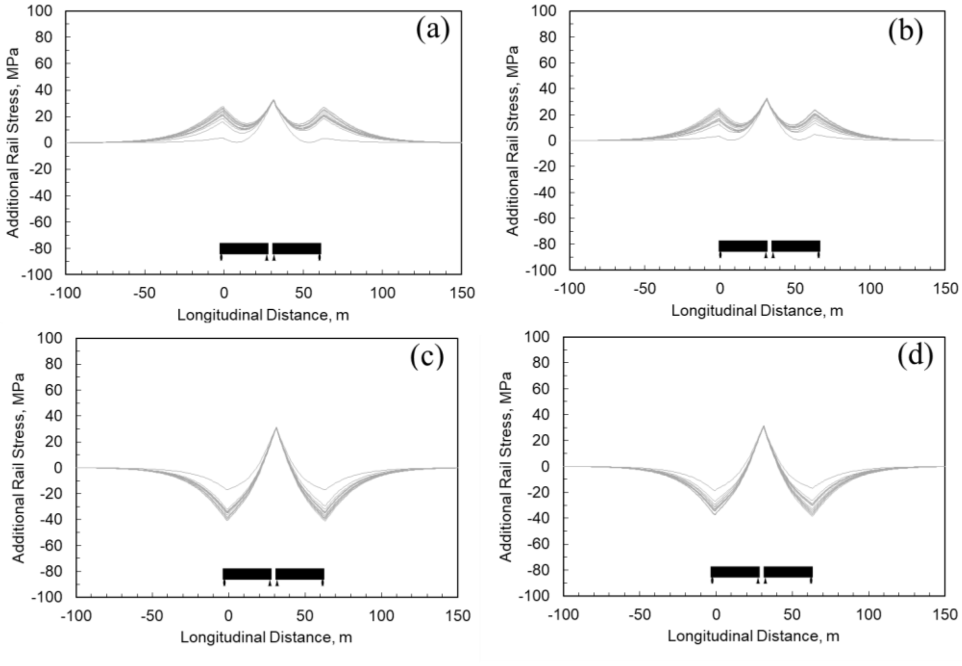

Figure 4.6. ARS results for Yayladağ Hatay Mw=6.4 Earthquake: (a) XH1_YH2 maximum tensile; (b) XH2_YH1 maximum tensile; (c) XH1_YH2 maximum compressive; (d) XH2_YH1 maximum compressive

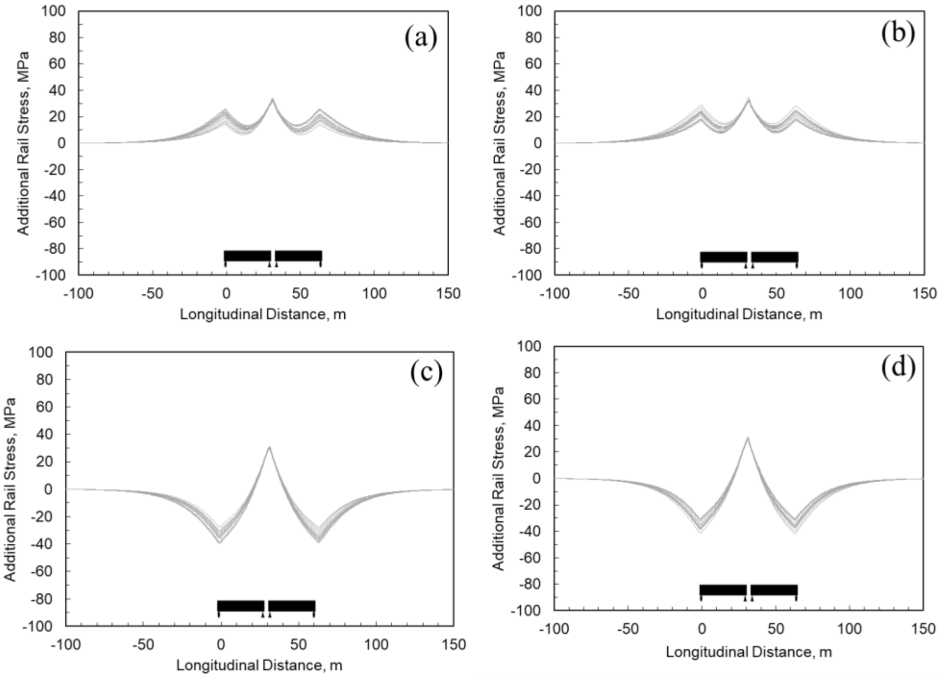

Figure 4.7. ARS results for Samandağ Hatay Mw=5.8 Earthquake: (a) XH1_YH2 maximum tensile; (b) XH2_YH1 maximum tensile; (c) XH1_YH2 maximum compressive; (d) XH2_YH1 maximum compressive

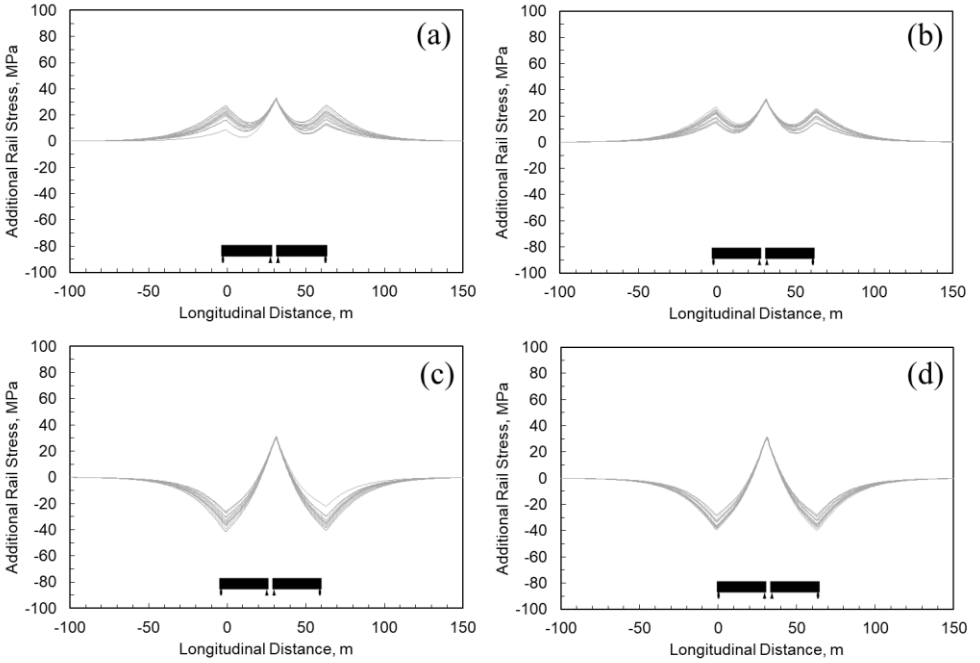

Figure 4.8. ARS results for Yeşilyurt Malatya ML=5.8 Earthquake: (a) XH1_YH2 maximum tensile; (b) XH2_YH1 maximum tensile; (c) XH1_YH2 maximum compressive; (d) XH2_YH1 maximum compressive

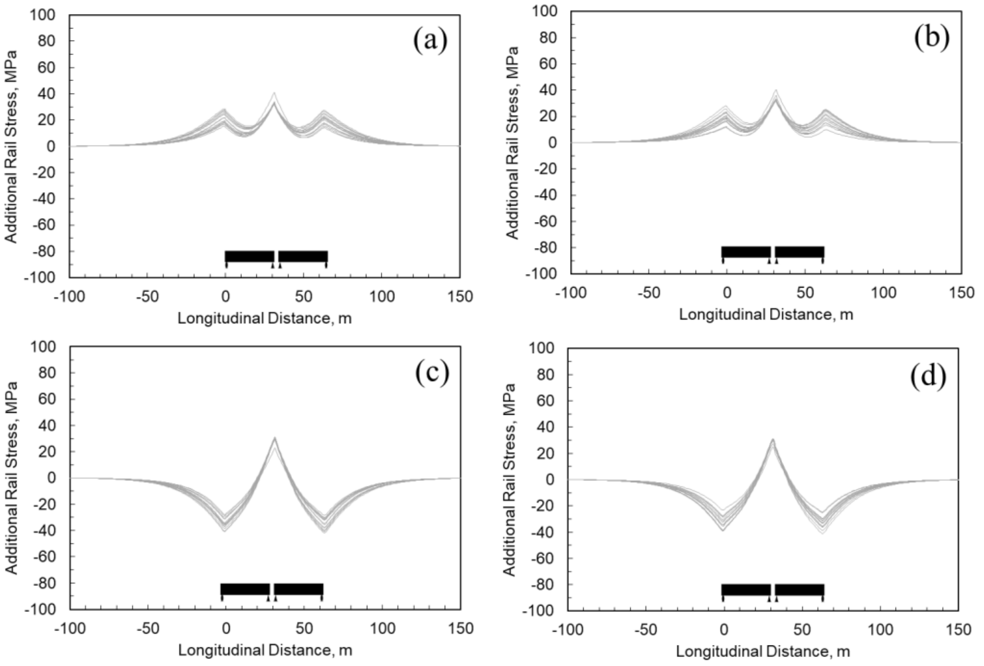

Figure 4.9. ARS results for Islahiye Gaziantep ML=5.7 Earthquake: (a) XH1_YH2 maximum tensile; (b) XH2_YH1 maximum tensile; (c) XH1_YH2 maximum compressive; (d) XH2_YH1 maximum compressive

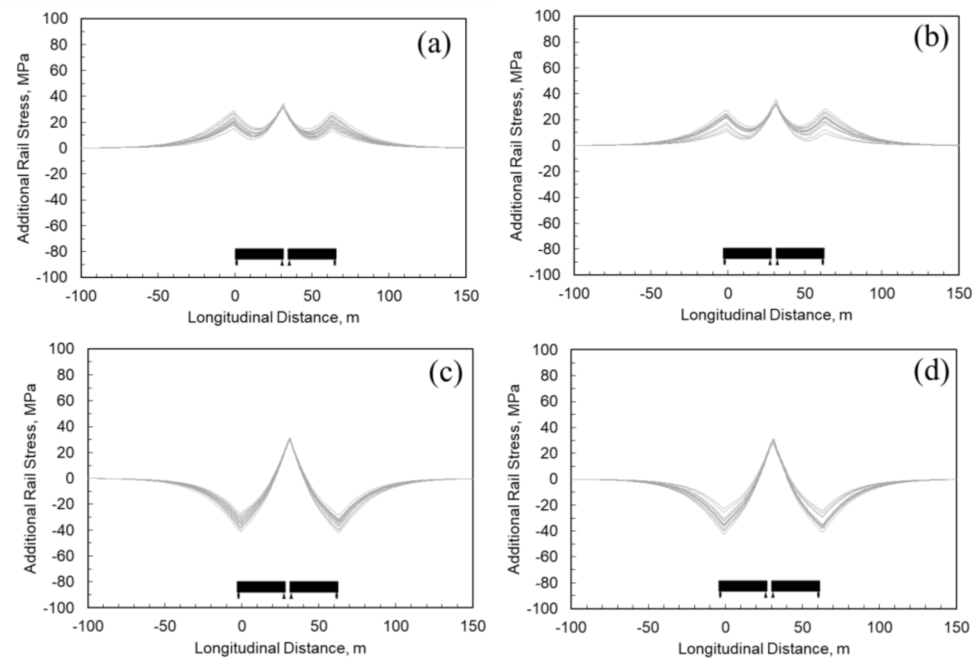

Figure 4.10. ARS results for Doğanşehir Malatya Mw=5.6 Earthquake: (a) XH1_YH2 maximum tensile; (b) XH2_YH1 maximum tensile; (c) XH1_YH2 maximum compressive; (d) XH2_YH1 maximum compressive

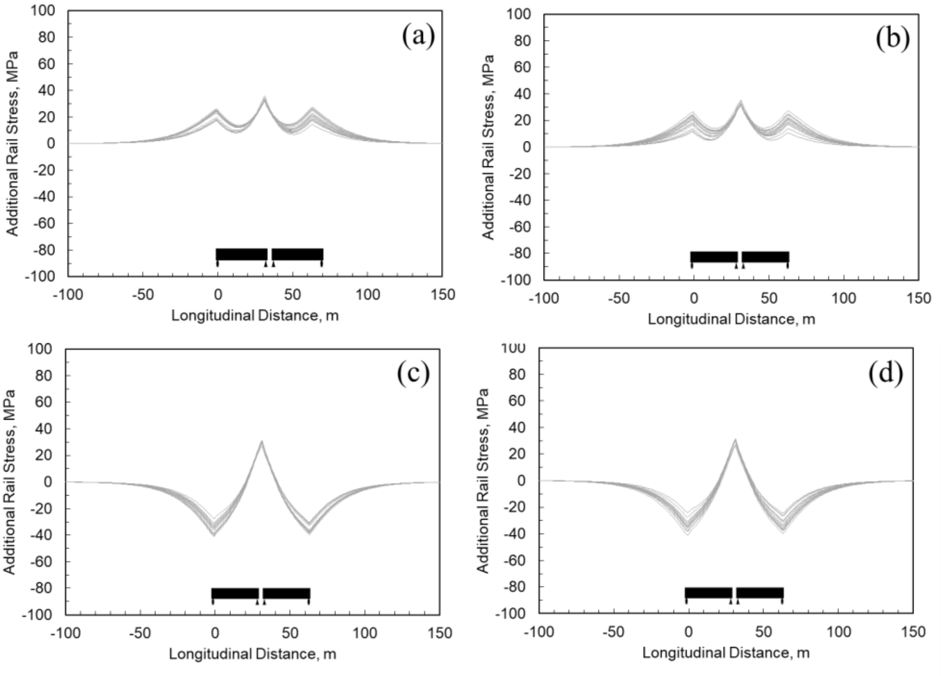

Figure 4.11. ARS results for Yeşilyurt Malatya Mw=5.6 Earthquake: (a) XH1_YH2 maximum tensile; (b) XH2_YH1 maximum tensile; (c) XH1_YH2 maximum compressive; (d) XH2_YH1 maximum compressive

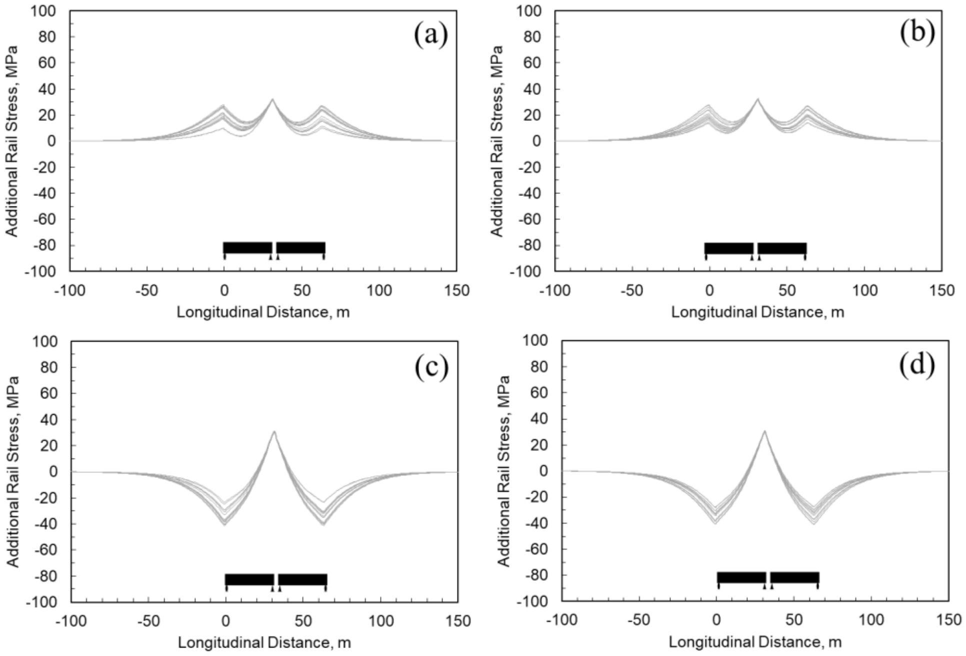

Figure 4.12. ARS results for Nurdağı Gaziantep ML=5.6 Earthquake: (a) XH1_YH2 maximum tensile; (b) XH2_YH1 maximum tensile; (c) XH1_YH2 maximum compressive; (d) XH2_YH1 maximum compressive

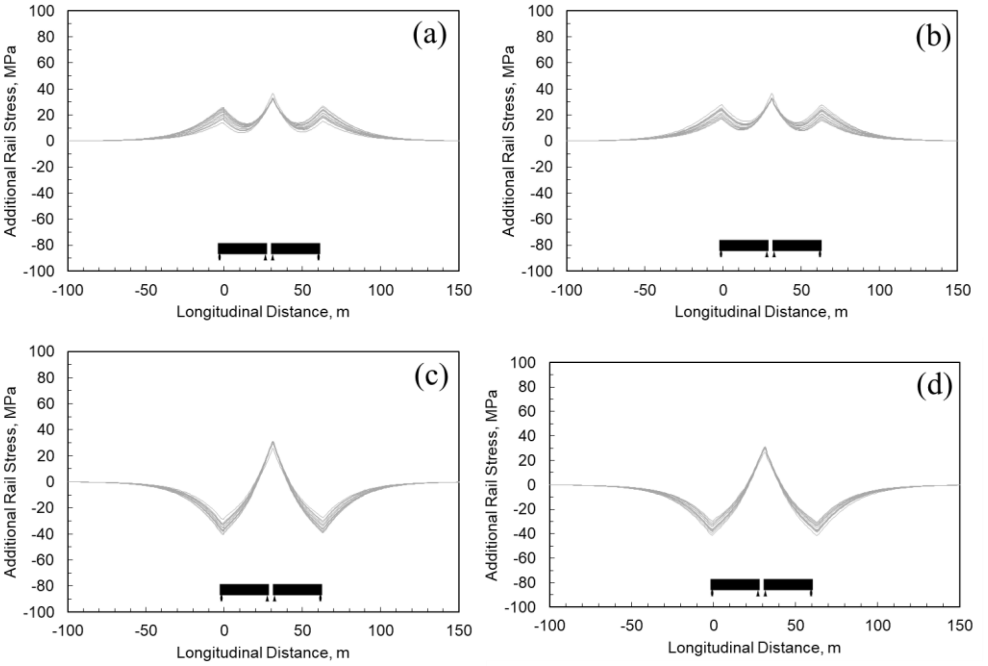

Figure 4.13. ARS results for Pazarcık Kahramanmaraş Mw=5.5 Earthquake: (a) XH1_YH2 maximum tensile; (b) XH2_YH1 maximum tensile; (c) XH1_YH2 maximum compressive; (d) XH2_YH1 maximum compressive

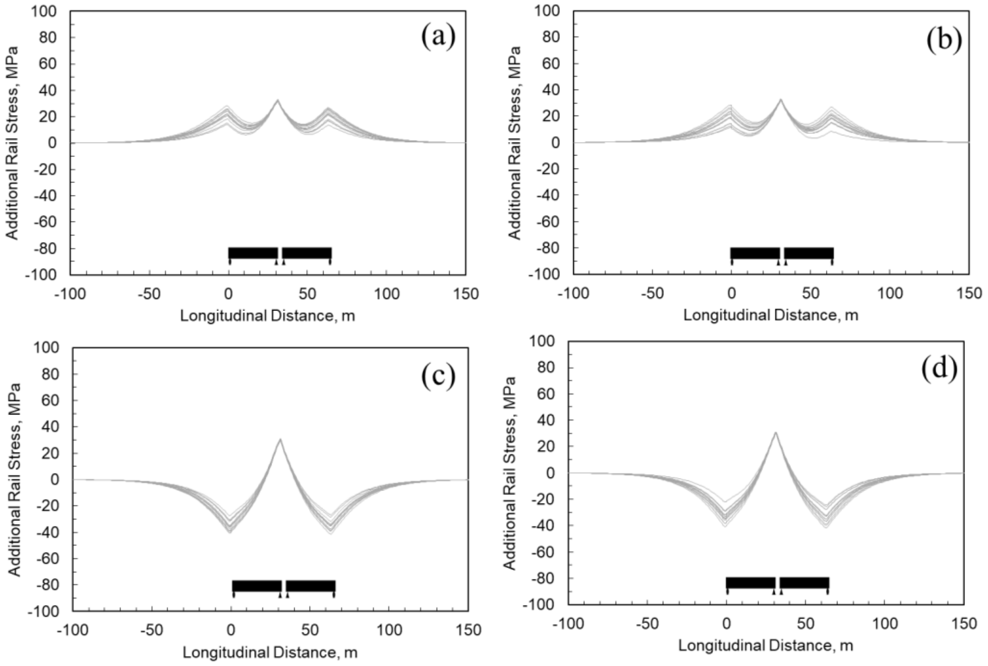

Figure 4.14. ARS results for Ekinözü Kahramanmaraş ML=5.5 Earthquake: (a) XH1_YH2 maximum tensile; (b) XH2_YH1 maximum tensile; (c) XH1_YH2 maximum compressive; (d) XH2_YH1 maximum compressive

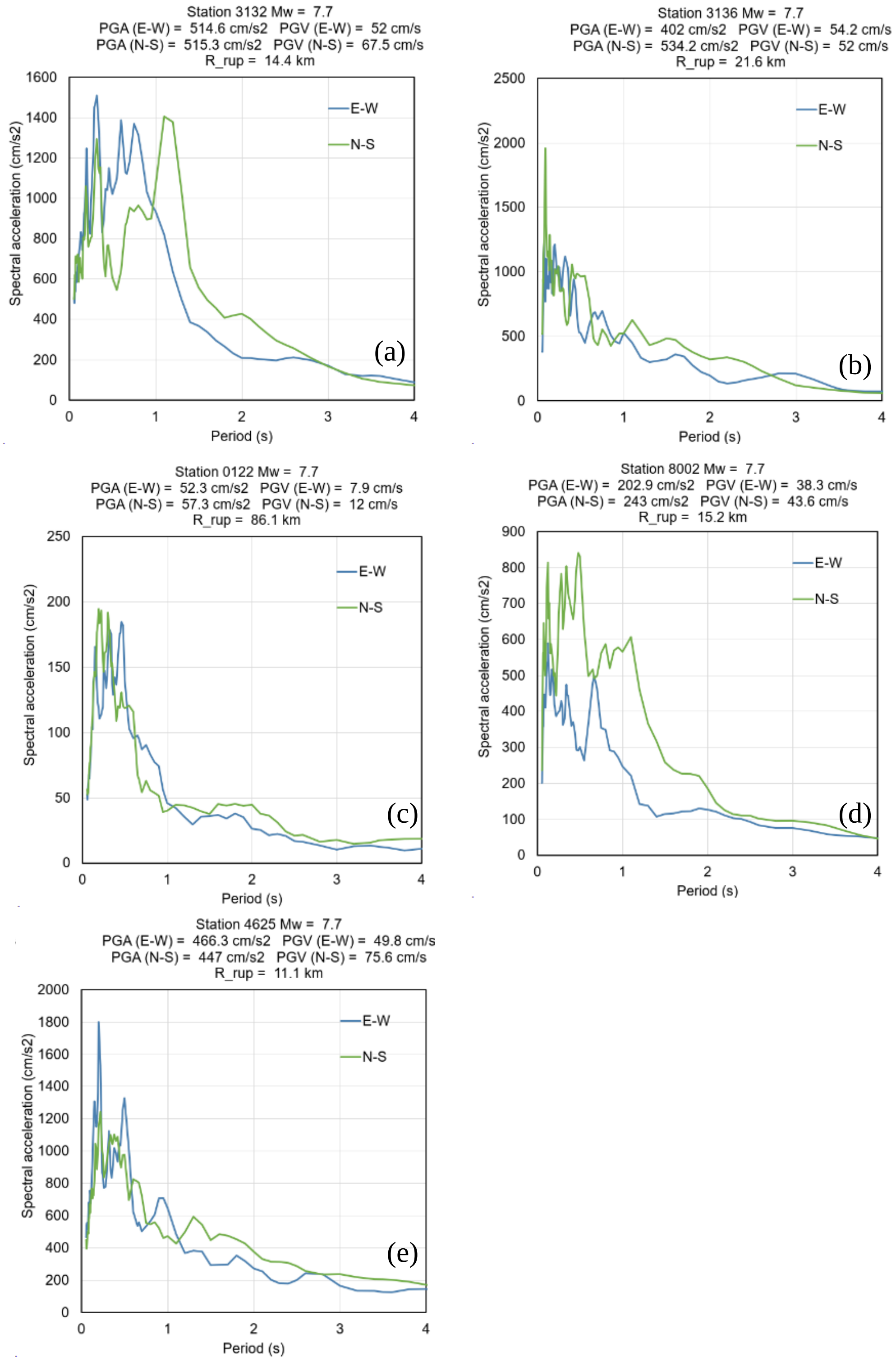
Station 3132 Mw = 7.7
PGA (E-W) = 514.6 cm/s2 PGV (E-W) = 52 cm/s
PGA (N-S) = 515.3 cm/s2 PGV (N-S) = 67.5 cm/s
R_rup = 14.4 km

Station 3136 Mw = 7.7
PGA (E-W) = 402 cm/s2 PGV (E-W) = 54.2 cm/s
PGA (N-S) = 534.2 cm/s2 PGV (N-S) = 52 cm/s
R_rup = 21.6 km

Station 0122 Mw = 7.7
PGA (E-W) = 52.3 cm/s2 PGV (E-W) = 7.9 cm/s
PGA (N-S) = 57.3 cm/s2 PGV (N-S) = 12 cm/s
R_rup = 86.1 km

Station 8002 Mw = 7.7
PGA (E-W) = 202.9 cm/s2 PGV (E-W) = 38.3 cm/s
PGA (N-S) = 243 cm/s2 PGV (N-S) = 43.6 cm/s
R_rup = 15.2 km

Station 4625 Mw = 7.7
PGA (E-W) = 466.3 cm/s2 PGV (E-W) = 49.8 cm/s
PGA (N-S) = 447 cm/s2 PGV (N-S) = 75.6 cm/s
R_rup = 11.1 km

Figure 4.15. Ground Motion spectra for Pazarcık Kahramanmaraş Mw =7.7 Earthquake: (a) Station 3132; (b) Station 3136; (c) Station 0122; (d) Station 8002; (e) Station 4625

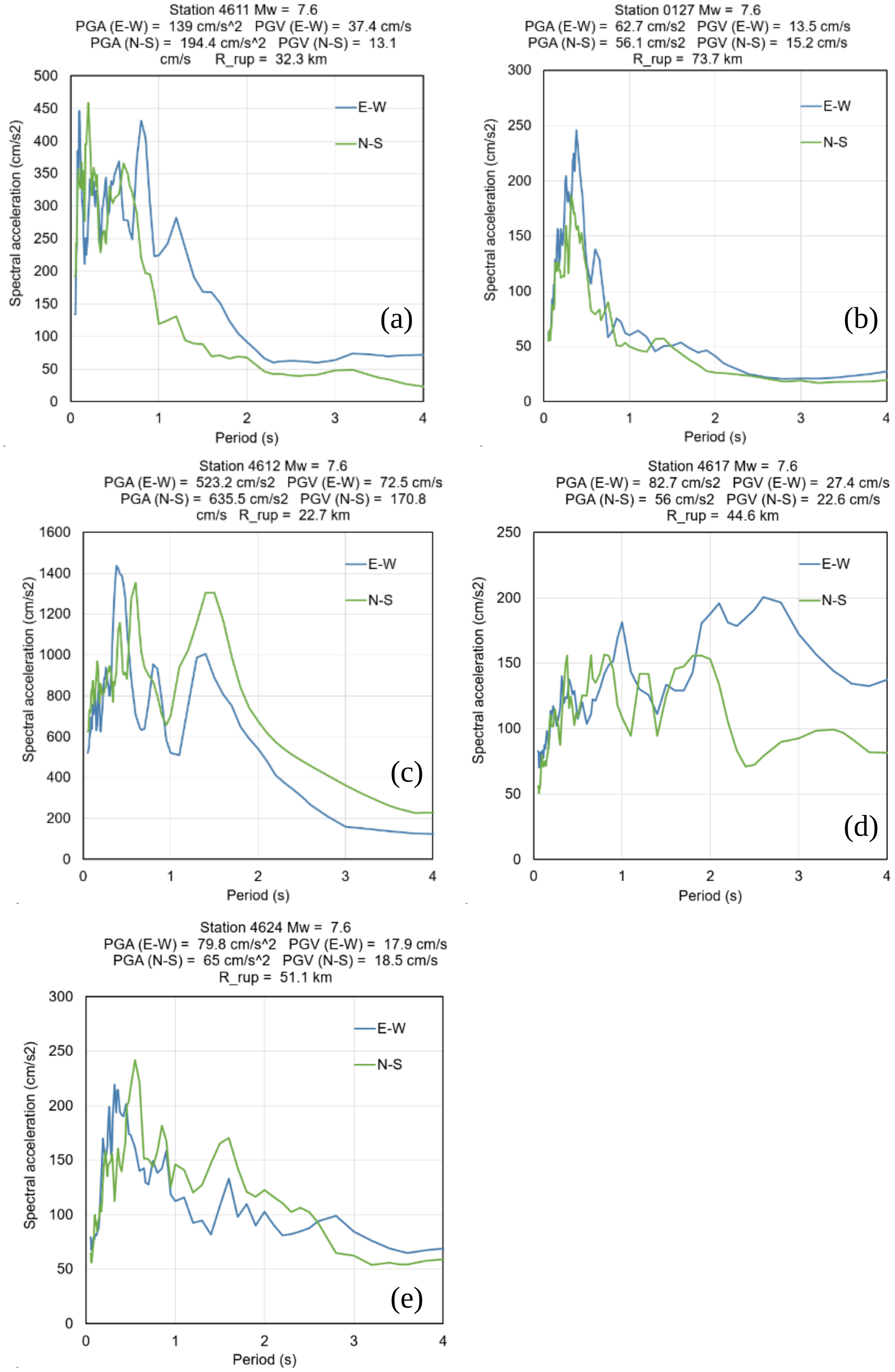

Figure 4.16. Ground Motion spectra for Elbistan Kahramanmaraş Mw =7.6 Earthquake: (a) Station 4611; (b) Station 0127; (c) Station 4612; (d) Station 4617; (e) Station 4624

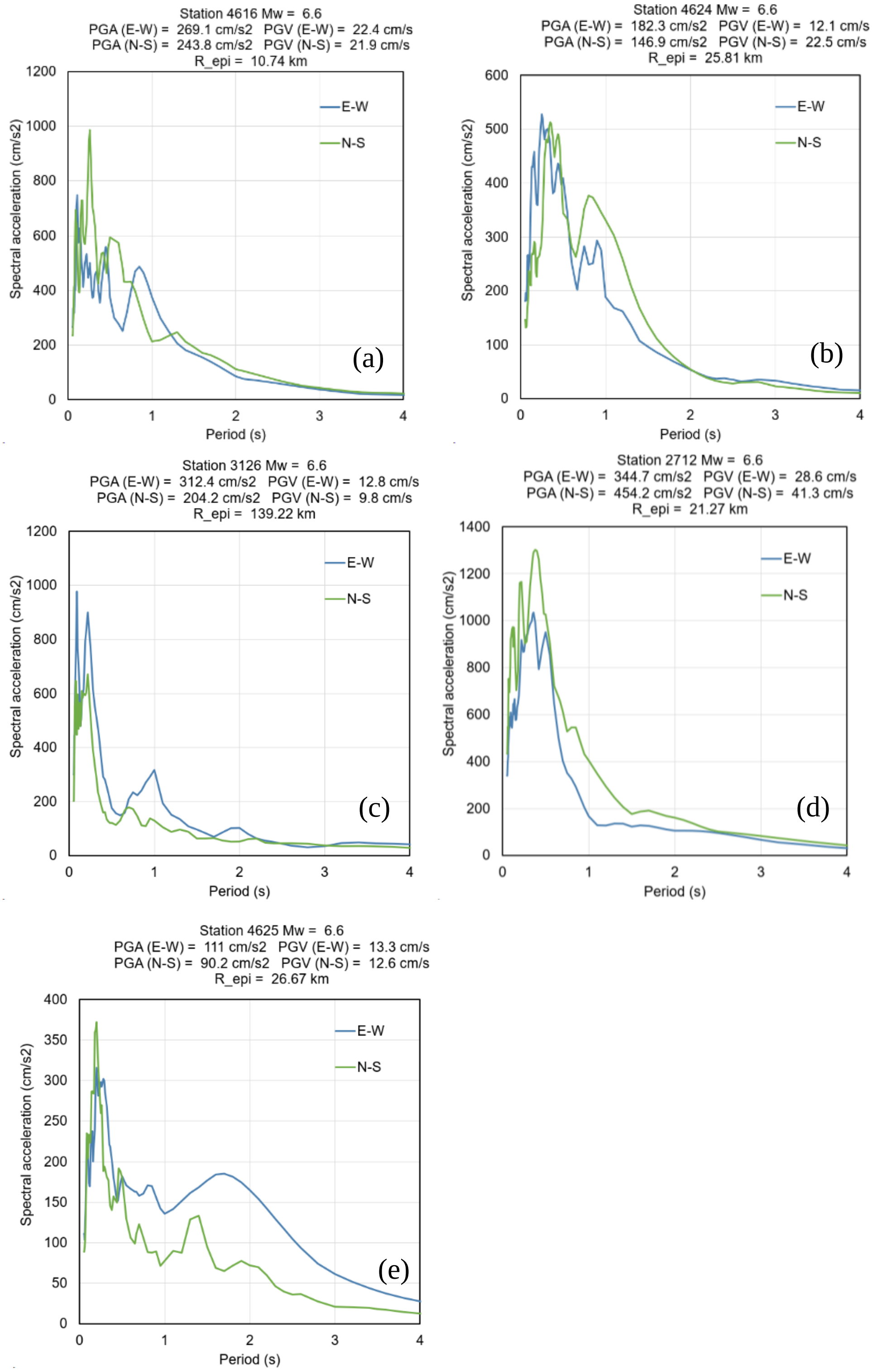

Figure 4.17. Ground Motion spectra for Nurdağı Gaziantep Mw = 6.6 Earthquake: (a) Station 4616; (b) Station 4624; (c) Station 3126; (d) Station 2712; (e) Station 4625

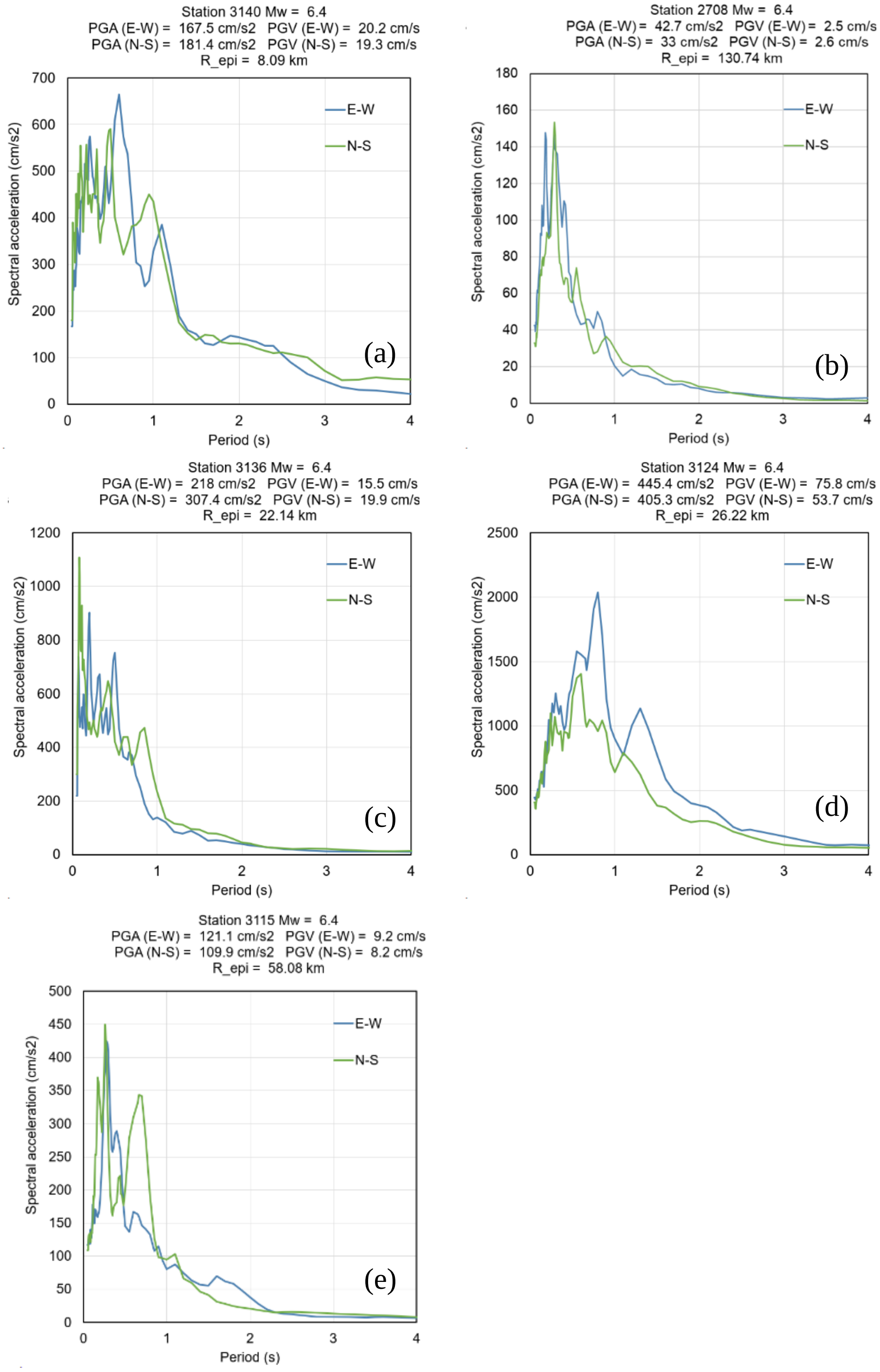

Figure 4.18. Ground Motion spectra for Yayladağ Hatay Mw = 6.4 Earthquake: (a) Station 3140; (b) Station 2708; (c) Station 3136; (d) Station 3124; (e) Station 3115

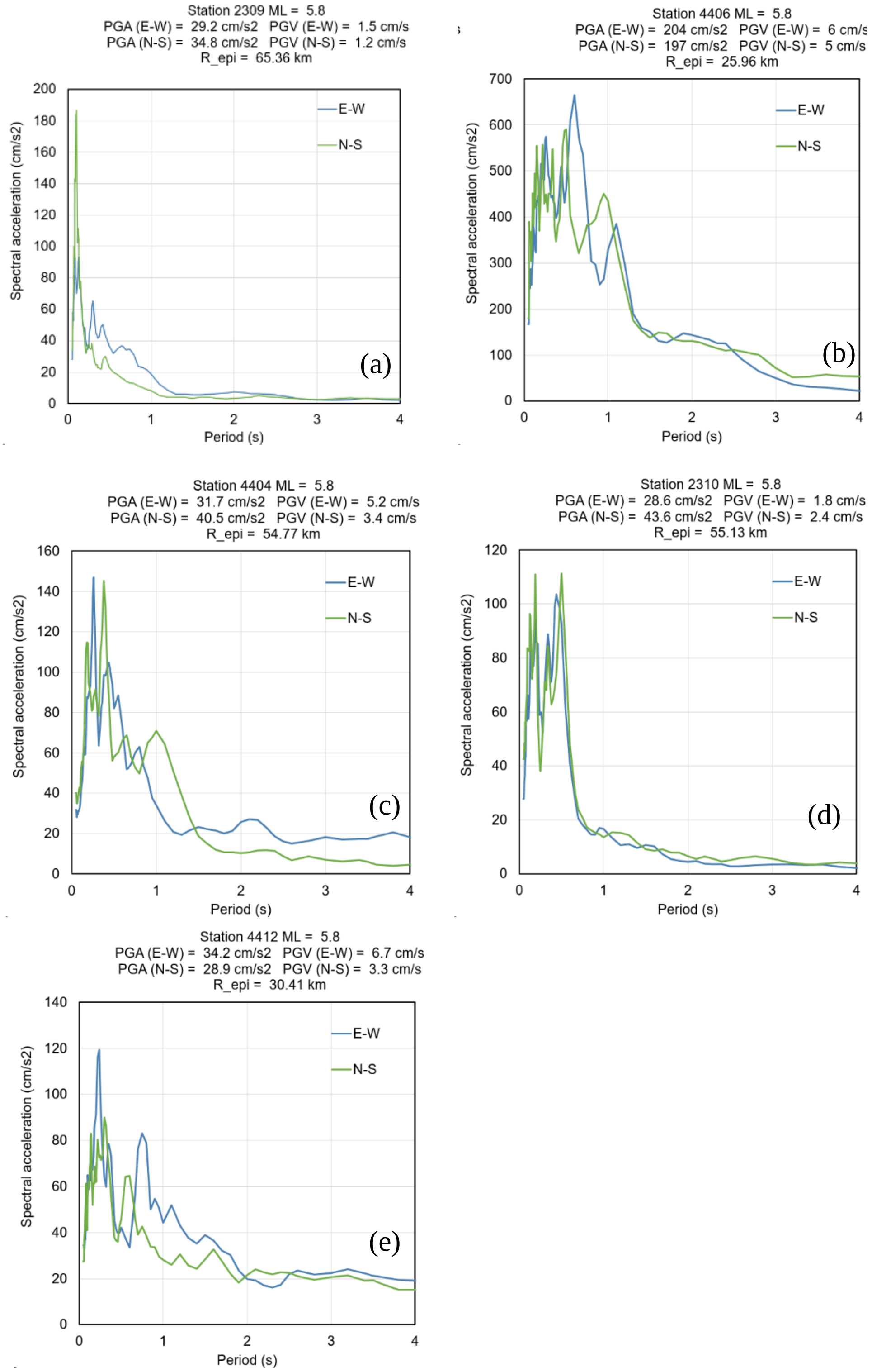

Figure 4.19. Ground Motion spectra for Yeşilyurt Malatya ML= 5.8 Earthquake: (a) Station 2309; (b) Station 4406; (c) Station 4404; (d) Station 2310; (e) Station 4412

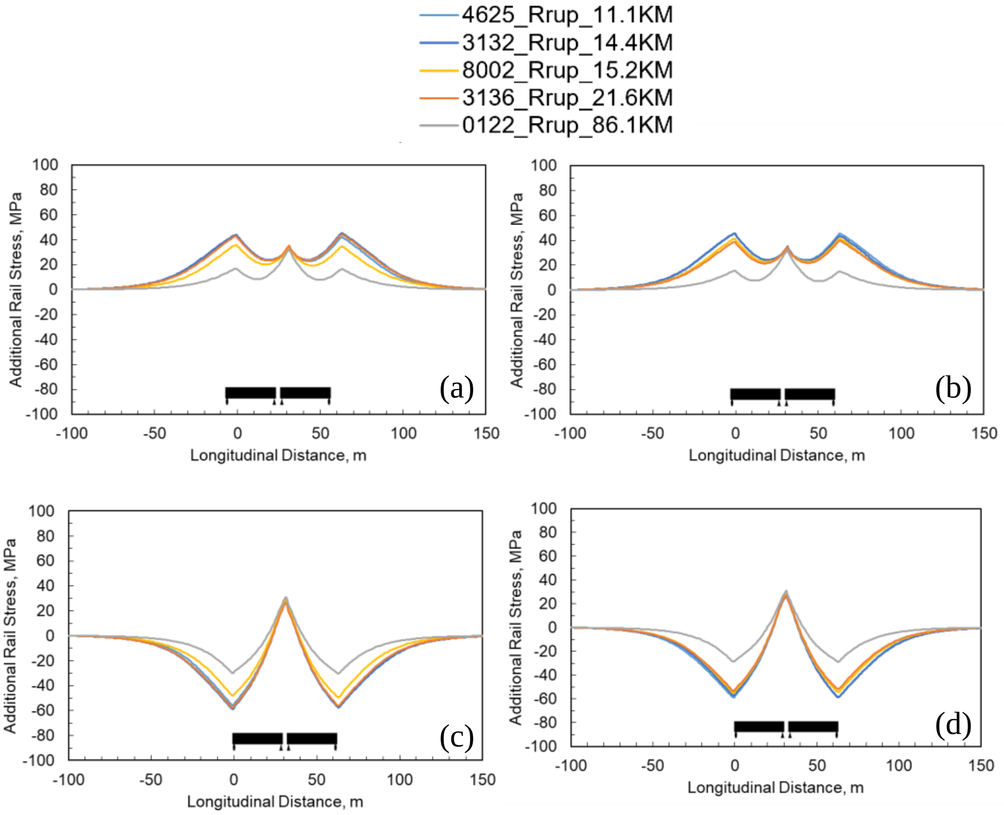

Figure 4.20. ARS results for Pazarcık Kahramanmaraş Mw=7.7 Earthquake: (a) XH1_YH2 maximum tensile; (b) XH2_YH1 maximum tensile; (c) XH1_YH2 maximum compressive; (d) XH2_YH1 maximum compressive

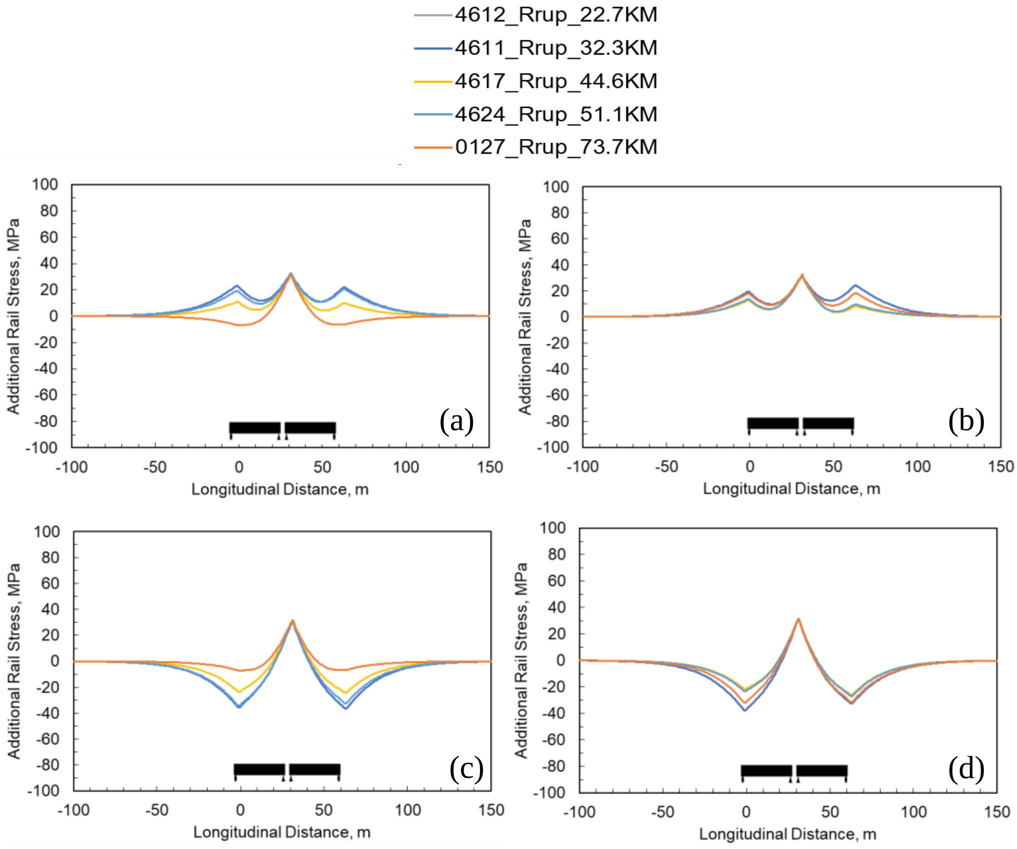

Figure 4.21. ARS results for Elbistan Kahramanmaraş Mw=7.6 Earthquake: (a) XH1_YH2 maximum tensile; (b) XH2_YH1 maximum tensile; (c) XH1_YH2 maximum compressive; (d) XH2_YH1 maximum compressive

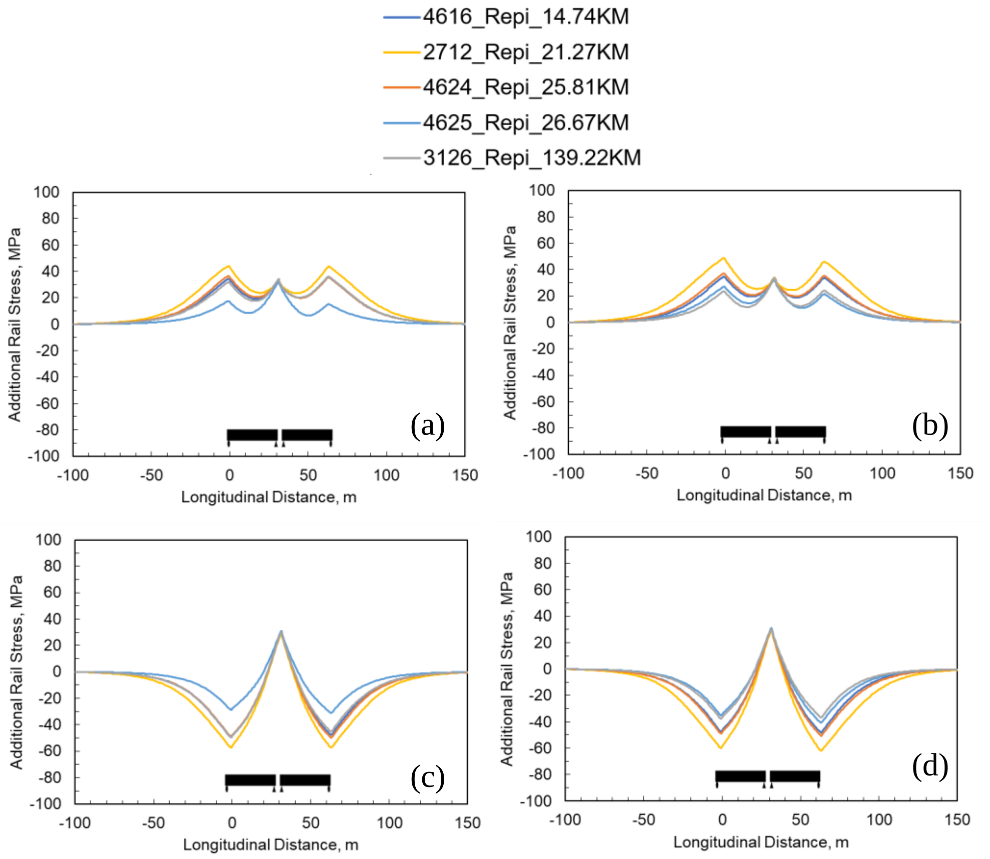

Figure 4.22. ARS results for Nurdağı Gaziantep Mw=6.6 Earthquake: (a) XH1_YH2 maximum tensile; (b) XH2_YH1 maximum tensile; (c) XH1_YH2 maximum compressive; (d) XH2_YH1 maximum compressive

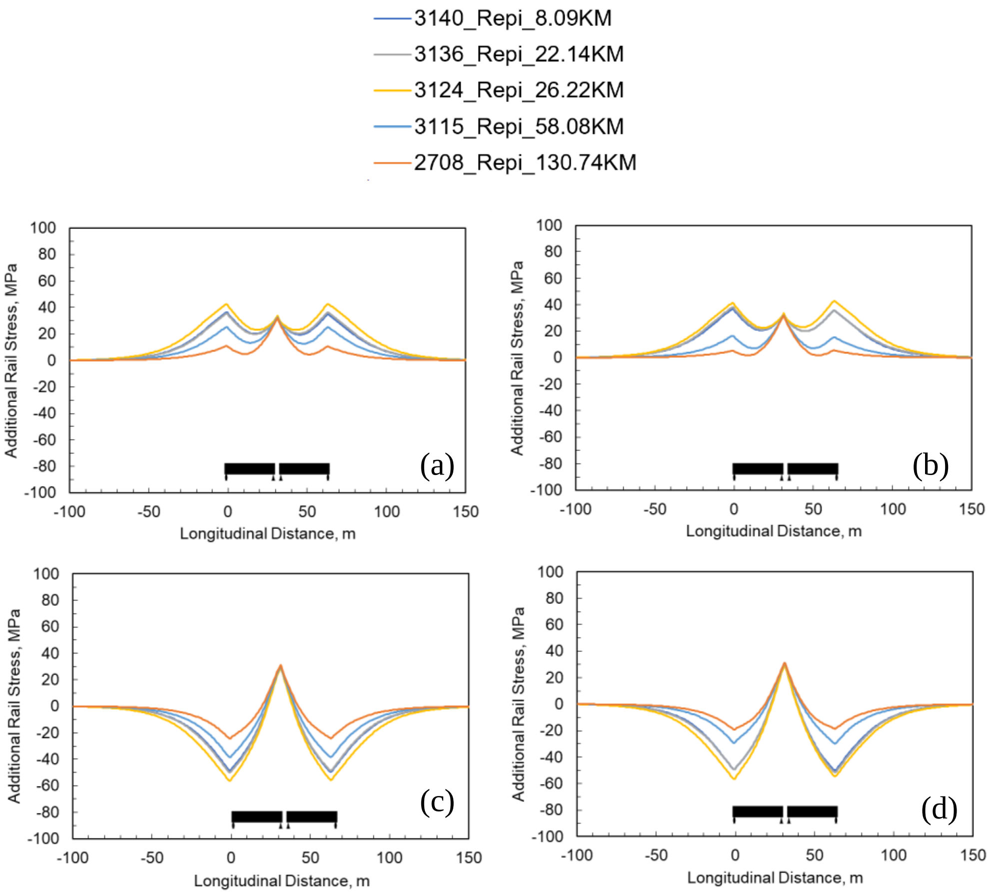

Figure 4.23. ARS results for Yayladağ Hatay Mw=6.4 Earthquake: (a) XH1_YH2 maximum tensile; (b) XH2_YH1 maximum tensile (c) XH1_YH2 maximum compressive; (d) XH2_YH1 maximum compressive

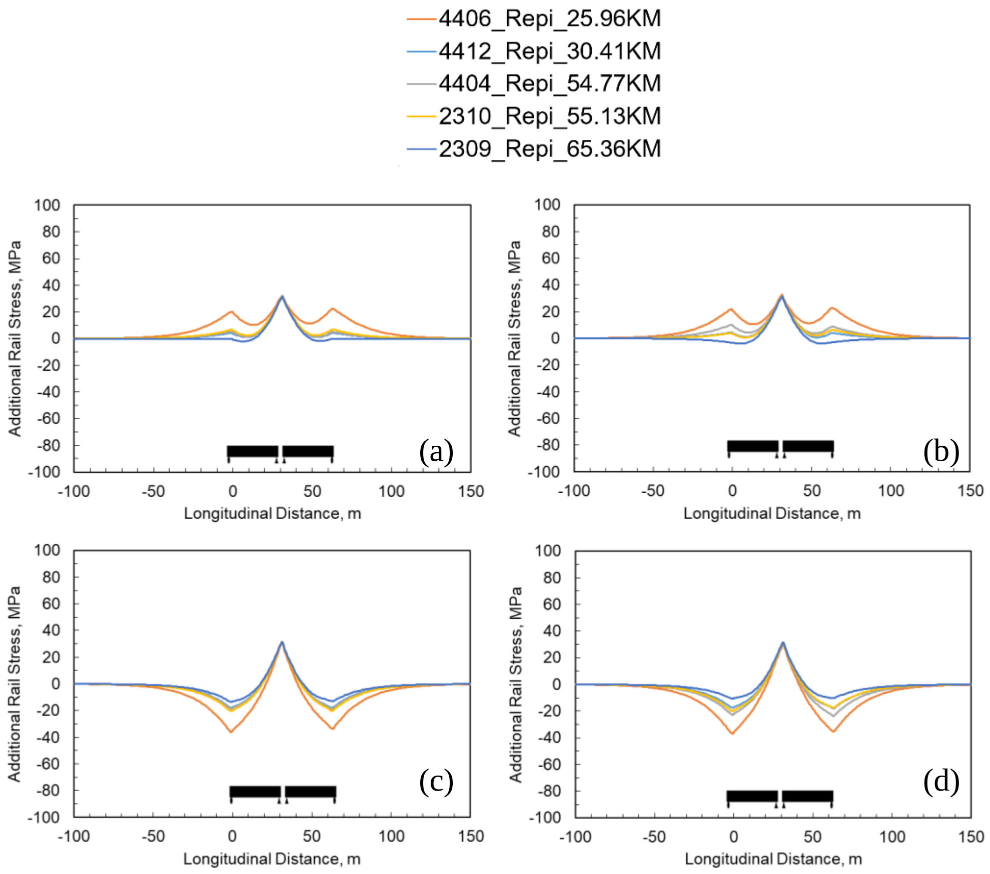

Figure 4.24. ARS results for Yeşilyurt Malatya ML=5.8 Earthquake: (a) XH1_YH2 maximum tensile; (b) XH2_YH1 maximum tensile; (c) XH1_YH2 maximum compressive; (d) XH2_YH1 maximum compressive

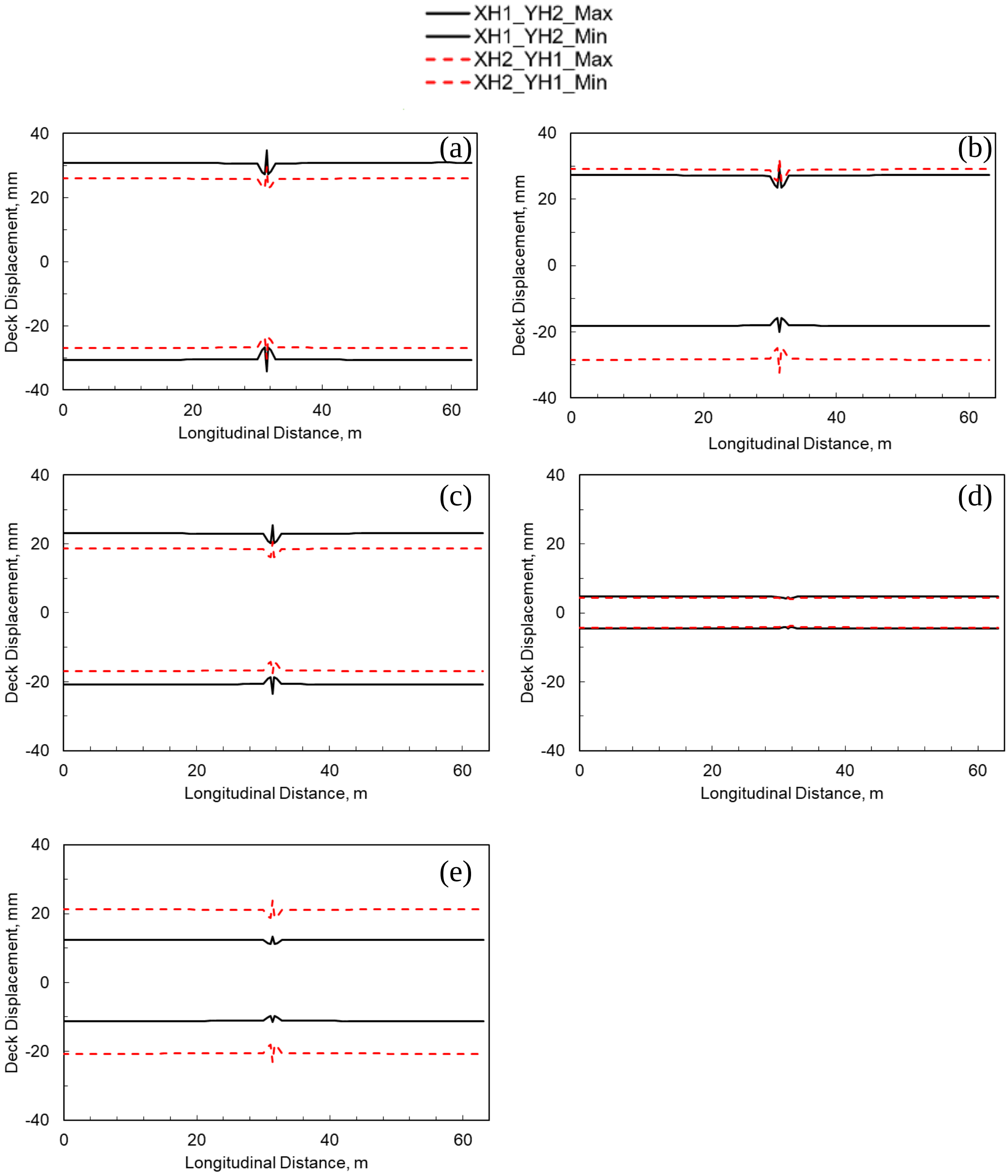

Figure 4.25. Deck displacement results for Pazarcık Kahramanmaraş Mw=7.7 Earthquake: (a) Station 3132; (b) Station 4625; (c) Station 3136 (d) Station 0122; (e) Station 8022 deck displacement

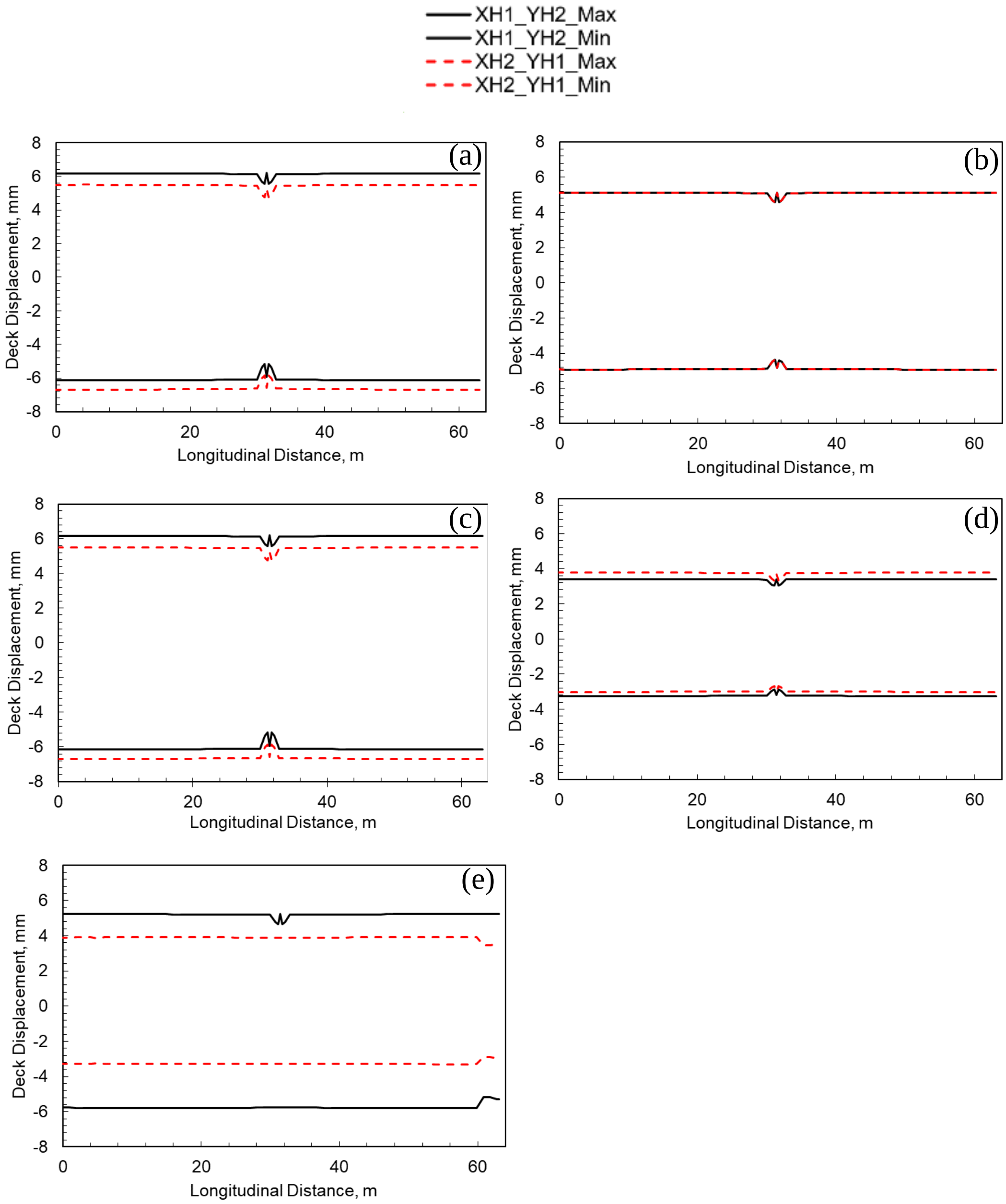

Figure 4.26. Deck displacement results for Elbistan Kahramanmaraş Mw=7.6 Earthquake: (a) Station 4611; (b) Station 0127; (c) Station 4612 (d) Station 4617; (e) Station 4624

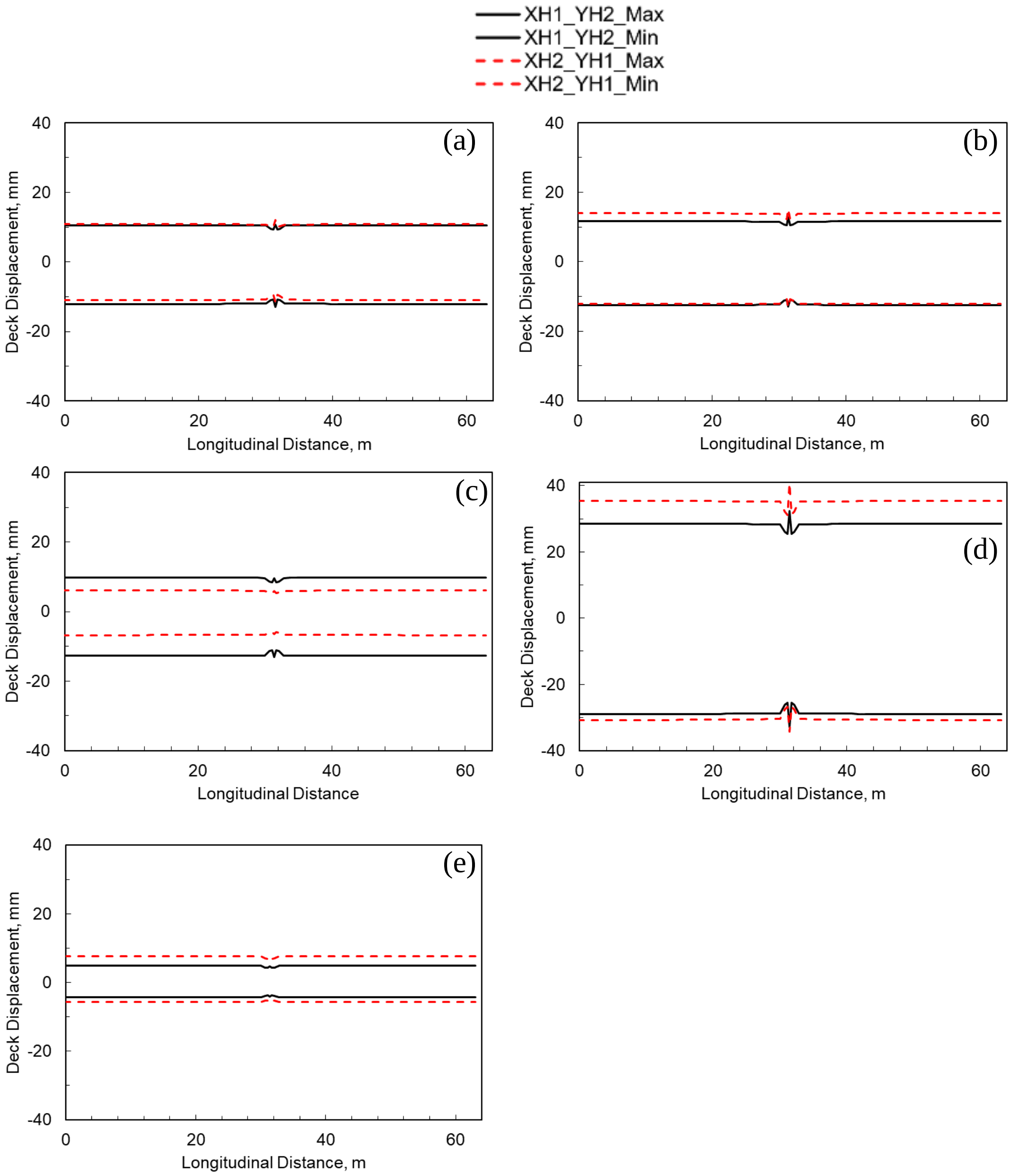

Figure 4.27. Deck displacement results for Nurdağı Gaziantep Mw=6.6 Earthquake: (a) Station 4616; (b) Station 4624; (c) Station 3126; (d) Station 2712; (e) Station 4625

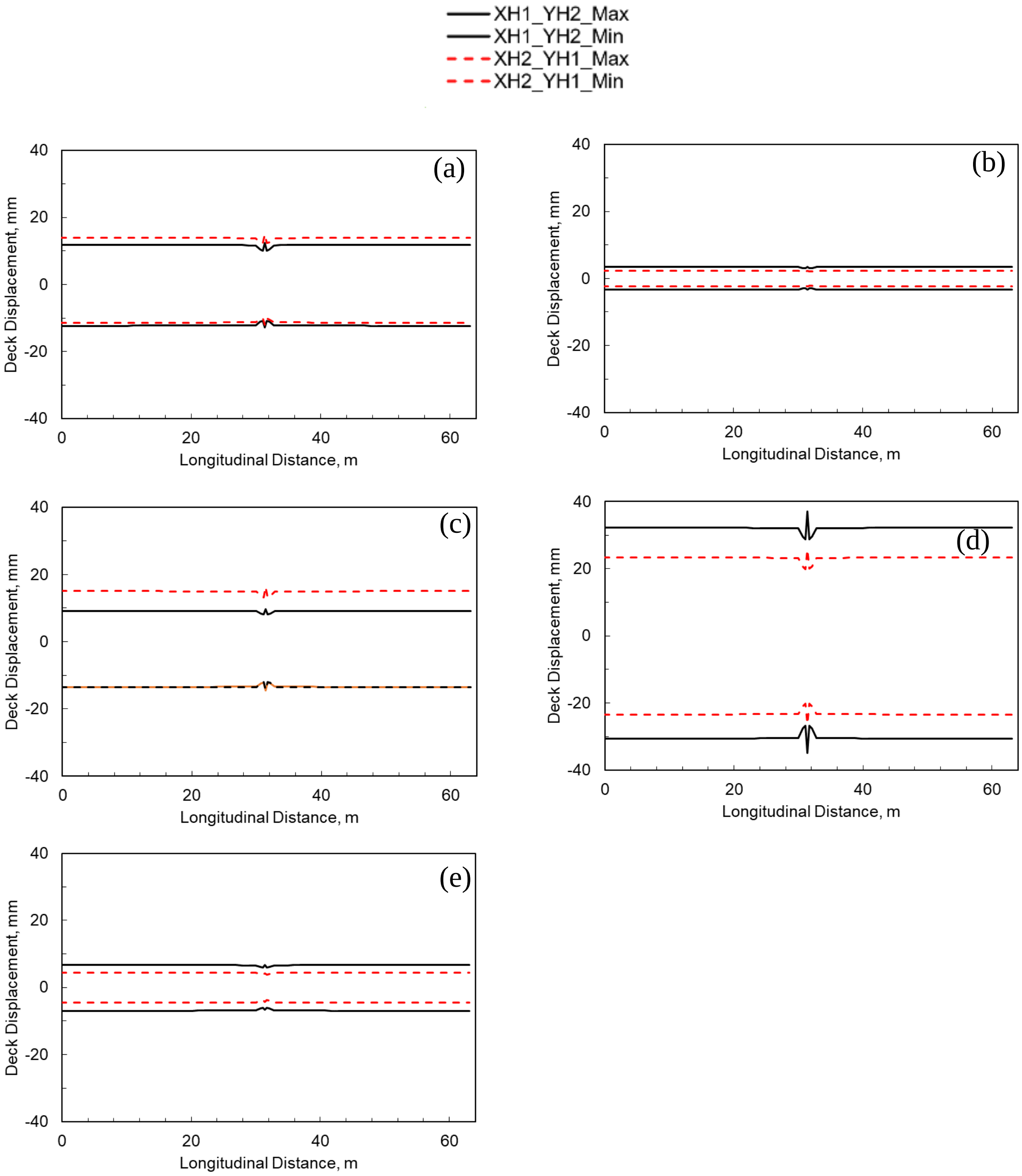

Figure 4.28. Deck displacement results for Yayladağ Hatay Mw=6.4 Earthquake: (a) Station 3140 deck displacement; (b) Station 2708; (c) Station 3136; (d) Station 3124; (e) Station 3115

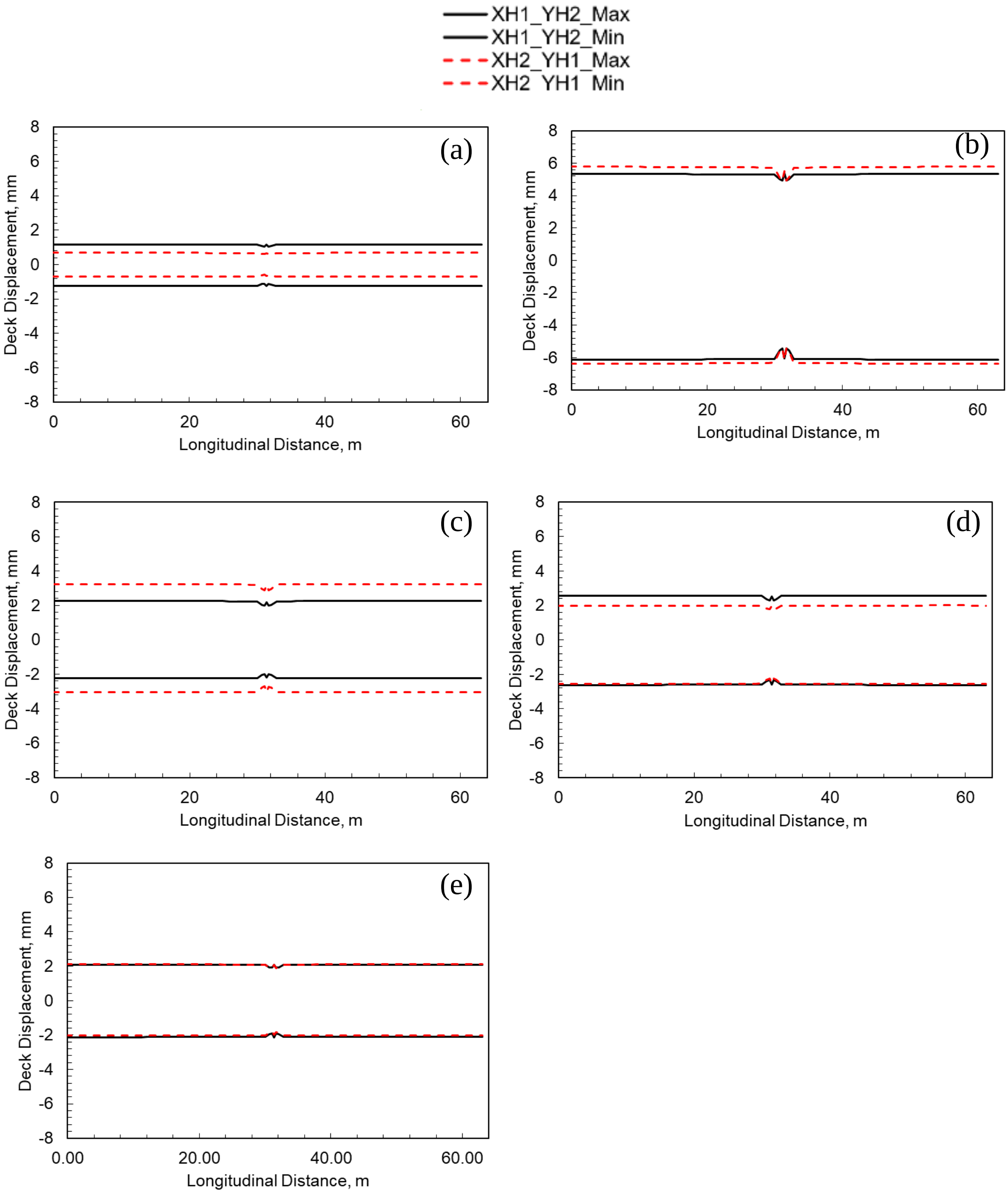

Figure 4.29. Deck displacement results for Yeşilyurt Malatya ML=5.8 Earthquake: (a) Station 2309; (b) Station 4406; (c) Station 4404; (d) Station 2310; (e) Station 4412

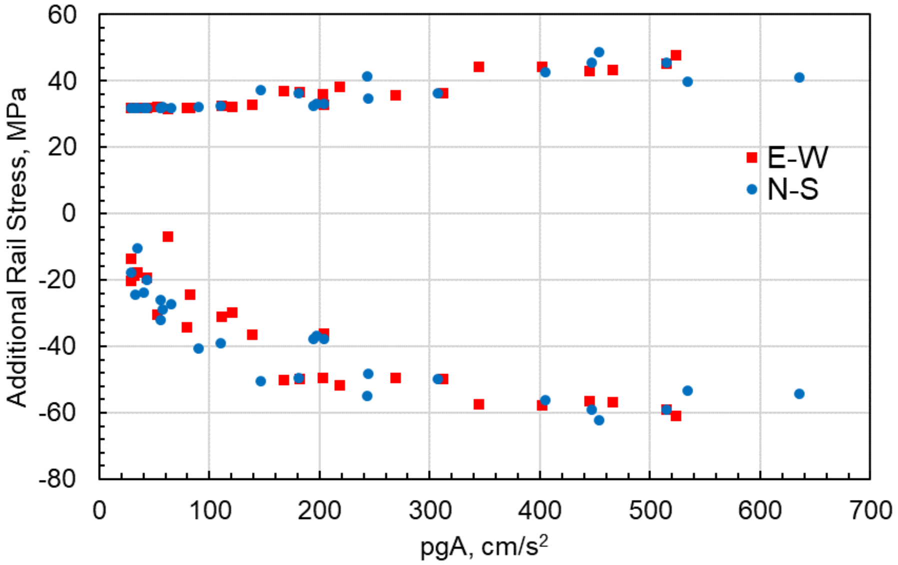

(a)

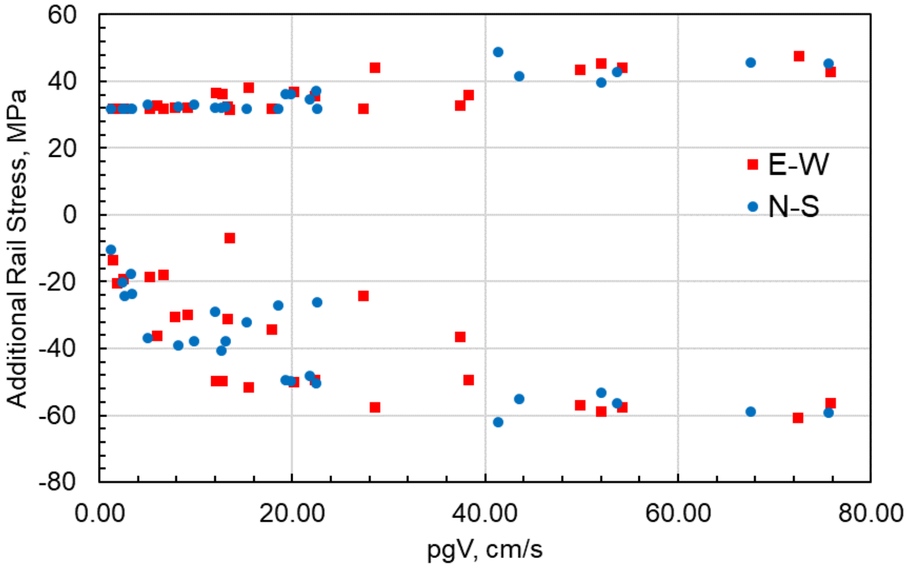

(b)

Figure 4.30. Relation between ARS and seismic intensity parameters: (a) PGA; (b) PGV

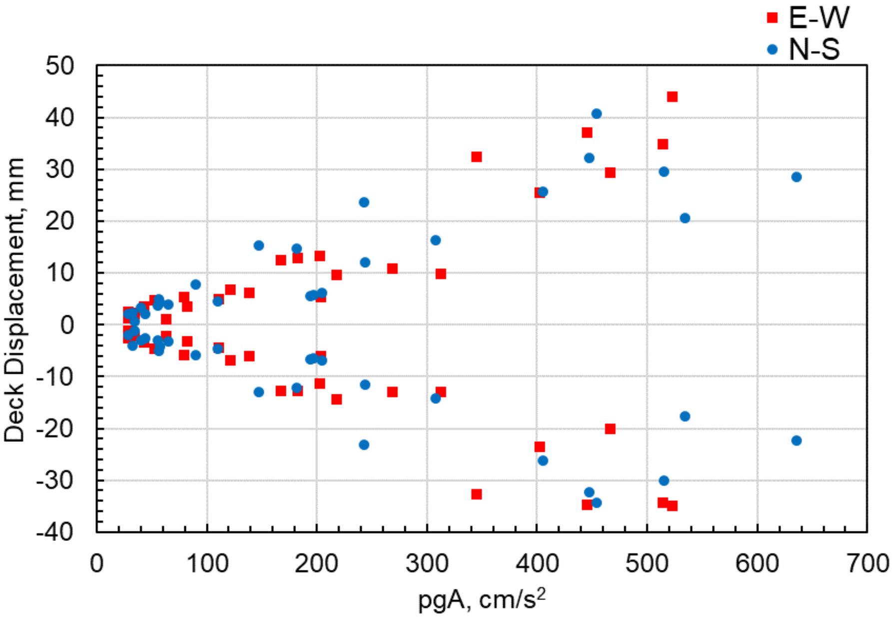

(a)

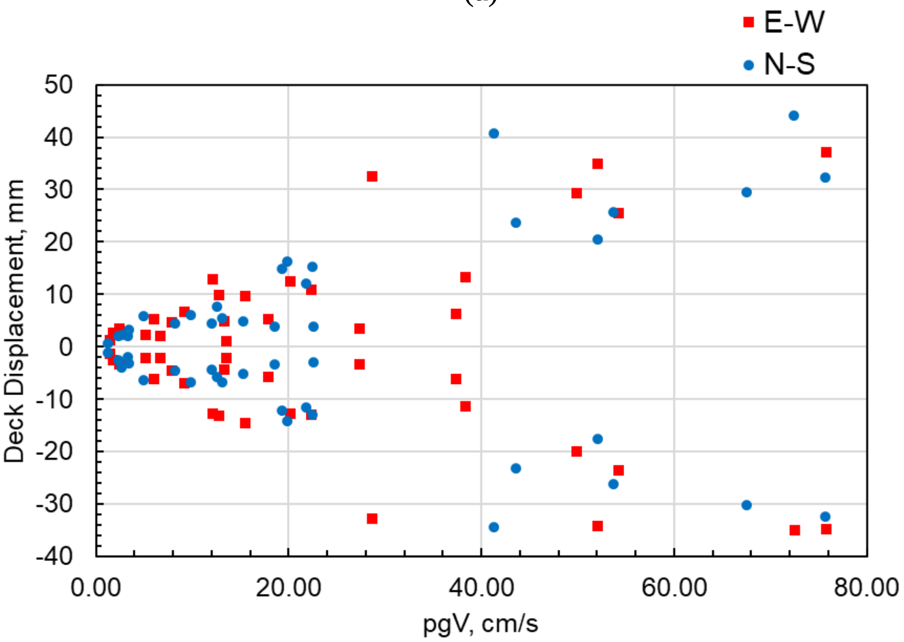

(b)

Figure 4.31. Relation between deck displacements and seismic intensity parameters: (a) PGA; (b) PGV

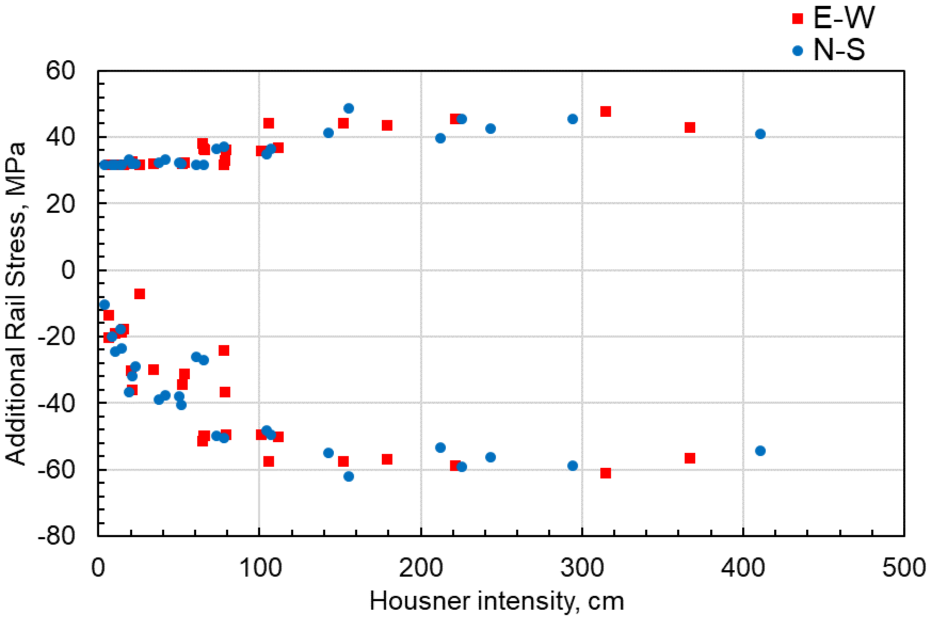

(a)

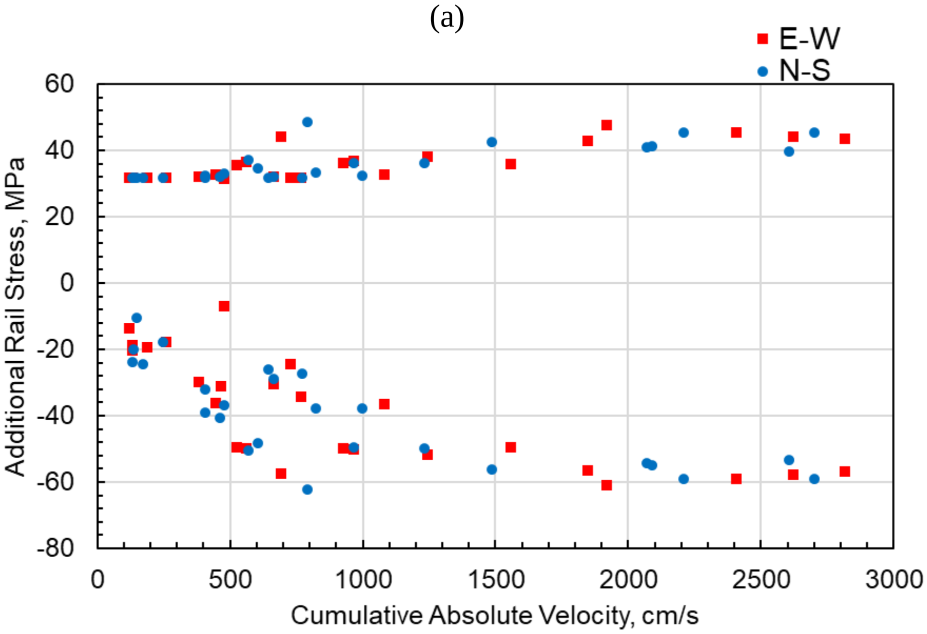

(b)

Figure 4.32. Relation between ARS and seismic intensity parameters: (a) H-I; (b) CAV

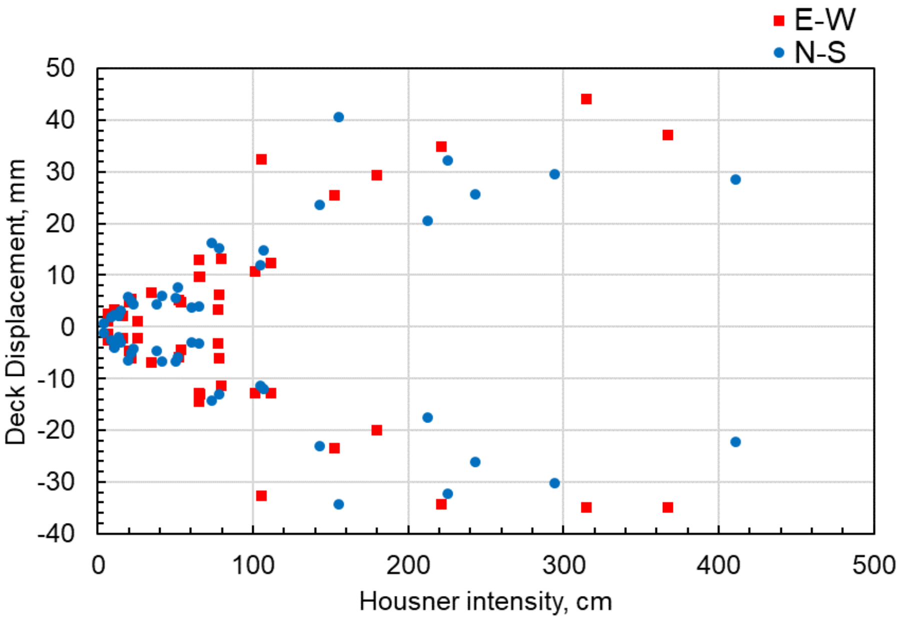

(a)

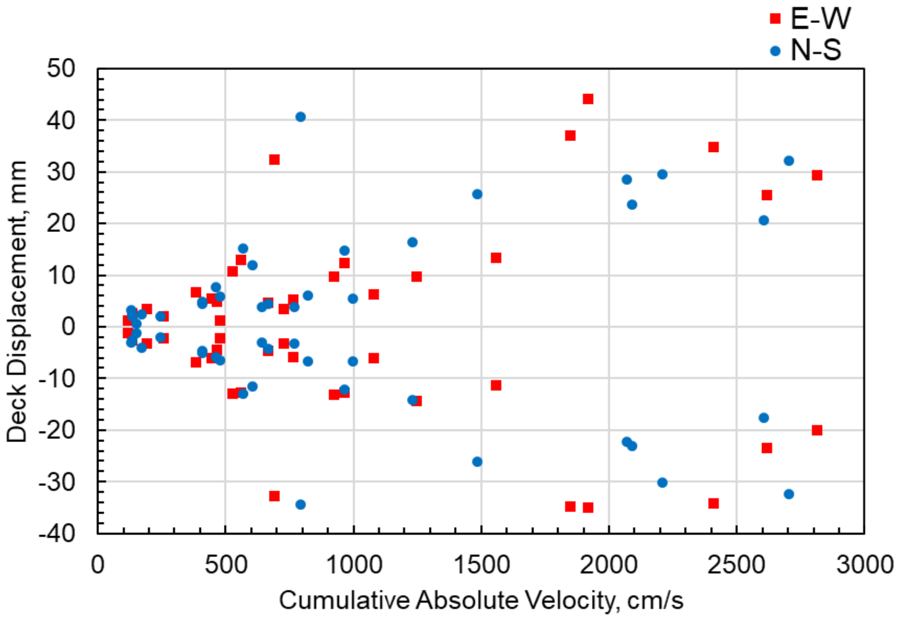

(b)

Figure 4.33. Relation between deck displacements and seismic intensity parameters: (a) H-I; (b) CAV

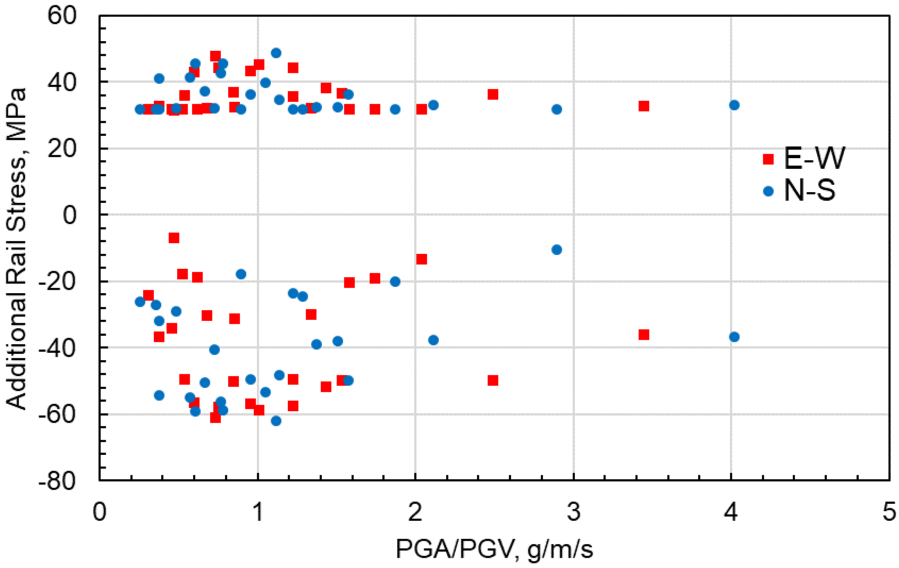

(a)

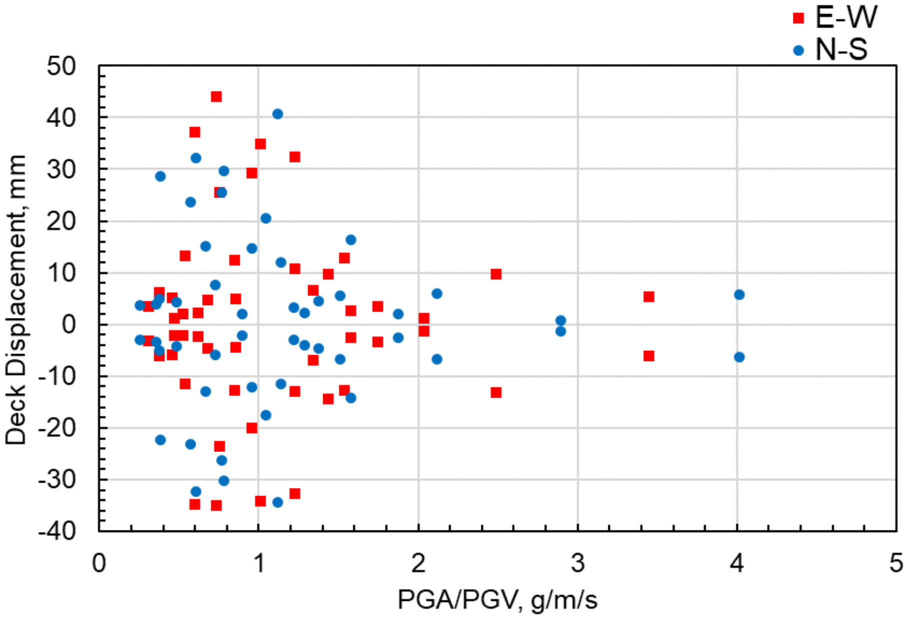

(b)

Figure 4.34. Relation between PGA/PGV ratio: (a) ARSs; (b) deck displacements

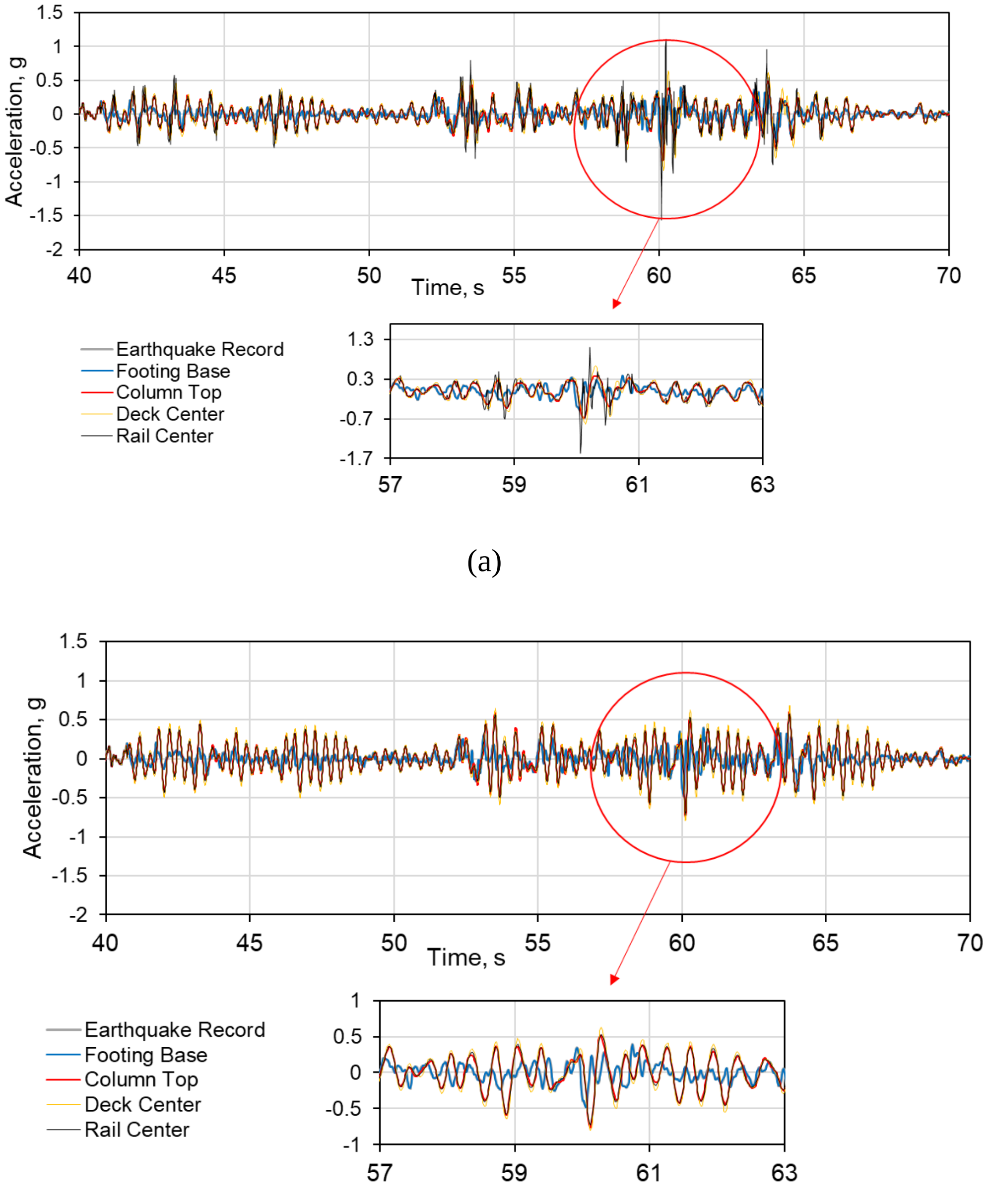

(a)

(b)

Figure 4.35. Pazarcik (Mw=7.7) earthquake Station 4625 ground motion record and acceleration response at different locations for Bridge K9: (a) bilinear RDC; (b) linear elastic RDC

CHAPTER 5

CONCLUSIONS

As part of this thesis, extensive numerical analyses were conducted to gain insights into TBI response through the adjustment of various parameters. Additionally, the exploration extended to investigating TBI response under seismic loads. The study is divided into three major parts and distinct conclusions drawn from each of these parts are presented below.

5.1 Conclusions Regarding Longitudinal TBI Response for Simply Supported Precast Concrete Railway Bridges

A numerical investigation was conducted in order to provide a better understanding of TBI for bridges with CWRs. The numerical modeling approach was verified with available analytical solutions and data obtained from bridge monitoring. The primary interest was to illustrate how sensitive the TBI response is to changes in RDCs with both separate and sequential analysis approaches. The parametric study was extended to investigate the effects of expansion length and substructure stiffness, in addition to RDC type, on the TBI response. The following conclusions are drawn based on the numerical analysis results:

- As the expansion length, (i.e., span length of a simply supported bridge) increases, the contribution of thermal loading in total ARSs increases due to increased cross-sectional area of the bridge. The same conclusion cannot be derived for braking/acceleration and vertical loading, since these forces are applied directly to the rail and to specific limited lengths according to the position of the train.

- Resistance limit in RDCs is reached close to roller support locations under thermal and braking/acceleration loading, whereas RDCs remain in initial linear range under vertical loading. The main reason is the direction of the loading. Relative displacements between track and bridge from vertical loads are not as significant as in the longitudinal loadings. In the case of braking/acceleration loading, RDCs with higher initial stiffness and lower relative yield displacements tend to yield earlier, resulting in lower ARSs where higher longitudinal forces are transferred from track to bridge.

- Highest ARSs are obtained with UIC 774-3R ballastless track RDC. Utilizing the RDCs that were reported based on field or laboratory measurements instead of those specified by design standards may lead to smaller ARSs. Therefore, conducting physical testing on fastening systems to identify more realistic RDCs can be an approach for obtaining longer expansion lengths, and hence more economical designs. In other words, according to the type of rail, sleepers and fastening system on tracks, specific RDCs can be used by bridge designers especially for ballastless systems to avoid exceeding the total ARS limits if the bridge is close to threshold in terms of TBI.

- Substructure stiffness has a crucial effect on the ARSs especially under acceleration/braking loads. Increased substructure stiffness leads to higher ARSs due to thermal and vertical effects, while the ARSs due to braking/acceleration loads decrease. Considering the combined contribution of all load effects, lower substructure stiffness results in higher ARSs in multi-span simply supported bridges. Therefore, as the substructure becomes slenderer, the TBI is more vulnerable to braking/acceleration forces in terms of ARSs. The ARS difference due to braking/acceleration forces was 192% between substructure with lowest stiffness (10 meters height of reinforced concrete piers with 2 meters of diameter) and highest stiffness (idealized pin condition). As substructure stiffness decreases, ARSs due to braking/acceleration forces become significantly high and start to dominate the total ARSs.

- Performing a separate analysis instead of a sequential analysis does not result in an appreciable difference in ARS values for ballasted tracks and for ballastless tracks over bridges with relatively high substructure stiffness. For the case of ballastless track with slender substructure sequential analysis produces approximately 10% smaller ARS compared to separate analysis.

In this study, short to medium span bridges with simply supported precast concrete girders were considered. Consequently, the above conclusions were validated only for this type of bridge and with the static moving load model utilized in analyses. One particular aspect of precast concrete girder bridges is that as the girders are prestressed almost exclusively, the concrete remains in the uncracked state under service loading. This condition validates the use of uncracked cross section properties for girders in analysis. Future analyses may focus on bridges of other types, as well as continuous span bridges with longer span lengths and dynamic train loads. Future analyses may focus on continuous span bridges with longer span lengths and dynamic train loads. TBI response of horizontally curved bridges may also be addressed in future studies.

5.2 Conclusions Regarding Investigation of TBI Response under Seismic Ground Motion

The investigation into track-bridge interaction (TBI) under seismic ground motions for railway bridges has yielded valuable insights into various influencing factors.

The third chapter focused on two designed railway bridges, designated as K8 and K9, located in the eastern part of Türkiye, employing sophisticated numerical analyses and exploring different scenarios. The findings of the study are expected to contribute to the process of enhancing the design and assessment of railway lines for seismic resilience, ensuring operational safety, and contributing to the development of more accurate and effective design guidelines for TBI analysis under seismic loading. The following key conclusions are drawn from the analyses presented in Chapter 3.

- The response of TBI under different ground motion scenarios, varying in earthquake magnitude and distance to fault, emphasizes the significant role of ground motion selection. The analysis demonstrates that even when using the same target spectrum for scaling, distinct ground motion parameters can lead to considerable variations in additional rail stresses (ARSs). This underscores the importance of carefully choosing appropriate ground motions for accurate TBI assessment.

- The presence or absence of intermediate expansion joints at pier locations is a crucial factor influencing TBI response. The inclusion of expansion joints at pier locations consistently results in reduced maximum tensile rail stresses and increased maximum compressive rail stresses at abutment locations.

- The investigation into different pier support modeling methods highlights the adequacy of using fixed boundary conditions at pier bases for TBI analysis. Comparative analysis with soil springs using spread footing foundations indicates minimal differences in rail stress responses. This finding suggests that the fixed support idealization provides sufficiently accurate ARS results for the studied bridges and soil types.

- The study's exploration of unloaded and loaded Rail Displacement Curves (RDCs) sheds light on the sensitivity of TBI response under seismic ground motion to the type of RDC. The use of loaded RDCs leads to significantly higher rail stresses, but has no discernible impact on the distribution of rail stresses along the track. While rail-deck relative displacements exceed the UIC 774-3R (2001) limit under braking/acceleration forces, they remain within the limit set by the Taiwan High-Speed Railway Provision (2000) under seismic loading scaled to the service earthquake.

5.3 Conclusions Regarding TBI Response of A Railway Bridge Subjected to Pazarcık and Elbistan Earthquakes

The following conclusions were obtained from the results of 410 nonlinear time history analyses, involving both scaled and unscaled ground motions concerning TBI:

- The variations in maximum tensile and compressive ARSs followed the trend of spectral acceleration at first period of the bridge structure in terms of scaled set of analysis.

- The maximum ARSs for each event that resulted from the scaled ground motions were limited around 43.0 MPa for compression and 40.8 MPA for tension.

- Considerably low yield displacement capacity of 2 mm in ballasted RDC shifted the focus more on the displacements rather than ARSs in terms of TBI design.

- Maximum tensile and compressive ARSs obtained from the analyses are below the limits specified by Taiwan Code (2000). The main reason for such a behavior is the occurrence of slip between the rail and the bridge structure after a certain lateral force threshold was reached.

- Distance to rupture is an important parameter especially in terms of displacement results. Similar magnitude earthquakes with different distances to rupture result in different TBI response due to the locations of the stations in scaled set of analyses.

- The deck longutinal displacements have a more decisive role than ARSs in terms of TBI design, especially for bridges in earthquake prone regions, when unscaled ground motion scenarios are considered.

- Both PGA and PGV values show similar correlations with deck displacement and ARSs. PGA value of 300 cm/s^2 and PGV value of 40 cm/s were identified as threshold limits for the specific bridge under consideration. Designers are not required to conduct a TBI assessment for ground motions when PGA and PGV values are below the specified threshold limits. In such cases, design provisions solely for thermal and train loads will be adequate for the investigated type railway bridges.

- PGA/PGV ratio values for the selected ground motions fall within the range of 0.8-1.2 g/m/s. Beyond this range, the relative displacements consistently remained below the specified design limitations.

- Yielding of RDCs amplified the maximum accelerations on rails more than two times when compared with nonyielding RDCs.

It is important to acknowledge that these conclusions have been specifically validated for the commonly used type of railway bridge in Türkiye. Extending the numerical modeling approach to other bridge configurations could yield further valuable insights. Moreover, redefining the rail stress limits under thermal and train loadings and introducing new limits for railway bridges in earthquake-prone regions could be considered to enhance the seismic resilience and operational safety of railway lines. Finally, the observed displacement limits and their correlation with PGA and PGV values could potentially be extended to other bridge configurations and variations in substructure stiffness. Utilizing these findings as design parameters could be a useful tool, particularly in the preliminary stages of TBI investigation in earthquake-prone regions.

REFERENCES

AFAD (Afet ve Acil Durum Yönetimi Başkanlığı), Ground Motion Database. AFAD https://tadas.afad.gov.tr/list-event

AFAD (Afet ve Acil Durum Yönetimi Başkanlığı), (2018). Türkiye Deprem Tehlike Haritası. https://www.afad.gov.tr/turkiye-deprem-tehlike-haritasi

Alijani, A., Kh. Abadi, M., & Ghyasvand, S. (2022). Numerical and experimental analysis of intact and cracked railway bridges. Structures, 38, 1018–1030.

American Society of Civil Engineers, 2016. ASCE/SEI 7-16: Minimum Design Loads for Buildings and Other Structures.

American Society of Civil Engineers, 2017. ASCE/SEI 41-17: Seismic Evaluation and Retrofit of Existing Buildings.

Aviram, A., Mackie, K. R. & Stojadinovic, B. (2008). Guidelines for Nonlinear Analysis of Bridge Structures in California. Pacific Earthquake Engineering Research Center, University of California, Berkeley.

BSSC (2003) NEHRP Recommended Provisions for seismic Regulations for New buildings and other Structures, Part1: Provisions, FEMA 368, Federal Emergency Management Agency, Washington, D.C.

Cetin, K. O., Ilgac, M., Can, G., & Cakir, E. (Eds.). (2023). (rep.). Preliminary Reconnaissance Report on February 6, 2023, Pazarcık Mw=7.7 and Elbistan Mw=7.6, Kahramanmaraş-Türkiye Earthquakes. Ankara, Türkiye: METU Earthquake Engineering Research Center.

Chellini G., Nardini L., & Salvatore W. (2011). Dynamical identification and modelling of steel-concrete composite high-speed railway bridges. Structure and Infrastructure Engineering, 7:11, 823-841.

Chen, R., Wang, P., & Wei, X. (2013). Track-Bridge Longitudinal Interaction of Continuous Welded Rails on Arch Bridge. Mathematical Problems in Engineering, 2013(1-8).

Cheng Y.S., Au F.T.K, & Cheung Y.K. (2001). Vibration of railway bridges under a moving train by using bridge-track-vehicle element. Engineering Structures, 23, 1597-1606.

Chinese national standards, TB 10015-2012. Code for design of railway continuous welded rail, Beijing; 2012.

Chopra, A. K. (1995). Dynamics of Structures: Theory and Applications to Earthquake Engineering. Earthquake Engineering and Structural Dynamics, 24 (1173).

Dai, G., Chen, G., Zheng, R., & Chen, Y. F. (2020). A new bilinear resistance algorithm to analyze the track-bridge interaction on long-span steel bridge under thermal action. Journal of Bridge Engineering, 25(2), 04019138.

Dai, G., Su, M., & Chen, Y. F. (2016). Design and construction of simple beam bridges for high-speed rails in China: Standardization and industrialization. The Baltic Journal of Road and Bridge Engineering, 11(4), 274–282. https://doi.org/10.3846/bjrbe.2016.32

Davis S.G. (2009). Controlling track-structure interaction in seismic conditions. In R. Calçada, R. Delgado, A.C. Matos, Goicocela J.M. (Ed.), Track Bridge Interaction on High-speed Railways (pp.29-35). London: Taylor & Francis.

Dicleli, M., Albhaisi, S., Mansour, M. Y. (2005). Static soil–structure interaction effects in seismic-isolated bridges. Practice Periodical on Structural Design and Construction, 10(1), 22–33. doi: 10.1061/(asce)1084-0680(2005)10:1(22)

DIN, DIN-Fachbericht 101. Einkwirkungen auf Brücken, Berlin; 2003.

Dobry R, Gazetas G. (1986). Dynamic response of arbitrary shaped foundations. ASCE Journal of Geotechnical and Geoenvironmental Engineering, 112(2), 109–35.

Elhout, E. A. (2020). The correlation between the ground motion intensity measure parameters of earthquakes. Asian Journal of Civil Engineering, 21(5), 829–840. https://doi.org/10.1007/s42107-020-00243-1

Enshaeian, A., & Rizzo, P. (2021). Stability of continuous welded rails: A state-of-the-art review of structural modeling and nondestructive evaluation. Proceedings of the Institution of Mechanical Engineers, Part F: Journal of Rail and Rapid Transit, 235(10), 1291–1311.

Eroglu, M., Koc, M. A., Esen, I., Kozan, R. (2023). Realistic modelling for analysis of train-structure and ballasted-track interaction for high-speed trains. Journal of Vibration Engineering & Technologies. doi.org/10.1007/s42417-023-01029-w

European Rail Research Institute ERRI D202/RP12: ‘Final report’, Utrecht: European Rail Research Institute, December 1997.

European Committee for Standardization (CEN), EN 13674-1. Railway applications – Track – Rail Part 1: Vignole railway rails 46 kg/m and above, Brussells; 2002.

European Committee for Standardization (CEN), EN 1991-2. Eurocode 1: Actions on structures. Traffic loads on bridges (Part 2), Brussels; 2003.

European Committee for Standardization (CEN), EN 1998-1. Eurocode 8: Design of structures for earthquake resistance - Part 1: General rules, seismic actions and rules for buildings, Brussels; 2004.

European Committee for Standardization (CEN), EN 1998-2. Eurocode 8: Design of structures for earthquake resistance - Part 2: Bridges, Brussels; 2005.

Frýba L. Dynamics of railway bridges, London : 1996.

Galvín P., Romero A., Moliner E., & Martínez-Rodrigo M.D. (2018). Two FE models to analyse the dynamic response of short span simply-supported oblique high-speed railway bridges: Comparison and experimental validation. Engineering Structures, 167, 48-64.

Guo W.W., Xia H., Roeck G.D., & Liu K. (2012). Integral model for train-track-bridge interaction on the Sesia viaduct: Dynamic simulation and critical assessment. Computers and Structures, 112-113, 205-216.

Hu, Z., Wei, B., Jiang, L., Li, S., & Min, H. (2022a). Track structural damage index for high-speed railway girder bridges considering residual deformations due to earthquake. Bulletin of Earthquake Engineering, 20(12), 6587–6609. https://doi.org/10.1007/s10518-022-01448-2

Hu, Z., Wei, B., Jiang, L., Li, S., Yu, Y., & Xiao, C. (2022b). Assessment of optimal ground motion intensity measure for high-speed railway girder bridge (HRGB) based on spectral acceleration. Engineering Structures, 252, 113728. https://doi.org/10.1016/j.engstruct.2021.113728

Huang, Y., Wang, J., Le, W., Zhang, L., & Su, J. (2021). Study on mechanical behaviours of rail fasteners and effects on seismic performance of Urban Rail Viaduct. Structures, 33, 3822–3834.

Jin, Z., Liu, W., Pei, S. (2022). Probabilistic evaluation of railway vehicle’s safety on bridges under random earthquake and track irregularity excitations. Engineering Structures, 266, 114527.

Kang, C., Schneider, S., Wenner, M., Marx, S. (2018). Development of design and construction of high-speed railway bridges in Germany. Engineering Structures, 163, 184-194.

Kang C., Wenner M., Marx S. (2021). Background investigation on the permissible additional stresses due to track/bridge interaction. Engineering Structures, 228, 111505.

Karoumi R., Wiberg J., & Liljencrantz A. (2005). Monitoring traffic loads and dynamic effects using an instrumented railway bridge. Engineering Structures, 27, 1813-1819.

Kašpárek, J., Ryjáček, P., Rotter, T., Polák, M., & Calçada, R. (2020). Long-term monitoring of the track–bridge interaction on an extremely skew steel arch bridge. Journal of Civil Structural Health Monitoring, 10, 377-387.

Kim H.B., Lee J., & Lee D.H. (2010). Extracting modal parameters of high-speed railway bridge using the TDD technique. Mechanical Systems and Signal Processing, 24, 707-720.

Kim, C. W., Kawatani, M., Kanbara, T., & Nishimura, N. (2013). Seismic behavior of steel monorail bridges under train load during strong earthquakes. Journal of Earthquake and Tsunami, 07(02), 1350006. https://doi.org/10.1142/s1793431113500061

KMG Proje, 2020. Kars-Iğdır-Aralık-Dilucu Demiryolu Bağlantısı Revize Etüt Proje ve Mühendislik Hizmetleri İşi, KM:180+311.478-KM:180+374.278 arası K9 Köprüsü Hesap Raporu (in Turkish).

Kohl, A. M., Clement, K. D., Schneider, J., Firus, A., Lombaert, G. (2023). An investigation of dynamic vehicle-bridge interaction effects based on a comprehensive set of trains and bridges. Engineering Structures, 279, 115555.

Korea Rail Network Authority. KR C08080: track-bridge longitudinal interaction analysis (in Korean), 2014.

Kwark J.W., Choi E.S., Kim Y.J., Kim B.S., & Kim S.I. (2004). Dynamic behavior of two-span continuous concrete bridges under moving high-speed train. Computers and Structures, 82, 463-474.

Li, S., Wei, B., Tan, H., Li, C., & Zhao, X. (2021). Equivalence of friction and viscous damping in a spring-friction system with concave friction distribution. Journal of Testing and Evaluation, 49(1), 20190885.

Liu K., Reynders E., De Roeck G., & Lombaert G. (2009). Experimental and numerical analysis of a composite bridge for high-speed trains. Journal of Sound and Vibration, 320, 201-220.

Liu, W., Lai, H., Dai, G., Rao, S., Wang, D., & Wu, B. (2021). Numerical Study on Track–Bridge Interaction of Integral Railway Rigid-Frame Bridge. Applied Sciences, 11(3), 922.

MIDAS Information Technology Co., Ltd. (2012). Analysis Reference Manual, MIDAS Civil.

MIDAS User Website Rail Structure Interaction. [Online]. Available: https://resource.midasuser.com/en/solution/rail-structure-interaction/. [Accessed: 01-Dec-2023].

Ministry of Transport and Infrastructure. Turkish Seismic Bridge Design Code, Ankara; 2020.

Mirković N.B., Popović J.P., Pustovgar A.P., Lazarević L.M., & Zhuravlev A.V. (2018). Management of stresses in the rails on railway bridges. FME Transactions, 46, 636-643.

Mirza, O., Kaewunruen, S., Dinh, C., & Pervanic, E. (2016). Numerical investigation into thermal load responses of railway transom bridge. Engineering Failure Analysis, 60, 280–295.

Pacific Earthquake Engineering Research Center, PEER Ground Motion Database. https://ngawest2.berkeley.edu/, [last visited on March 2023].

Pacific Earthquake Engineering Research Center, PEER (2008). Guidelines.

Peixer, M. A., Montenegro, P. A., Carvalho, H., Ribeiro, D., Bittencourt, T. N. (2021). Running safety evaluation of a train moving over a high-speed railway viaduct under different track conditions. Engineering Failure Analysis, 121, 105133.

Petrangeli, M., Tamagno, C., & Tortolini, P. (2008). Numerical analysis of track: Structure interaction and time domain resonance. Proceedings Of The Institution Of Mechanical Engineers, Part F: Journal Of Rail And Rapid Transit, 222(4), 345-353. doi: 10.1243/09544097jrrt168

Ramos, Ó., Schanack, F., Carreras, G., & de Vena Retuerto, J. (2019). Bridge length limits due to track-structure interaction in continuous girder prestressed concrete bridges. Engineering Structures, 196, 109310.

Rocha J.M., Henriques A.A., & Calçada R. (2012). Safety assessment of a short span railway bridge for high-speed traffic using simulation techniques. Engineering Structures, 40, 141-154.

Ruge, P., & Birk, C. (2007). Longitudinal forces in continuously welded rails on bridge decks due to nonlinear track–bridge interaction. Computers & Structures, 85(7-8), 458-475.

Ryjáček, P., & Vokáč, M. (2014). Long-term monitoring of steel railway bridge interaction with continuous welded rail. Journal of Constructional Steel Research, 99, 176-186.

Sanguino, M.C., Requejo, P.G. (2009). Numerical methods for the analysis of longitudinal interaction between track and structure. In R. Calçada, R. Delgado, A.C. Matos, Goicocela J.M. (Ed.), Track Bridge Interaction on High-speed Railways (pp.95-108). London: Taylor & Francis.

Song M.K., Noh H.C., & Choi C.K. (2003). A new three-dimensional finite element analysis model of high-speed train-bridge interactions. Engineering Structures, 25, 1611-1626.

Stokes G.G. (1867). Discussion of a differential equation related to the breaking of railway bridges. Transactions of the Cambridge Philosophical Society, 8(5), 707-735.

Strauss, A., Karimi, S., Šomodíková, M., Lehký, D., Novák, D., Frangopol, D. M., & Bergmeister, K. (2018). Monitoring based nonlinear system modeling of bridge–continuous welded rail interaction. Engineering Structures, 155, 25–35.

Su, M., Dai, G., Marx, S., Liu, W., & Zhang, S. (2018). A brief review of developments and challenges for high-speed rail bridges in China and Germany. Structural Engineering International, 29(1), 160–166. https://doi.org/10.1080/10168664.2018.1456892

Sung D., & Chang S. (2019). Nonlinear behavior of rail fastening system on slab track at railway bridge ends: FEA and experimental study. Engineering Structures, 195, 84-96.

Taiwan High Seep Rail Corporation. Design Specifications, Contract Issue; 2001.

Tso, W. K., Zhu, T. J., & Heidebrecht, A. C. (1992). Engineering implication of Ground Motion A/V ratio. Soil Dynamics and Earthquake Engineering, 11(3), 133–144. https://doi.org/10.1016/0267-7261(92)90027-b

Tzepushelov A., & Troyitzky L. (1974). Design, laying, maintenance and repair of continuously welded rails on the USSR railways. Rail International, 589-605.

Union Internationale des Chemins de fer (UIC), 774-3R Track/bridge interaction. Recommendations for calculations, Paris; 2001.

UIC. (2023, February). High-speed around the world - international union of railways. UIC High Speed. https://uic.org/IMG/pdf/uic-high-speed-around-the_world.pdf

Wang, Z., Jiang, L., Jiang, L., Zhou, W., Du, Y. (2022). Seismic response of high-speed railway simple-supported girder track-bridge system considering spatial effect at near-fault region. Soil Dynamics and Earthquake Engineering, 158, 107283.

Wenner, M., Meier, T., Wedel, F., Schacht, G., & Marx, S. (2019). Experimental determination of the longitudinal pier stiffness of a long railway viaduct. Frontiers in Built Environment, 5.

Widarda, D. R. Longitudinal forces in continuously welded rails due to nonlinear track-bridge interaction for loading sequences, PhD thesis, Dresden Technical University, Dresden; 2009.

Yan, B., Dai, G., & Zhang, H. (2012). Beam-track interaction of high-speed railway bridge with ballast track. Journal of Central South University, 19(5), 1447-1453.

Yang, S. C., & Jang, S. Y. (2016). Track–Bridge interaction analysis using interface elements adaptive to various loading cases. Journal of Bridge Engineering, 21(9), 04016056.

Yun, K.-M., Bae, H.-U., Moon, J., Kim, J.-J., Park, J.-C., & Lim, N.-H. (2019). Quantification of ballasted track-bridge interaction behavior due to the temperature variation through field measurements. NDT & E International, 103, 84–97.

Zhang, J., Wu, D., & Li, Q. (2015). Loading-history-based track–bridge interaction analysis with experimental fastener resistance. Engineering Structures, 83, 62–73.

Zhang, Y., Jiang, L., Zhou, W., Feng, Y., Tan, Z., Chai, X. (2020). Study of bridge-subgrade longitudinal constraint range for high-speed railway simply-supported beam bridge with CRTSII ballastless track under earthquake excitation. Construction and Building Materials, 241, 118026.

Zeng, Z., Tian, C., Tu, Q., Shuaibu, A. A., Wang, W. (2019). Experimental study on the longitudinal resistance of WJ-8 fasteners subjected to torque and vertical loading in continuously welded rails. Proceedings of the Institution of Mechanical Engineers, Part F: Journal of Rail and Rapid Transit, 234(10), 1071–1080. https://doi.org/10.1177/0954409719880667

APPENDICES

A. Supplementary Analysis Results

In addition to those reported in the main body of the thesis, supplementary analyses were conducted in order to either validate the implementation of finite element methods or to shorten the duration of numerical analysis using efficient element length.

Additional verification was done for a 60 m single span concrete box girder bridge using separate and sequential analyses. The study conducted by Yang and Jang (2016) provides detailed geometric and material information regarding this bridge. Figure A.1 presents the ARS distribution for various load cases, including thermal, braking, and vertical train loads, along with the total distribution. As illustrated, the ARS results for each specific load and the total from separate and sequential analyses are agreed well with the results presented in Yang and Jang's study.

Moreover, apart from verification with a simply supported bridge, the models were also validated for a continuous bridge with varying pier heights, span lengths, and two distinct superstructure types within the same bridge. Likewise the simply supported bridge, the geometric and material data sourced from Yang and Jang's study (2016) was utilized. Figure A.2 illustrates the alignment of ARS results with the provided values, further confirming the accuracy of the models employed.

Before conducting analyses, a comprehensive verification process was undertaken using different element lengths. This verification relied on the simply supported bridge example detailed in Yang and Jang's (2016) study. Following a thorough comparison of various element lengths as depicted in Figure A.3, the decision was made to maintain a consistent 1.0 m element length across all analyses, except for particular areas need specific element sizing such as expansion joints. For all of the TBI models utilized in this study, 1.0 m length elements were employed for tracks and the bridge.

For verification models used in Chapter 2, embankment length was initially modelled as 300 m long on each side of a 25 m simply-supported bridge,. However, it became essential to shorten this length due to the presence of nonlinear RDC properties within the embankment. In order to optimize the duration of the nonlinear time history analyses used in Chapters 3 and 4, a series of analyses were performed, employing varying embankment lengths of 5, 10, 25, 50, 100, 300, 400, and 500 m on each side of the bridge. The analysis models were conducted under thermal loading conditions, employing identical geometric and material properties as those utilized in the parametric study on span length detailed in Chapter 2. Variation of maximum tensile and compressive ARSs with the embankment length are presented in Figure A.4. According to the figure, it is evident that an embankment length of 100 m is sufficient without compromising the accuracy of the maximum ARSs. Analysis was repeated to assess the influence of span length on the embankment length provided on both sides of the bridge model. The resulting ARSs under thermal loads for the bridge with 50 m simply-supported span was repeated as illustrated in Figure A.5. For this scenario as well, employing an embankment length of 100 m remains a valid approach to ensure the accuracy of the obtained results.

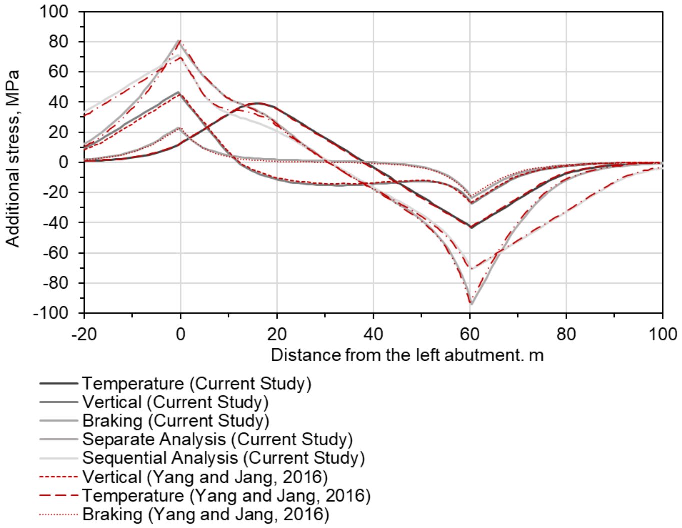

Figure A.1. Verification of ARS with simply supported model provided by Yang and Jang (2016)

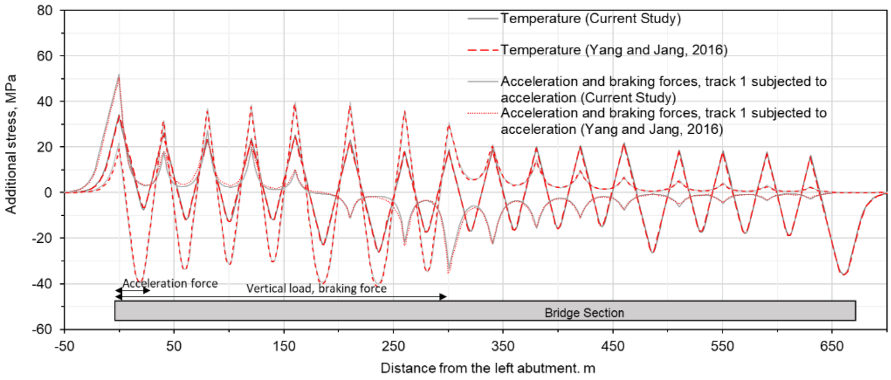

Figure A.2. Verification of ARS with continuous bridge model provided by Yang and Jang (2016)

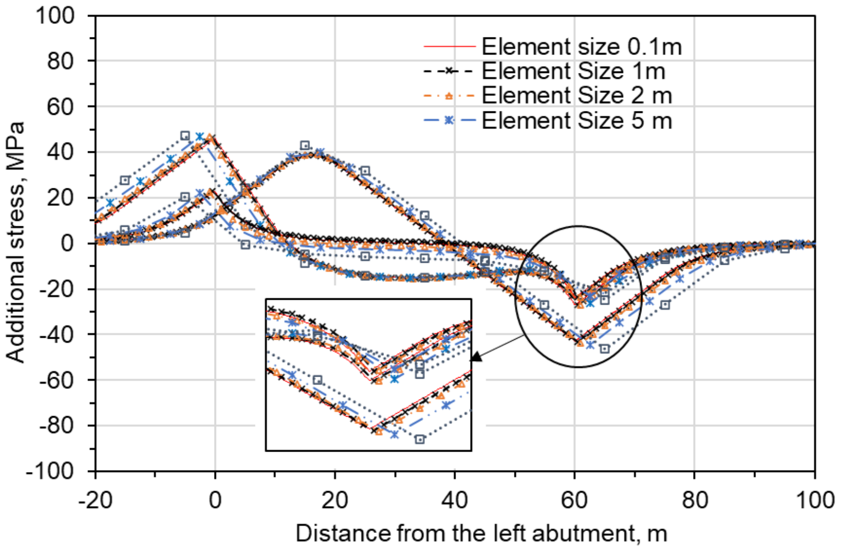

Figure A.3. Element size based on generic TBI model provided by Yang and Jang (2016)

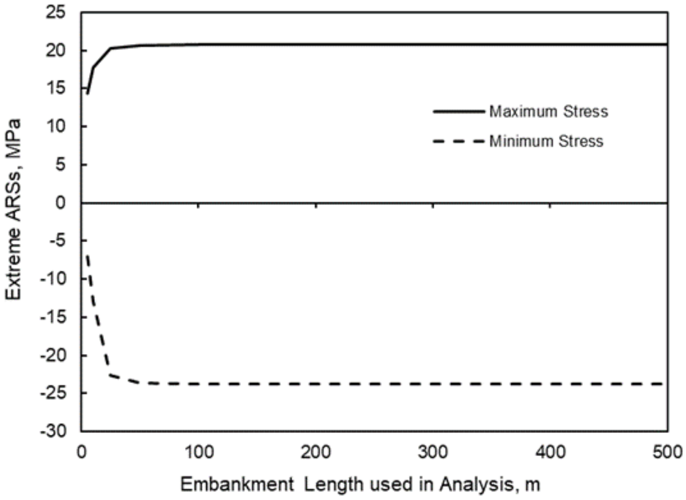

Figure A.4. ARS vs. embankment length (25 m span length)

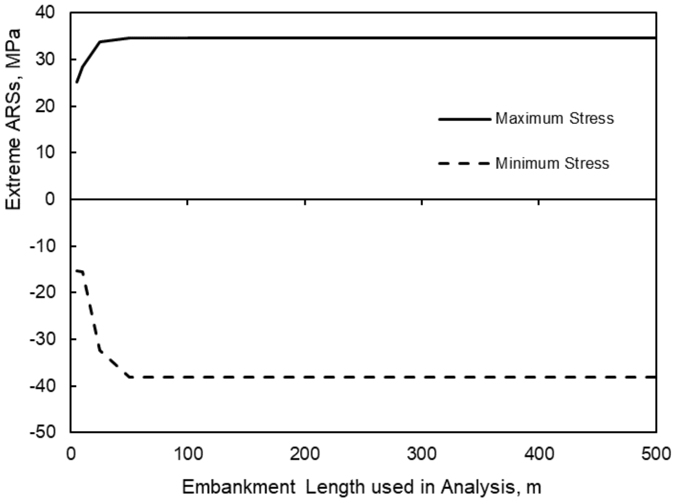

Figure A.5. ARS vs. embankment length (50 m span length)

B. Acceleration Spectra for Ground Motion Records used in Analyses

The unscaled and scaled spectra for the events are provided below.

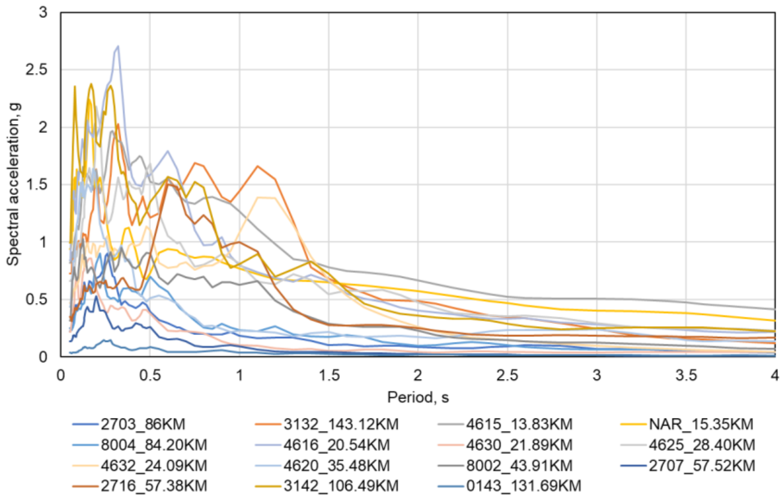

Figure B.1. Unscaled spectra of selected ground motions for Pazarcık Kahramanmaraş Mw = 7.7 Earthquake

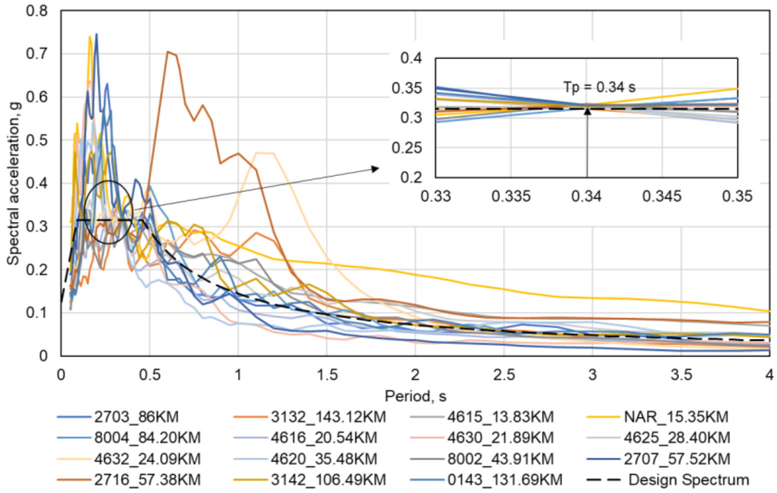

Figure B.2. Scaled Spectra of selected ground motions for Pazarcık Kahramanmaraş Mw = 7.7 Earthquake

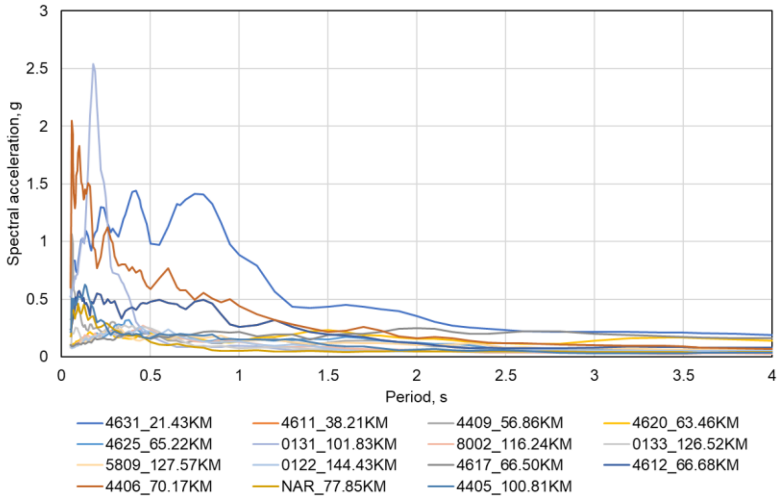

Figure B.3. Unscaled spectra of selected ground motions for Elbistan Kahramanmaraş Mw = 7.6 Earthquake

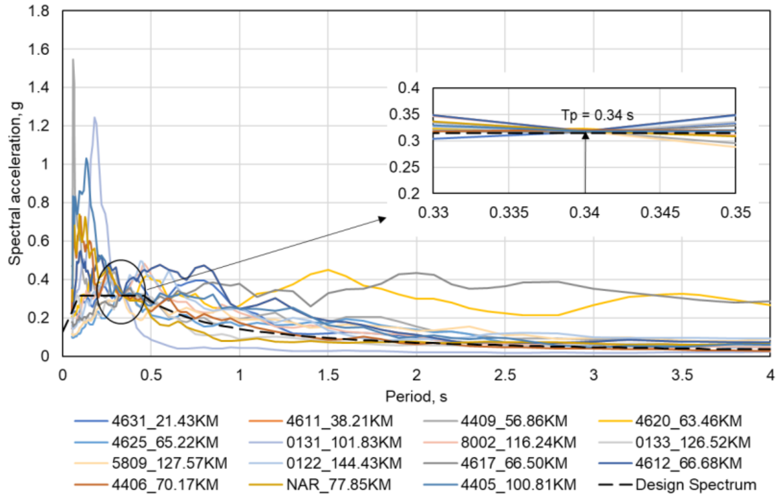

Figure B.4. Scaled spectra of selected ground motions for Elbistan Kahramanmaraş Mw = 7.6 Earthquake

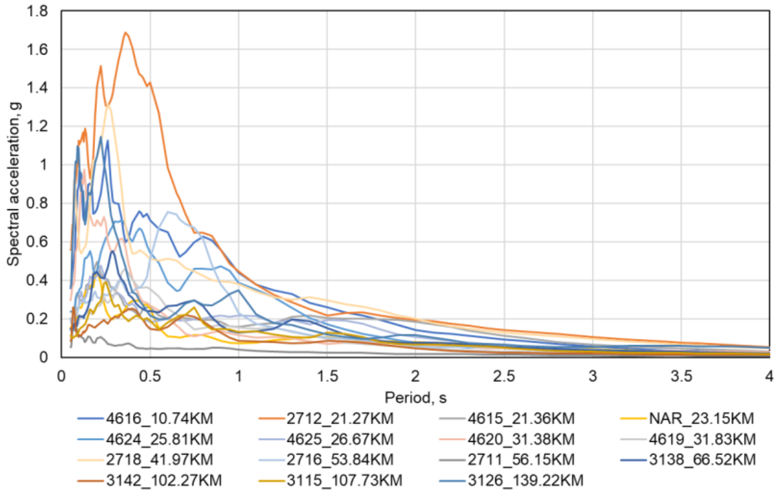

Figure B.5. Unscaled spectra of selected ground motions for Nurdağı Gaziantep Mw = 6.6 Earthquake

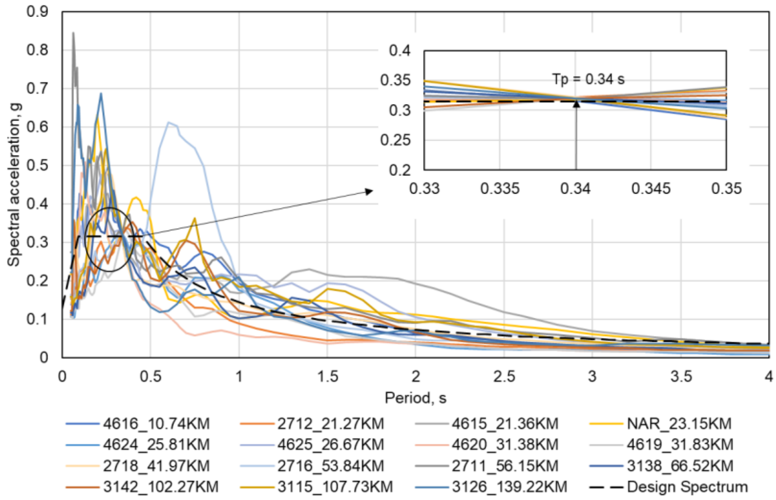

Figure B.6. Scaled spectra of selected ground motions for Nurdağı Gaziantep Mw = 6.6 Earthquake

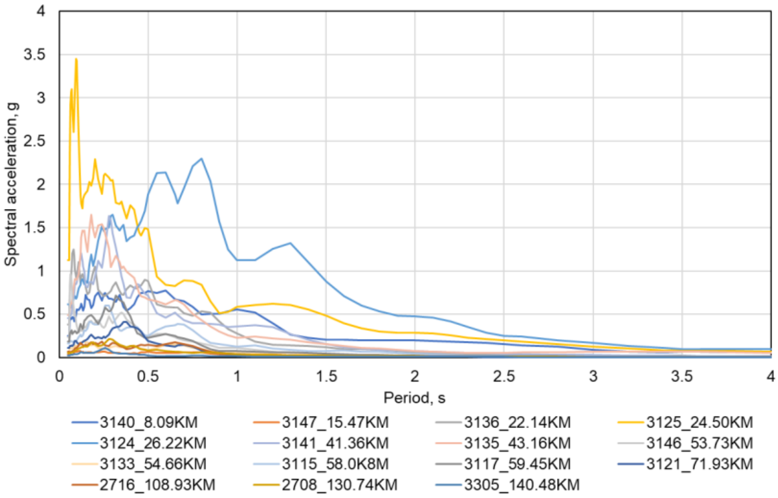

Figure B.7. Unscaled spectra of selected ground motions for Yayladağ Hatay Mw = 6.4 Earthquake

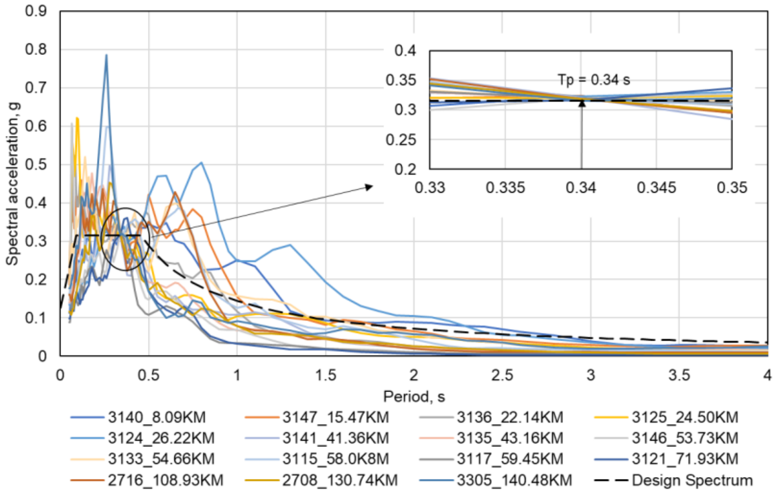

Figure B.8. Scaled spectra of selected ground motions for Yayladağ Hatay Mw = 6.4 Earthquake

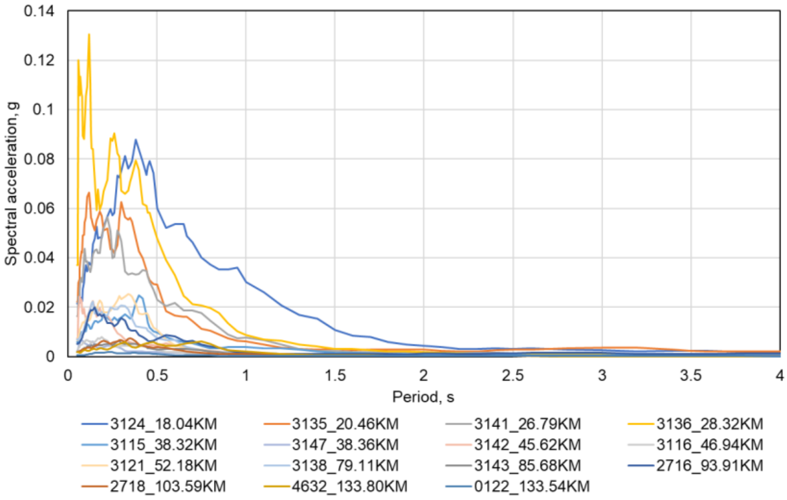

Figure B.9. Unscaled spectra of selected ground motions for Samandağ Hatay Mw = 5.8 Earthquake

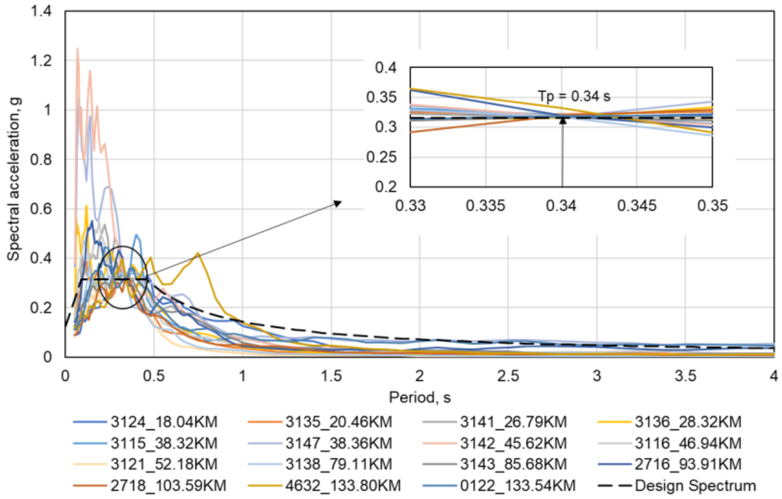

Figure B.10. Scaled spectra of selected ground motions for Samandağ Hatay Mw = 5.8 Earthquake

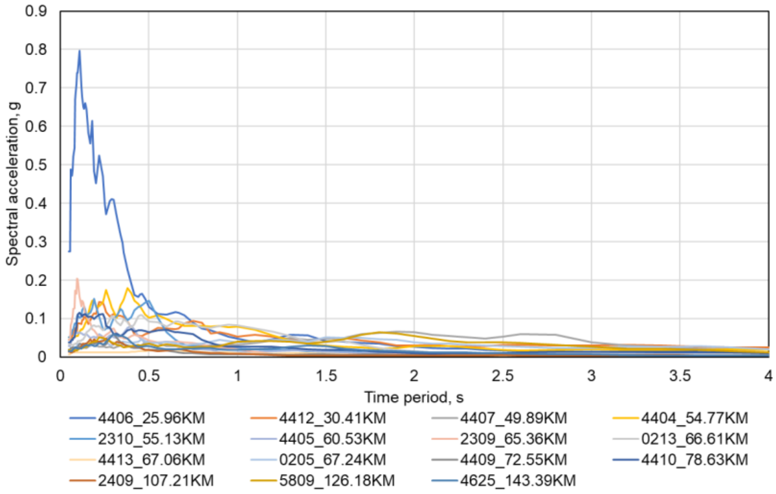

Figure B.11. Unscaled spectra of selected ground motions for Yeşilyurt Malatya ML = 5.8 Earthquake

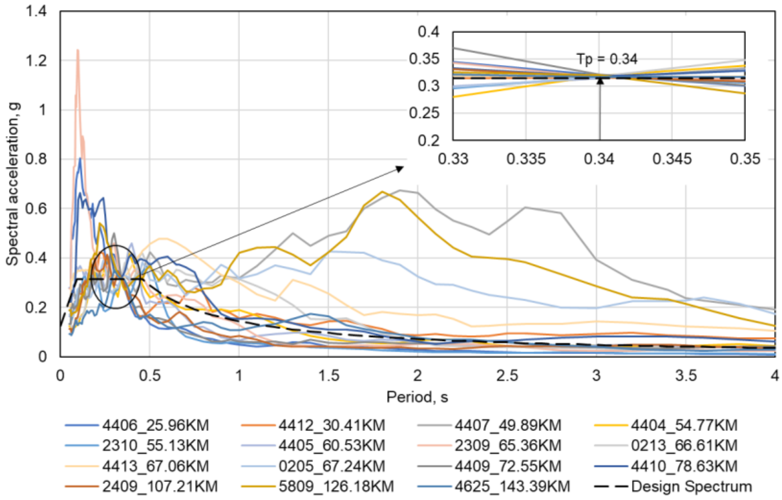

Figure B.12. Scaled spectra of selected ground motions for Yeşilyurt Malatya ML = 5.8 Earthquake

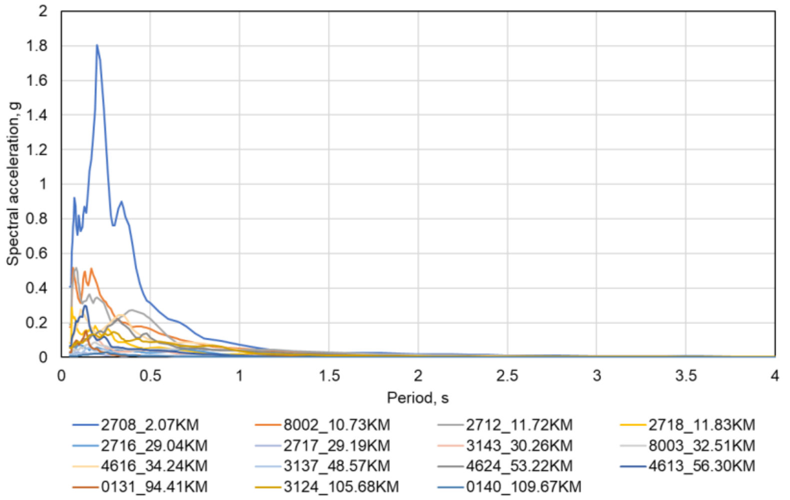

Figure B.13. Unscaled spectra of selected ground motions for Islahiye Gaziantep ML = 5.7 Earthquake

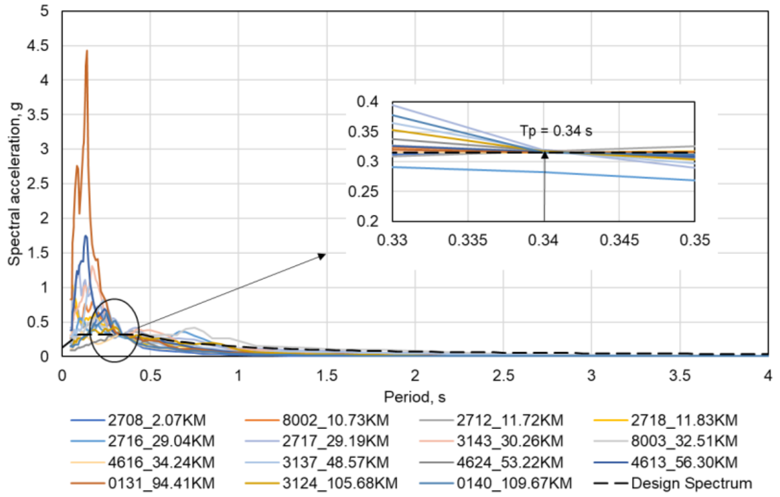

Figure B.14. Scaled spectra of selected ground motions for Islahiye Gaziantep ML = 5.7 Earthquake

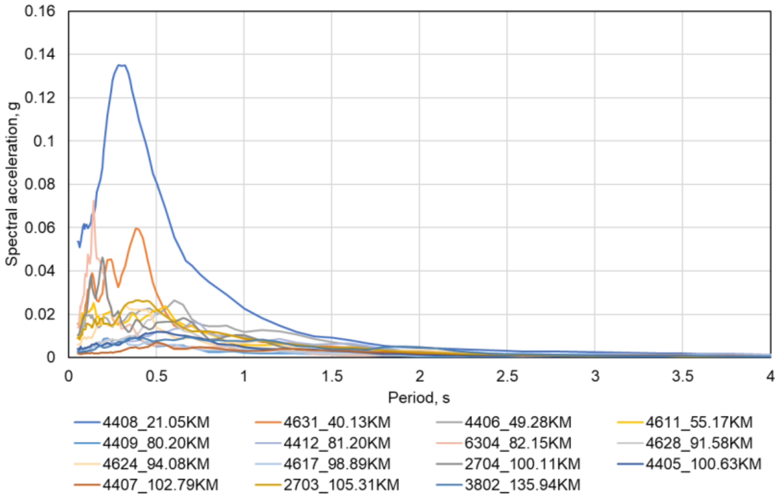

Figure B.15. Unscaled spectra of selected ground motions for Doğanşehir Malatya Mw = 5.6 Earthquake

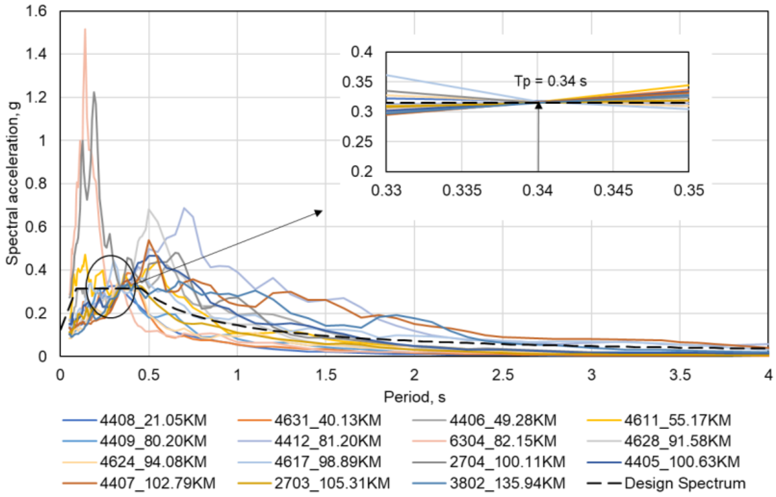

Figure B.16. Scaled spectra of selected ground motions for Doğanşehir Malatya Mw = 5.6 Earthquake

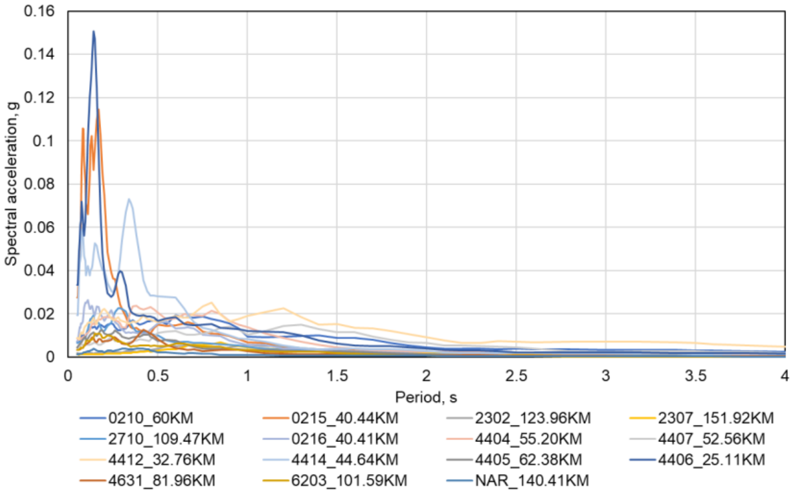

Figure B.17. Unscaled spectra of selected ground motions for Yeşilyurt Malatya Mw = 5.6 Earthquake

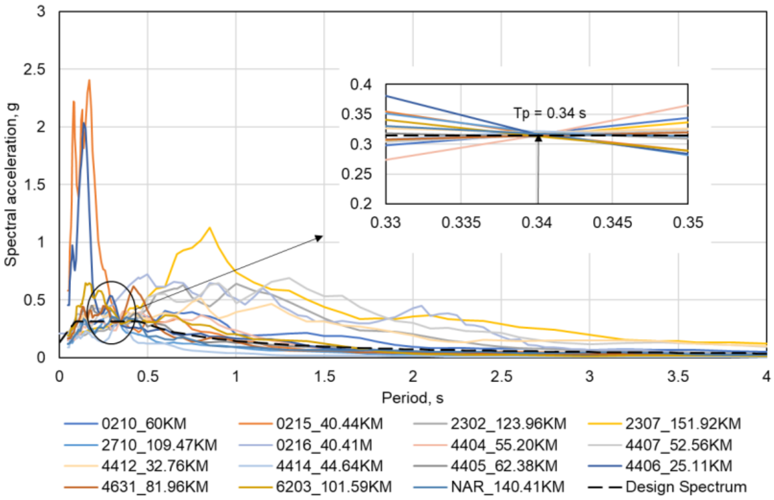

Figure B.18. Scaled spectra of selected ground motions for Yeşilyurt Malatya Mw = 5.6 Earthquake

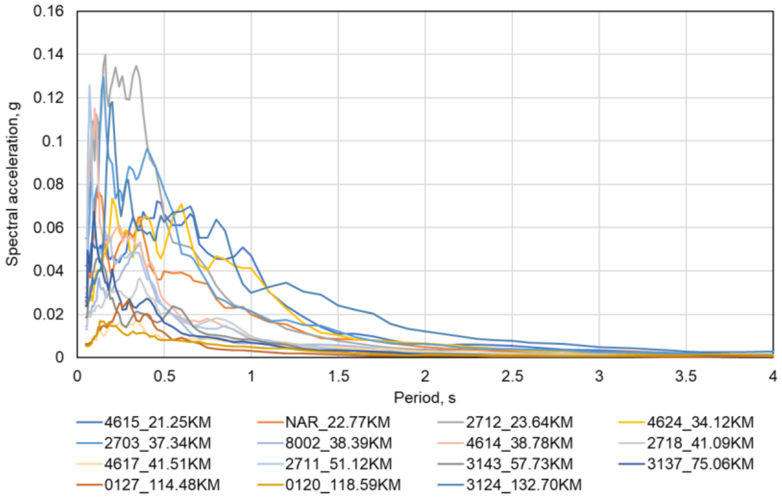

Figure B.19. Unscaled spectra of selected ground motions for Nurdağı Gaziantep ML = 5.6 Earthquake

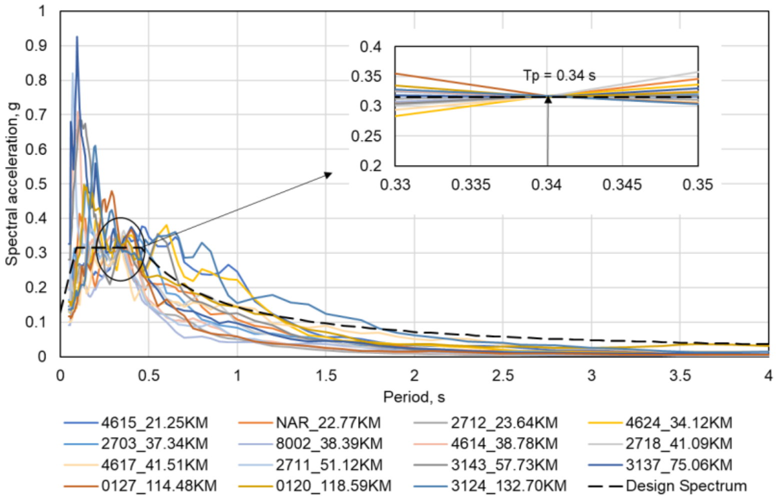

Figure B.20. Scaled spectra of selected ground motions for Nurdağı Gaziantep ML = 5.6 Earthquake

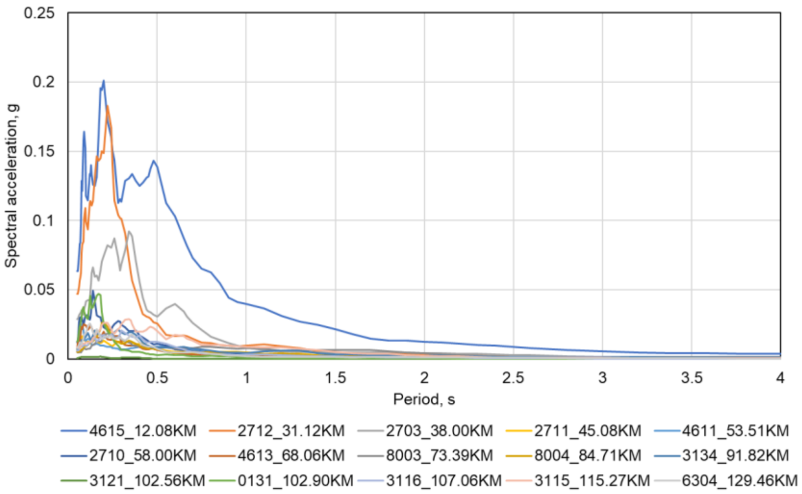

Figure B.21. Unscaled spectra of selected ground motions for Pazarcık Kahramanmaraş Mw = 5.5 Earthquake

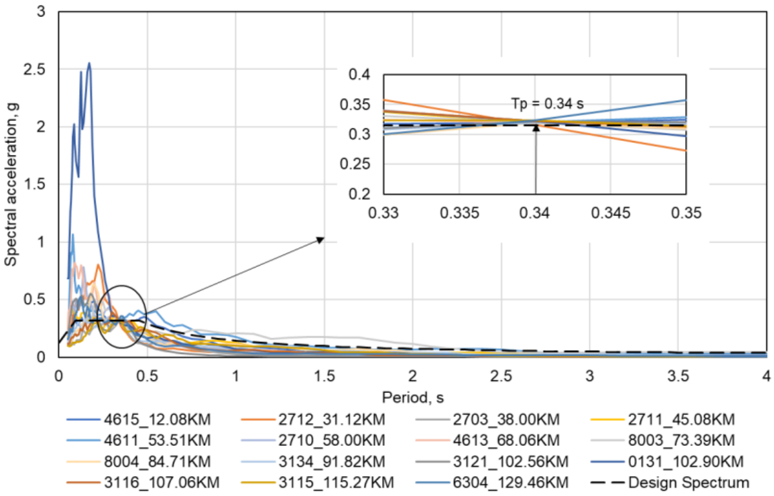

Figure B.22. Scaled spectra of selected ground motions for Pazarcık Kahramanmaraş Mw = 5.5 Earthquake

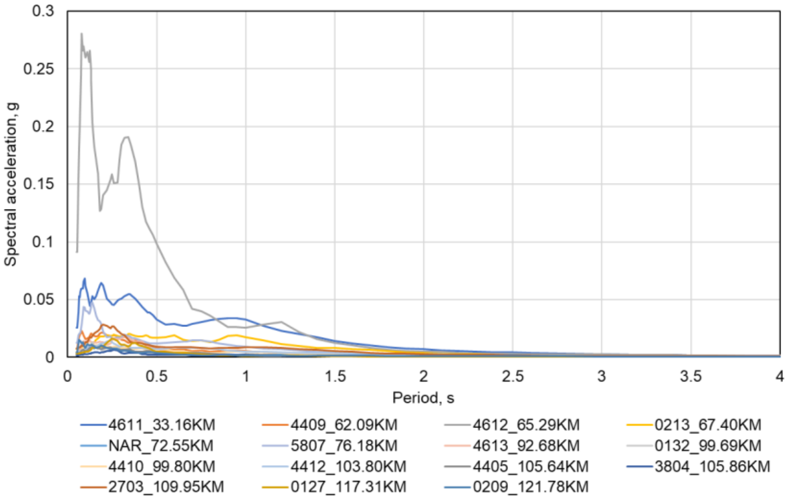

Figure B.23. Unscaled spectra of selected ground motions for Ekinözü Kahramanmaraş ML = 5.5 Earthquake

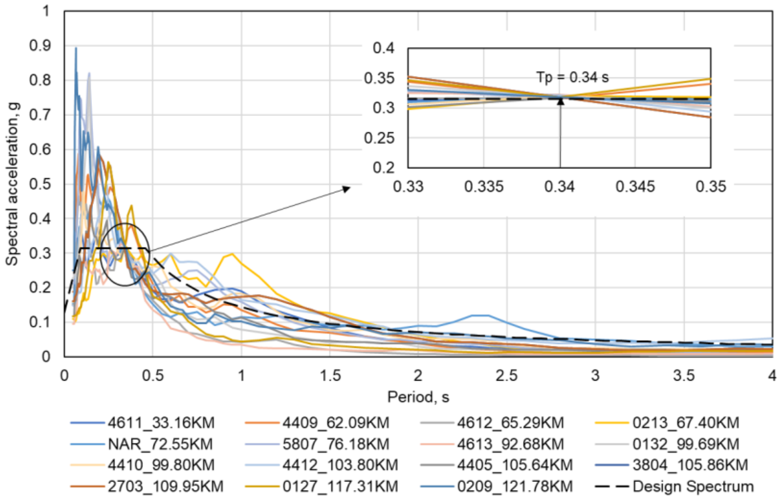

Figure B.24. Scaled spectra of selected ground motions for Ekinözü Kahramanmaraş ML = 5.5 Earthquake

C. Figures for Earthquake Data Distribution to Distance Parameters

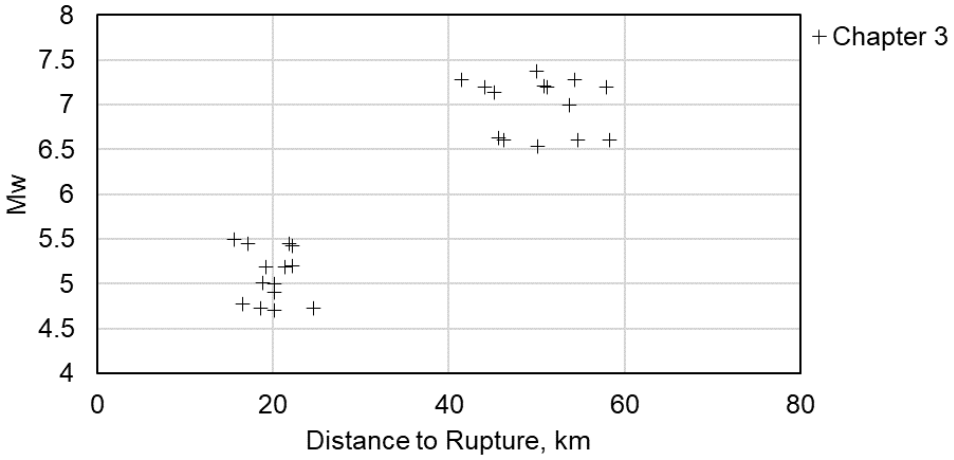

Figure C.1. Earthquake data distribution used in Chapter 3

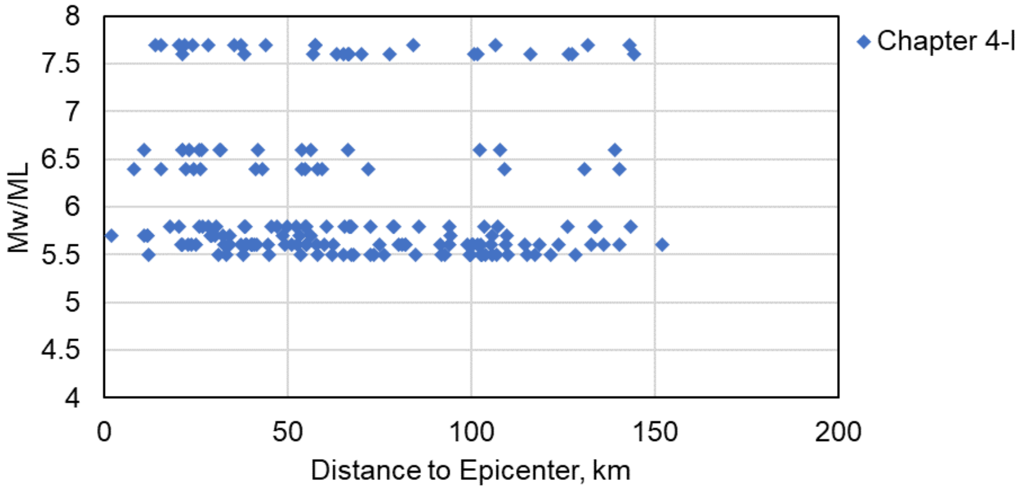

Figure C.2. Earthquake data distribution used in Chapter 4 : Scaled ground motions

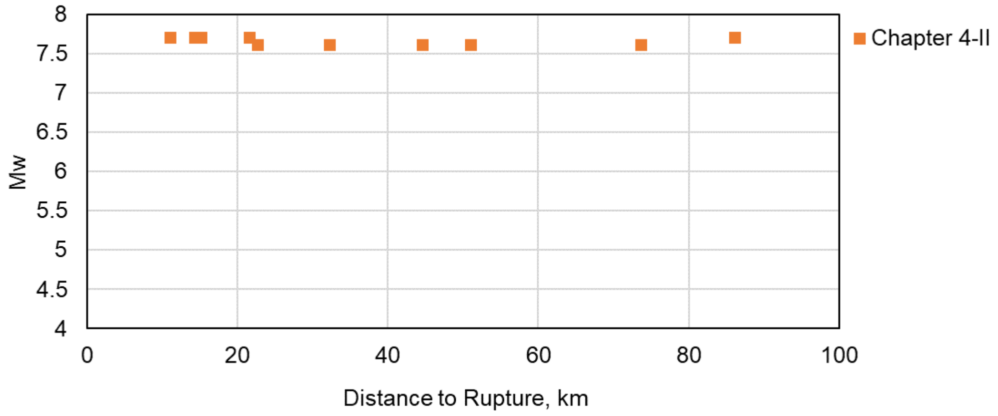

(a)

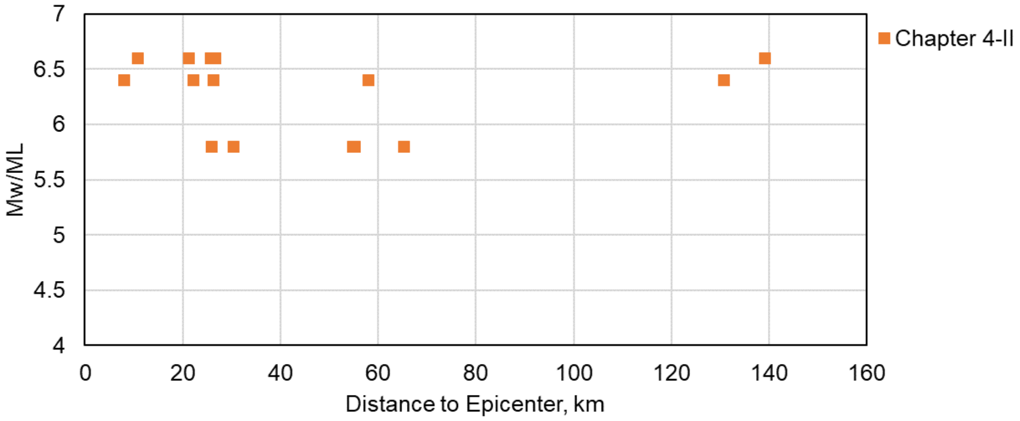

(b)

Figure C.3. Earthquake data distribution used in Chapter 4 : Unscaled groud motions based on distance to: (a) rupture; (b) epicenter

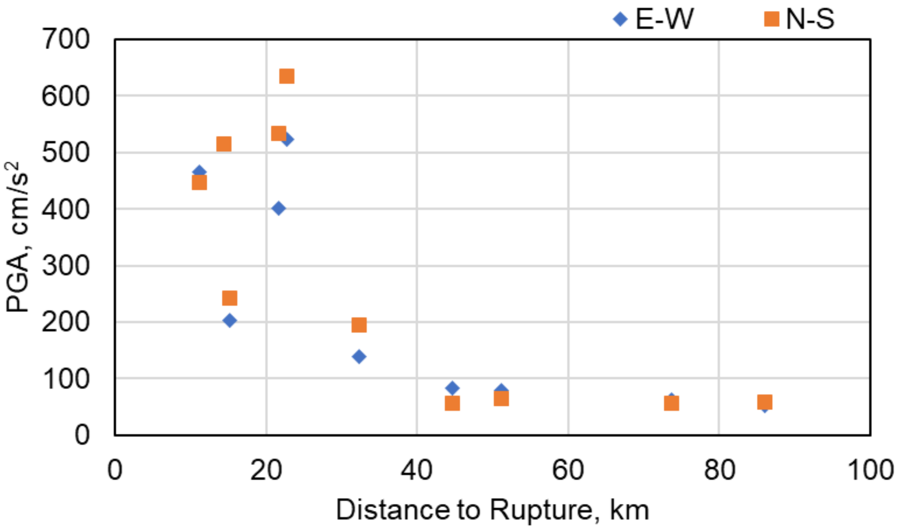

(a)

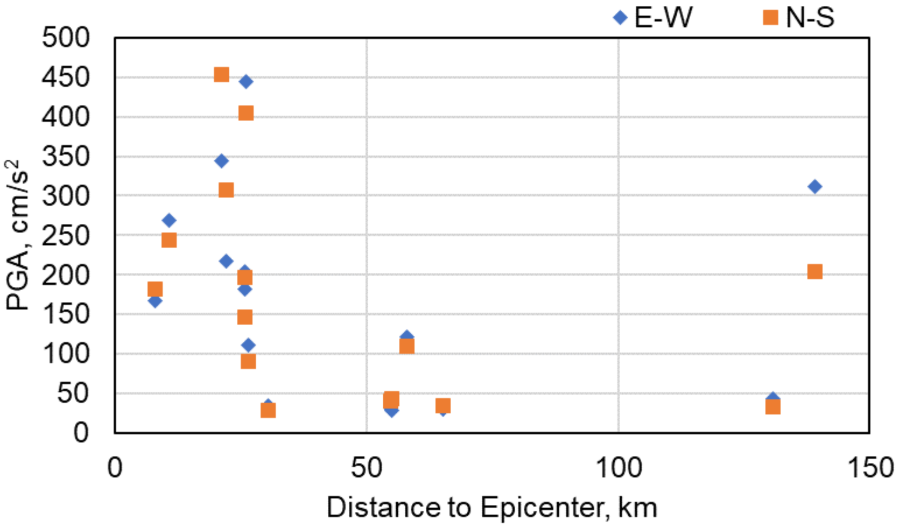

(b)

Figure C.4. Relation between PGA and distance to: (a) rupture; (b) epicenter

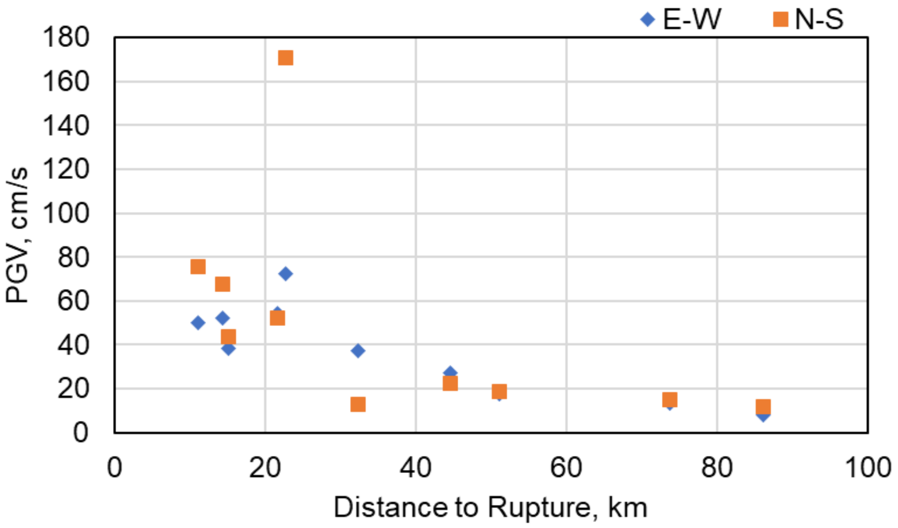

(a)

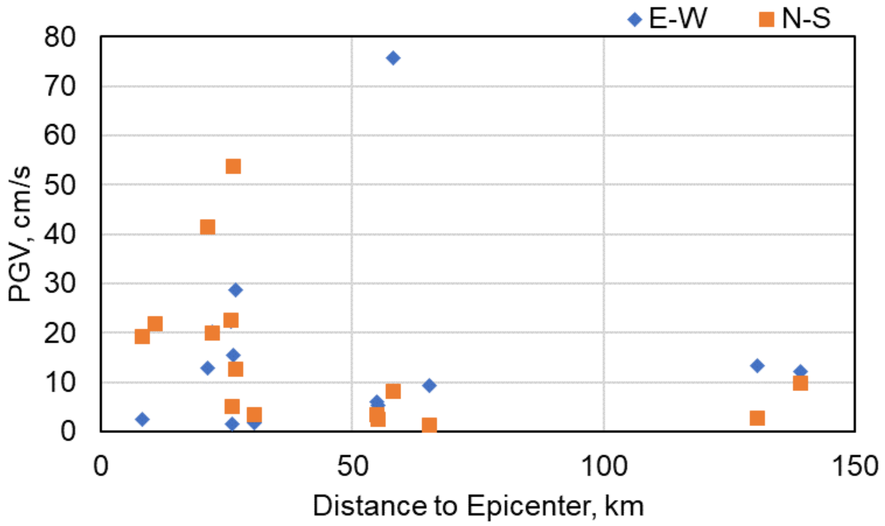

(b)

Figure C.5. Relation between PGV and distance to: (a) rupture; (b) epicenter

CURRICULUM VITAE

Surname, Name: Öztürk, Alper

EDUCATION

Degree	**Institution**	**Year of Graduation**
MS	METU Civil Engineering	2017
BS	METU Civil Engineering	2015
High School	TED Ankara College	2010

EXPERIENCE

Year	**Place**	**Enrollment**
2015-2016	Sigal Mühendislik Ltd. Şti.	Infrastructure Engineer
2016-2023	Yüksel Proje A.Ş.	Deputy Manager
2023	PINI Group SA	Technical Coordinator

FOREIGN LANGUAGES

Fluent English, Basic French

PUBLICATIONS

1. Ozturk, A., Baran, E., Askan A. (2024). A Numerical Investigation on Longitudinal Track-Bridge Interaction in Simply Supported Precast Concrete Girder Railway Bridges. Practice Periodical on Structural Design and Construction. (Accepted for publication on January 10, 2024)

2. Ozturk, A., Baran, E., Askan A. (Under Review). Investigation of Longitudinal Track-Bridge Interaction in Railway Bridges under Seismic Ground Motion. Structures.

3. Ozturk, A., Baran, E., Tort, C. (2019). Nonlinear fiber modeling of steel-concrete partially composite beams with channel connectors. KSCE Journal of Civil Engineering, 23(5), 2227–2242.